Wave propagation in spatially extended systems

by

Stephanie A. Dodson

B.Sc., University of Massachusetts, Amherst; Amherst, MA, 2014

M.Sc., Brown University; Providence, RI, 2015

A dissertation submitted in partial fulfillment of the
requirements for the degree of Doctor of Philosophy
in The Division of Applied Mathematics at Brown University

PROVIDENCE, RHODE ISLAND

May 2019

This dissertation by Stephanie A. Dodson is accepted in its present form by The Division of Applied Mathematics as satisfying the dissertation requirement for the degree of Doctor of Philosophy.

Date_____ _____

Björn Sandstede, Ph.D., Advisor

Recommended to the Graduate Council

Date_____ _____

John Mallet-Paret, Ph.D., Reader

Date_____ _____

Margaret Beck, Ph.D., Reader

Approved by the Graduate Council

Date_____ _____

Andrew G. Campbell, Dean of the Graduate School

Vita

Education

- Brown University, Providence, RI, 2014 - 2019

  Ph.D. in Applied Mathematics, expected May 2019

  M.Sc. in Applied Mathematics, 2015

- University of Massachusetts, Amherst, Amherst, MA, 2010 - 2014

  B.S. in Mathematics

  B.S. in Physics

  Commonwealth Honors College Scholar with Greatest Distinction

Honors and Awards

- 2018, National Science Foundation Graduate Internship Program
- 2018, SIAM Student Travel Award for SIAM Annual Meeting
- 2018, Association for Women in Mathematics Poster Prize, SIAM Annual Meeting
- 2017, Red Sock Award for Poster Presentation, SIAM Conference on Applications of Dynamical Systems

- 2017, SIAM Student Travel Award for SIAM Conference on Applications of Dynamical Systems
- 2015, National Science Foundation Graduate Research Fellowship

Teaching Experience

- Instructor, Applied Ordinary Differential Equations, Brown University, Summer 2017
- Teaching Assistant, Methods of Applied Mathematics I, Brown University, Spring 2016
- Teaching Assistant, Applied Ordinary Differential Equations, Brown University, Fall 2015

Service and Professional Activities

- Sheridan Center for Teaching and Learning, Brown University
  - Course Design Seminar, Spring 2018
  - Teaching Consultant Program, Fall 2017 - Spring 2018
  - New TA orientation workshop leader, Fall 2017
  - Certificate I: Reflective Teaching, Fall 2016
- Mentor, Directed Reading Program, Division of Applied Mathematics, Brown University, Fall 2018 - Spring 2019
- Organizer, Lefschetz Center for Dynamical Systems Seminar, Division of Applied Mathematics, Brown University, Fall 2018 - Spring 2019

- Mentor, Applied Math Undergraduate-Graduate Mentoring Program, Division of Applied Mathematics, Brown University, Fall 2015 - Spring 2019
- Participant, NOAA Ocean Satellite Data Course, University of Washington, Seattle, WA, August 28 - 30, 2018
- Participant, MBI-NIMBioS-CAMBAM Summer Graduate Program: Connecting Biological Data with Mathematical Models, NIMBioS, Knoxville, TN, June 18 - 23, 2017
- Organizer, Women's Intellectual Network Research Symposium, New England, March 4, 2017
- Organizer, Brown University Math Slam, Division of Applied Mathematics, Brown University, Fall 2016 - Spring 2017
- President, Brown University Association for Women in Mathematics Student Chapter, Fall 2015 - Spring 2017
- Faculty-Graduate Liaison, Division of Applied Mathematics, Brown University, Fall 2015 - Spring 2017
- Participant, Gene Golub SIAM Summer Schoo, Drexel University, Philadelphia, PA, July 25 - August 5, 2016
- Participant, Séminaire de Mathématiques Supérieures: Dynamics of Biological Systems, University of Alberta, Edmonton, Alberta, Canada, May 30 - June 11, 2016
- Participant, Brown-ICERM-Kobe Summer Simulation School, Brown University, Providence, RI and Kobe University, Kobe, Japan, August 17 - 31, 2015
- Secretary, Brown University Association for Women in Mathematics Student Chaper, Fall 2014 - Spring 2015

- Other service: Events organizer for Rose Whelan Society for Women in Math (2014 - 2019), Co-organizer of Applied Math graduate student retreat, Judge for Association for Women in Mathematics National Essay Contest (2017, 2019)

Publications

- H.M. McNamara, S. Dodson, Y-L Huang, E.W. Miller, B. Sandstede, and A.E. Cohen. *Geometry-Dependent Arrhythmias in Electrically Excitable Tissues*, Cell Systems, October 2018, doi.org/10.1016/j.cels.2018.08.013

Presentations

- Contributed Talk: *Mechanisms Driving Period-Doubling Instabilities in Spiral Waves* at Dynamics Days, Northwestern University, Evanston, IL, January 6, 2019
- Invited Talk: *Line Defects and Alternans: Period-Doubling Instabilities in Spiral Waves* at SIAM Annual Meeting, Portland, OR, July 13, 2018
- Poster Presentation: *Spectral Properties of Spiral Waves in the Karma Model* in AWM Poster Session at SIAM Annual Meeting, Portland, OR, July 9-14, 2018
- Invited Talk: *Stability of Spiral Waves in Models of Cardiac Tissue* at SIAM Conference on Nonlinear Waves and Coherent Structures, Anaheim-Orange County, CA, June 14, 2018

- Contributed Talk: *Spectral Stability of Spiral Waves in Models of Cardiac Tissue* at Advancing Women's Impact in Mathematics Symposium (AWIMS), Worcester Polytechnic Institute, Worcester, MA, April 7, 2018

- Contributed Talk: *Stability of Spiral Waves in Cardiac Dynamics* at Dynamics Days, Denver, CO, January 4-6, 2018

- Poster Presentation: *Spectral Stability of Spiral Waves in Models of Cardiac Tissue* at Dynamics Days, Denver, CO, January 4-6, 2018

- Contributed Talk: *Stability of Spiral Waves in Cardiac Dynamics* in Applied Math Graduate Student Seminar, Brown University, Providence, RI, November 6, 2017

- Invited Talk: *Stability of Spiral Waves in Cardiac Dynamics* in Boston University Dynamical Systems Seminar, Boston, MA, October 2, 2017

- Poster Presentation: *Spectral Properties of Spiral Waves in the Karma Model* at SIAM Conference on Applications of Dynamical Systems, Snowbird, Utah, May 21-25, 2017

- Contributed Talk: *Spiral Waves in Cardiac Dynamics* at Applied Math Days, Rensselaer Polytechnic Institute, Troy, New York, April 7-8, 2017

- Contributed Talk: *Spiral Waves in Cardiac Dynamics* in Applied Math Graduate Student Seminar, Brown University, Providence, RI, February 27, 2017

- Poster Presentation: *Spectral Properties of Spiral Waves in the Barkley Model* at Dynamics Days, Silver Spring, Maryland, January 4-6, 2017

Professional Associations

- American Mathematical Society (AMS)
- Association for Women in Mathematics (AWM)
- Society for Industrial and Applied Mathematics (SIAM)

Dedication

In memory of my grandmother Anita Dodson, who instilled in me a love of knowledge and always pushed me to succeed.

Acknowledgments

To my advisor Björn, thank you for the continued guidance, enthusiasm, and mentorship throughout the years. I am incredibly thankful to have had Björn as a research advisor and have served as his teaching assistant; in both these roles, he has set an example of excellence and shared his passion for mathematics and learning. His endless support of my professional development has allowed me to grow as a researcher and teacher, and for that I am forever grateful.

I would also like to thank Dr. John Mallet-Paret and Dr. Margaret Beck for taking the time to serve on my thesis committee. Also, to Dr. Adam Cohen and Harry McNamara for collaborating and providing experimental results for this research.

I have been fortunate enough to interact with many members of the Division of Applied Math who have made this last five years memorable. To the many current and previous members of the Sandstede research group, who have served as role models, colleagues, and friends: thank you for sharing your endless knowledge, entertaining and thought-provoking conversations, and of course, animal facts. Anna and Karen, thank you for your friendship and vote of confidence throughout this journey.

Lastly, I am eternally thankful for the support of my family and friends - especially that of my parents and brother.

Contents

List of Tables

List of Figures

Chapter One

Introduction

1.1 Periodic patterns and waves

Periodic patterns are ubiquitously observed in biological and physical processes. The propagation of electrical pulses in neurons and cardiac tissue [1–4], oscillations of chemical reagents [5–7], spots and stripes on animal coats [8], and bands of vegetation [9, 10] are all examples of naturally occurring spatiotemporal periodic waves. Beyond being visually elegant, patterns often have or are the by product of functions. Mathematical studying how these patterns evolve can lead to a deeper understanding of the patterns themselves and a discovery of hidden mechanisms driving their structure and transformations.

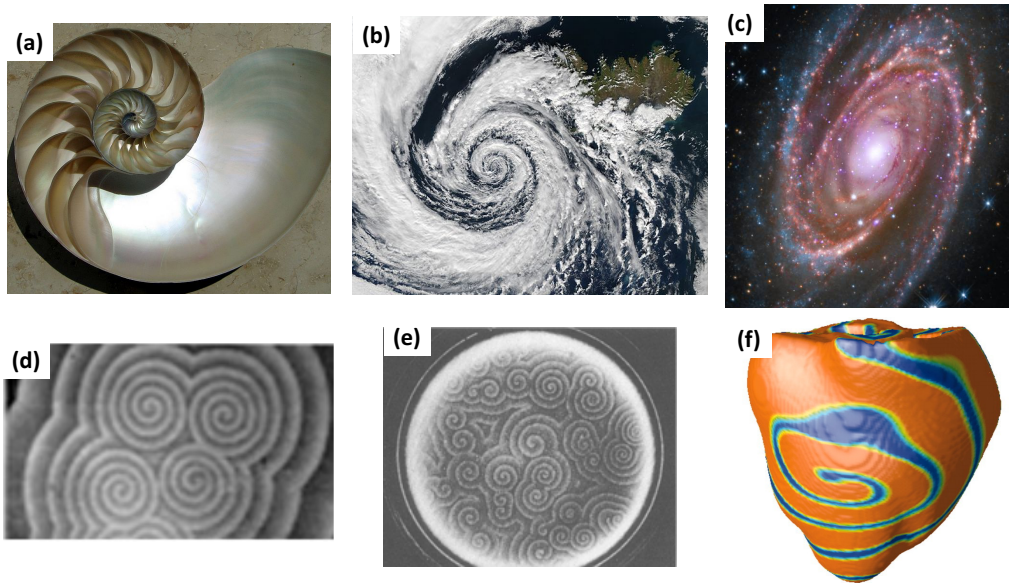

Figure 1.1: Examples of spiral waves in nature. (a) Shell [11], (b) weather system over Iceland [12], (c) Spiral Galaxy M81 [13], (d) Interacting spirals in the Belousov-Zhabotinsky reaction [14], (e) cAMP cell signaling in Dictyostelium discoideum (slime mold) [15], (f) Spiral wave of electrical activity on surface of heart [16]

Of patterns arising in nature, spiral waves are one of the most universal. From designs on sea shells to cloud formation in weather systems and spinning galaxies millions of light years away, spirals appear at an immense variety of length scales

(Figure 1.1). Spirals are observed in the oscillatory Belousov-Zhabotinsky chemical reaction [5, 6], self-organization of amoebae from cAMP signaling in starving slime molds [15], and electrical activity associated with irregular heart rhythms in cardiac tissue [4, 17]. These systems support stable regular traveling and spirals waves of a constant shape, but bifurcations to complex and unstable patterns are also common (Figure 1.2). Spiral patterns are observed to drift and meander while the tip traces out intricate designs [18, 19], form stationary line defects, and express modulations in spiral band width termed alternans. Understanding behaviors of spiral waves in cardiac arrhythmias and chemical oscillations has been a large motivation for this work. As such, spiral waves arising in these applications are further described below.

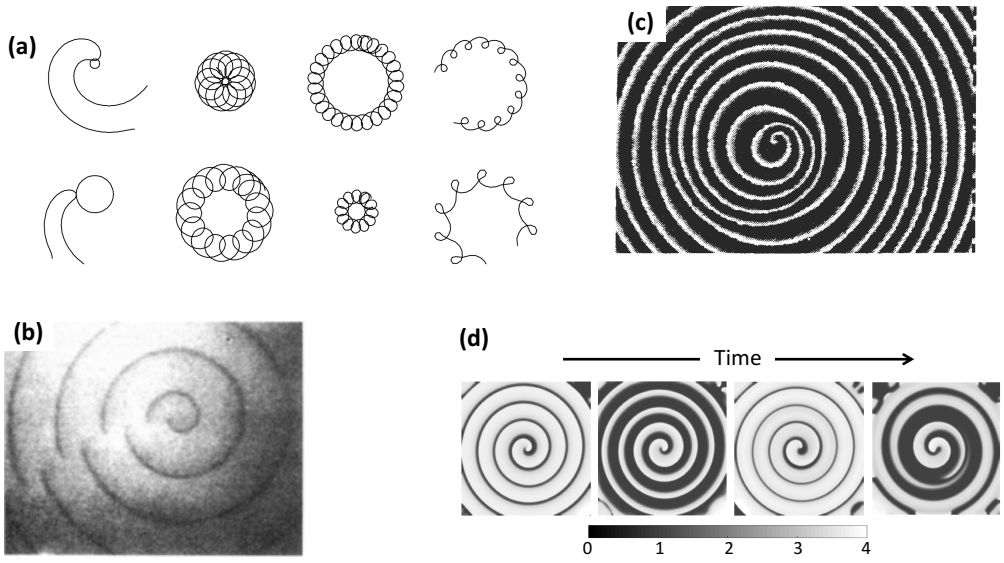

Figure 1.2: Examples of bifurcations in spiral waves of excitable and oscillatory media. (a) Designs traced out by spiral time in meandering [20], (b) Stationary line defect in Belousov-Zhabotinsky chemical reaction [21], (c) Super-spiral structure caused by meandering and drifting [22], (d) Time evolution of alternans in the Karma model

1.1.1 Cardiac arrhythmias

In normal cardiac function, heart beats are initiated by pacemaker cells of the sinoatrial (SA) node located in the atrium. The electrical activity propagates over the surface of the tissue as a traveling wave and causes the atrium to contract. Traveling waves pause at the lower conductance atrioventricular (AV) node as the ventricle fills. Waves then pass through Purkinje fibers in the ventricles and oxygen rich blood is pumped throughout the body [23]. Figure 1.3a provides a schematic diagram of the heart.

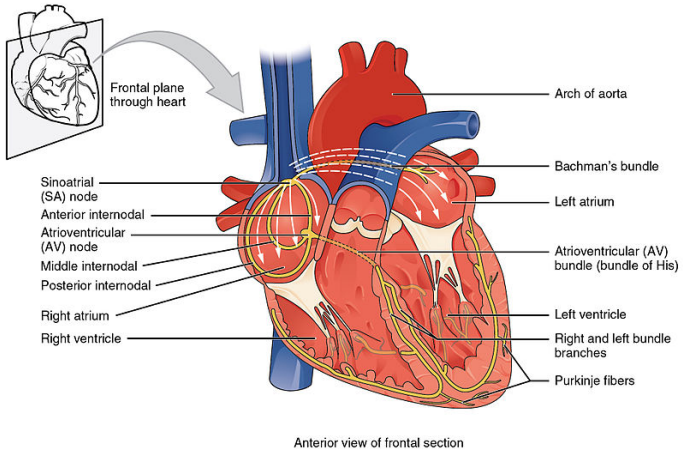

Figure 1.3: Diagram showing regions of the heart [24].

During cardiac arrhythmias, this cycle is interrupted and the typically organized electrical activity can form a spiral wave. Known as reentrant arrhythmias, these spirals rotate independent of the SA node and can be life threatening depending on the location of the wave. In ventricular tachycardia spirals on the ventricles create an accelerated heart rate (100-200 bpm), and is particularly dangerous if the spiral destabilizes as unorganized electrical activity can lead to potentially fatal ventricular fibrillation and sudden cardiac arrest – the leading natural cause of death in the US. The most reliable treatment is an electrical defibrillator which restores natural rhythms through shocking cardiac tissue with potentially damaging currents of up-

wards of 1000 volts [23]. Current research has been focused on less detrimental ways to terminate ventricular tachycardia and fibrillation. A better understanding of how tachycardiac spiral waves transition to fibrillation may help in this endeavor.

Clinical studies indicate a primary driver of spiral wave breakup leading to fibrillation is due to conduction block following a long-short temporal modulation of the action potential duration, corresponding to the variation of spiral band width of the alternans instability (Figure 1.2d) [17, 25]. Alternans are visible on electrocardiograms and have become a clinical warning sign of sudden cardiac death [17, 25]. For a detailed summary of spiral waves in cardiac dynamics, see the review article [26] and recent results published in the special issue [27].

1.1.2 Chemical oscillations

The Belousov-Zhabotinsky reaction is an example of a nonlinear chemical oscillator in which two reactions fluctuate by generating and consuming the same product. The visible oscillations are in the concentrations of intermediate reaction products, and these reactions have been important for the development of the field of non-equilibrium thermodynamics [7].

The Belousov-Zhabotinsky reaction is also a convenient system to study pattern formation in as the oscillations occur on the time scale of minutes and are visible to the human eye. Patterns formed include targets, single and multi-armed spiral waves, and defect patterns. Today, many variants of the original reaction exist, and the research has led to observations of chaotic systems [28] and Turing patterns [29]. Furthermore, the chemical reactions have led to insights into biological systems which

exhibit the same spatial patterns [30]. Further details of spiral waves and pattern formation in the Belousov-Zhabotinsky and other chemical reactions can be found in [7].

Stationary line defects have been experimentally observed in the Belousov-Zhabotinsky reaction [21, 31] and have been reproduced in numerical simulations [32, 33]. Figure 1.2b shows an example of such a defect, where wave amplitudes are out of phase across the stationary lines.

1.2 Reaction-Diffusion systems

Reaction-diffusion systems are canonically used to study pattern formation in physical and biological systems. They display a rich set of dynamics and in general take the form

$$U_t = D\Delta U + F(U), \quad U \in \mathbb{R}^n, \quad D \in \mathbb{R}^{n\times n}, \quad x \in \mathbb{R}^2$$

where $U = (u_1, \ldots, u_n)^T$ is a vector of species that diffuse at rates given by the positive elements δ_j of the diagonal matrix D and Δ is the Laplacian operator. Kinetic reactions of the species are captured by the typically nonlinear function $F(U)$.

Models of oscillatory and excitable media range in complexity from biophysically detailed ion-channel models to reduced systems which imitate qualitative features of the full system. Both categories fall under the reaction-diffusion framework. The propagation of electrical potentials in excitable media, such as neurons and cardiac

tissue, are often described by biophysically detailed ion-channel models given by

$$V_t = \Delta V + f(V, n)$$
$$n_t^j = g(V, n).$$

Here, $V = V(x,t) \in \mathbb{R}$ corresponds to the electrical potential and M dynamic gating variables are given by $n = \left(n^1(x,t), \ldots, n^M(x,t)\right)^T \in \mathbb{R}^M$ which describe the opening and closing of ion channels that facilitate the voltage propagation. Gating variables physically do not diffuse, meaning ion channel models are reaction-diffusion systems with rank-deficient diffusion matrix D.

A separation of time scales in the ion channel models allows for model reductions where species are grouped by fast and slow diffusion rates. Reduced models, including the Barkley [18], Karma [34], Fenton-Karma [35], and Rössler models, have been successful in capturing transitions to complex meandering, drifting, and the period-doubled line defects and alternans patterns observed in the detailed equations and provide more tractable systems for numerical and analytical studies.

The core of a planar spiral wave is a source that emits periodic waves, which far away from the core limit to one-dimensional periodic wave trains. However, whether it be a laboratory dish or the surface of the heart, transitions to period-doubled patterns are physically observed on bounded domains. When posed on finite domains, planar spiral waves are truncated and periodic waves emitted from the core are now matched with boundary sinks. In both of these systems spiral waves are stationary solutions on $\mathbb{R}^2$ or a bounded disk in a rotating polar coordinate frame, allowing for stability and transitions to be studied by considering the spectra of the operator obtained by linearizing the nonlinear system about the spiral wave solution.

Stability of a planar spiral wave is determined by continuous curves of essential spectrum that describe perturbations convected to or away from the core, and finitely many point eigenvalues which have exponentially decaying eigenfunctions. On a bounded domain, the spiral spectrum is a union of eigenvalues from three sets: (1) eigenvalues from the planar spiral that persist under domain truncation and associated with core instabilities, (2) eigenvalues from far-field dynamics, and (3) eigenvalues created by the boundary sink [33]. Therefore, unstable eigenvalues and associated behaviors are generated by instabilities from one of these sets. In particular, if the addition of the boundary sink generates unstable eigenvalues, then the domain shape and size may influence the resulting behaviors. On the other hand, if instabilities are not a result of the boundary sink, then unstable patterns will likely be observed independent of domain features.

Alternans and line defects are particularly interesting mathematically as they lead to a spiral wave with twice the period of the original planar wave and can be though of as period-doubling bifurcations. On bounded disks, they originate through the destabilization of point eigenvalues which have imaginary parts at half-multiples of the angular frequency, but it is unknown if and how the restriction to finite domains influences the instabilities and generation of these point eigenvalues. Meander and drift instabilities are the result of a Hopf bifurcation associated with the core, and dynamics well understood through actions of the symmetry group of translations and rotations on the plane and a center manifold reduction [19, 36]. However, previous studies provide inconsistent and incomplete evidence of the contributions of core, far-field, and boundary conditions to the formation of alternans and line defects.

Understanding how the domain contributes to transitions and stability of wave pat-

terns provides insight into the mechanisms responsible for complex patterns and what domains are relevant for their study. Our approach to determining what regions generate unstable point eigenvalues on bounded domains uses spectral theory and considers how patterns and operators are changed by boundary conditions. In particular, eigenvalues that persist under domain truncation and those generated by the boundary are directly computed through analysis of the boundary sink and a spiral with non-reflecting boundary conditions which mimics an infinite domain.

Finally, spectral properties of spiral waves have been primarily studied in qualitative models, both with positive and zero diffusion in all variables [16, 18, 37, 38], but positive diffusion for all species may be unphysical in certain models. Furthermore, detailed ion-channel models contain many diffusionless gating variables, resulting in a singular and rank-deficient diffusion matrix D. In an effort to extend spectral results to biophysically realistic models, we investigate how a rank-deficient diffusion matrix impacts the spiral spectrum. Even in the qualitative Barkley model, a very different and unexpected spectral picture is observed when diffusion is removed from the second variable. Differences are shown in Figure 1.4, and will be discussed in detail in Chapter 4.

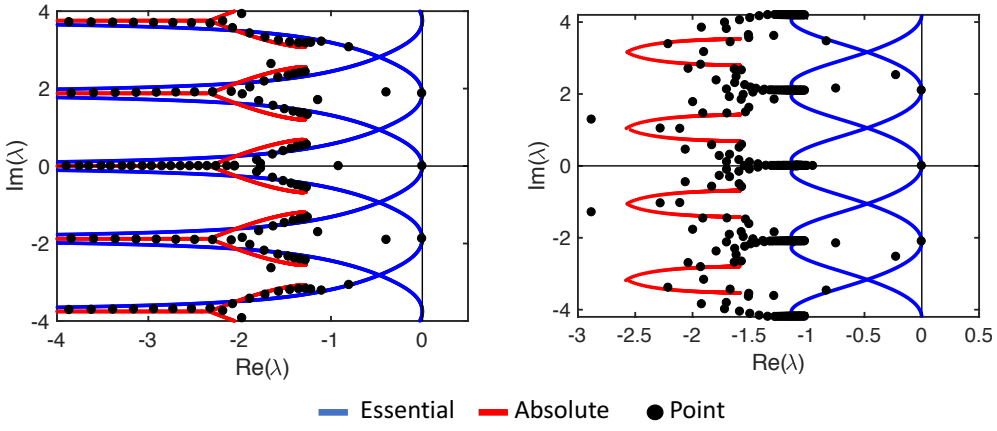

Figure 1.4: (left) Positive diffusion in all components. (right) Zero diffusion in second component results in rank-deficient matrix.

1.3 Outline and overview of results

The goal of this thesis is to further investigate the stability and bifurcations of traveling wave patterns in excitable and oscillatory media, and is organized as follows. First, we focus on investigating domain contributions to spiral wave instabilities. Mathematical theory and notation of periodic traveling waves and spiral waves are reviewed in Chapter 2, including a review of relevant spectral properties for operators on the plane and how these properties are modified by bounded domains. Methods and details of numerical computations are also presented. In Chapter 3, the theory is used to develop a methodology for directly determining the origin of unstable point eigenvalues and is applied to the case of alternans and line defects. In Chapter 4 we turn our attention to understanding the abnormal spectral limits in reaction-diffusion systems with diffusionless variables. Finally, to emphasize that the domain can and does influence system behaviors, we end with an application that highlights how the same electrical forcing protocols applied to a model system for excitable media leads to different spiking behaviors in isolated cells versus spatially extended tissues.

New contributions are presented in Chapters 3, and 4, and Chapters 5 and are further outlined below. A discussion of contributions and directions for future work are included in Chapter 6.

- *Period-doubling instabilities in spiral waves:* We introduce a procedure to determine if bifurcations of two-dimensional patterns on bounded domains arise from unstable point eigenvalues attributed with the spiral core, far-field dynamics, or boundary conditions. The method is applied to investigate mechanisms driving the line defects and alternans instabilities observed in spiral waves on

bounded disks. Our results indicate that line defects arise due to boundary effects, meaning that line defects will only be present on finite domains and boundary conditions may influence the observed instability. On the other hand, alternans are a product of core instabilities, and domain shape and boundaries are less influential in their development. Moreover, the shape of the alternans eigenfunction arises from interaction of point eigenvalues with the essential spectrum.

- *Spectra under zero-diffusion limit:* Unexpected results are observed for the spectra of reaction-diffusion systems in the zero-diffusion limit of the slow species. In an effort to extend spectral results to biophysically relevant ion-channel models and as a first step in understanding this profound behavior, we analyze the essential spectrum under the zero-diffusion limit. We find the continuous curves exhibit a discontinuous limit, in that the spectral curves for small positive diffusion do not limit to the curves for zero-diffusion. Moreover, this behavior is governed by the non-diffusing species. Results are applied to the Barkley model.

- *Geometry-dependent transitions to arrhythmic rhythms:* The role of tissue geometry in transitions to irregular, arrhythmic patterns is explored in a model system of bio-engineered cells. A detailed ion-channel model is developed for the system which reproduces the distinct transitions experimentally observed in single cells versus spatial extended tissues. The model is additionally used to explain how the coupling strength between cells leads to formation of conduction blocks in tissues. Combined, the results urge caution when extending electrophysiology experimental results of single cells to tissues. This work is a collaboration with Harold M. McNamara and Dr. Adam E. Cohen and was published in [39].

Chapter Two

Mathematical Preliminaries

In this chapter, we review relevant theoretical information about one-dimensional periodic traveling waves and spiral waves, both on unbounded domains and the restriction to bounded domains. Next, we describe spectral properties of the patterns. Finally, numerical algorithms used to compute the waves and spectra are described and implementation details provided.

The models studied in this thesis all fall into the category of general reaction-diffusion systems

$$U_t = D\Delta U + F(U), \quad U \in \mathbb{R}^n, \quad D \in \mathbb{R}^{n\times n}, \quad x \in \mathbb{R}^2, \tag{2.1}$$

where $U = (u_1, \ldots, u_n)^T$ is a vector of species that diffuse at rates given by nonnegative elements δ_i of the diagonal matrix D, and Δ is the Laplace operator.

In an attempt to remain consistent with notation throughout this thesis, variables and quantities with a subscript of ∞ will correspond to the periodic traveling wave and a subscript of $*$ to the two-dimensional spiral wave.

2.1 One-Dimensional periodic traveling waves

In our context, periodic traveling waves, also referred to as wave trains, serve as building blocks of spiral waves. Therefore, we first consider the existence and stability properties of wave trains on $\mathbb{R}$ and their restriction to bounded domains before describing spiral waves on the plane and bounded disks.

2.1.1 Periodic waves on the unbounded real line

On $\mathbb{R}$, the reaction-diffusion system (2.1) reduces to

$$U_t = DU_{xx} + F(U), \quad x \in \mathbb{R}. \tag{2.2}$$

Wave trains are solutions to (2.2) of the form $U_\infty(\kappa x - \omega t)$ where U_∞ is 2π-periodic in the argument, κ is the spatial wave number, and ω is the frequency. In the traveling coordinate $\xi = \kappa x - \omega t$, wave trains are stationary solutions of

$$U_t = \kappa^2 DU_{\xi\xi} + \omega U_\xi + F(U), \qquad \xi \in \mathbb{R}. \tag{2.3}$$

An example is shown in Figure 2.1. Generically, wave trains arise as one-parameter families for which ω and κ are connected by the nonlinear dispersion relation $\omega = \omega_*(\kappa)$ for U near U_∞. The group velocity of the wave train describes the direction information is transported by the wave and is defined from the nonlinear dispersion relation as $\mathrm{c_g} = \frac{d\omega}{d\kappa}$.

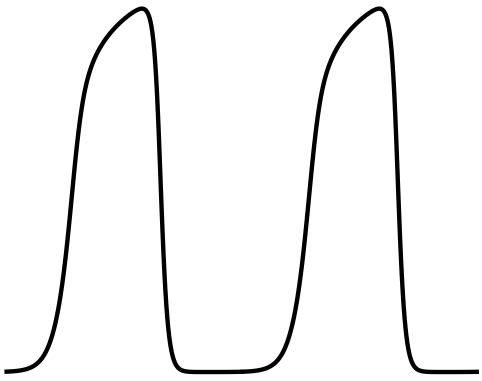

Figure 2.1: Illustration of two periods of a wave train.

2.1.2 Boundary sinks

Infinite domains are unrealistic in nature, and instead finite domains with Neumann boundary conditions are common; these no-flux boundary conditions represent physical walls of the containers in laboratory experiments, lower conductance tissue separating regions of the heart, and are natural computational domains. Imposing boundaries truncates the infinite wave train and creates a source or sink. The wave shape will be modified near the boundary, but will converge to the periodic wave trains in the far-field limit. We say that U_{bdry} is a T-periodic boundary sink if it satisfies the one-dimensional equation on the half-line in the laboratory frame

$$\begin{aligned} U_t &= \frac{T}{2\pi}\left[DU_{xx} + F(U)\right], \quad (x,t) \in (-\infty, 0) \times S^1 \\ U_x(0,t) &= 0, \quad t \in S^1 \end{aligned} \tag{2.4}$$

and has convergence to a wave train $U_\infty(\kappa x - \omega t)$ with $\mathrm{c_g} > 0$

$$\left|U_{\text{bdry}}(x,\cdot) - U_\infty(\kappa x - \cdot)\right|_{C^1(S^1)} \to 0 \text{ as } \; x \to -\infty.$$

In (2.4), the T-periodic boundary sink has been scaled to be 2π-periodic. An example of a boundary sink is shown in Figure 2.2. The characterization of boundary sink arrises from transportation of the wave train towards $x = 0$ from $x = -\infty$ due to the positive group velocity of the asymptotic wave trains. Waves posed on the finite interval $x \in [-L, L]$ can be thought of as a connection between sinks and sources, and are T-periodic solutions of

$$\begin{aligned} U_t &= DU_{xx} + F(U), \quad x \in (-L, L) \\ U(\pm L, \cdot) &= 0 \end{aligned}$$

where Neumann boundary conditions are enforced at the endpoints of the interval.

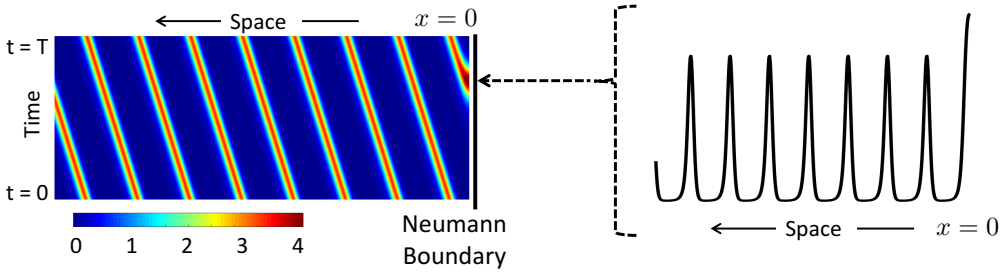

Figure 2.2: Illustration of a boundary sink from the Rössler model. Effect of Neumann boundary condition highlighted by temporal cross section on the right.

2.2 Properties of Spiral Waves

2.2.1 Planar spiral waves

We say that the reaction-diffusion system (2.1) has a planar spiral wave solution of the form $U(x,t) = U_*(r, \phi - \omega t)$ if there exists an $\omega \in \mathbb{R}$ and a smooth function $\theta(r)$ with $\theta'(r) \to 0$ such that U_* satisfies (2.1) and

$$|U_*(r, \cdot - \omega t) - U_\infty(\kappa r + \theta(r) + \cdot - \omega t)|_{C^1(S^1)} \to 0, \qquad \text{as } r \to \infty,$$

where $U_\infty(\kappa r - \omega t)$ is a wave train with $c_g > 0$. Here, (r, ϕ) are polar coordinates of $x \in \mathbb{R}^2$, ω is the temporal rotational frequency, and $\theta(r)$ acts as a phase correction to match solutions at the core with asymptotic wave trains. The spatial wave number κ is selected by the spiral, and the wave train connects ω and κ through the nonlinear dispersion relation $\omega = \omega_*(\kappa)$. Spiral waves are stationary solutions in the co-rotating

polar frame $(r, \psi) = (r, \phi - \omega t)$

$$U_t = D\Delta_{r,\psi}U + \omega U_\psi + F(U). \tag{2.5}$$

Reaction-diffusion systems with diagonal diffusion matrices posses the special Euclidean symmetry group $SE(2)$ of rotations and translations in the plane. Rigidly rotating, meandering, and drifting spiral waves are relative equilibria and relative periodic orbits under these group actions, and the dynamics of planar spiral waves have been described through symmetry groups [19, 36].

2.2.2 Spiral waves on a bounded disk

As with wave trains, finite domains are physically and numerically realistic. Bounded disks in particular are common computational domains as they incorporate rotational symmetry properties of the spiral. When considered on $B_R(0)$, a disk of radius R, planar spiral waves are truncated and solutions with positive group velocity emitted from the core are now matched with time T-periodic boundary sinks $U_{bdry}(\xi, t)$. Spirals formed on $B_R(0)$ with homogeneous-Neumann boundary conditions are stationary solutions in the rotating, polar frame

$$\begin{aligned} &U_t = D\Delta_{r,\psi}U + \omega_R U_\psi + F(U), \quad (r, \psi) \in [0, R) \times S^1 \\ &U_r(R, \psi) = 0, \quad \psi \in S^1. \end{aligned} \tag{2.6}$$

The temporal frequency of the bounded spiral limits to that on the infinite domain $\omega_R \to \omega_*$ as $R \to \infty$. An example of a spiral wave on a bounded disk is compared with a planar spiral wave in Figure 2.3. Note how the homogeneous Neumann boundary

conditions influence the spiral near the outer boundary, similar to the boundary sink from Figure 2.2.

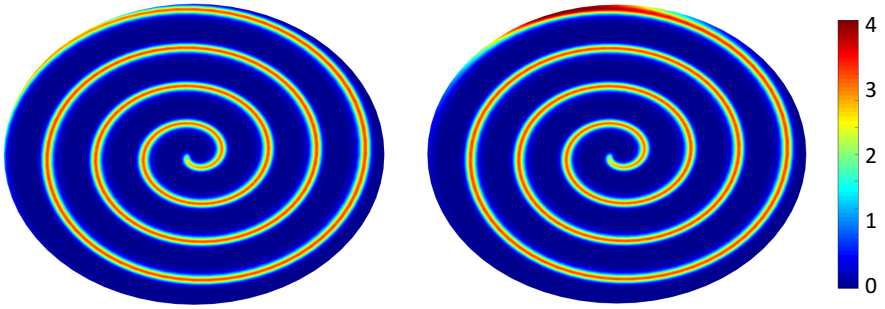

Figure 2.3: (left) Planar spiral wave, shown on disk for comparison purposes. (right) Spiral wave on a bounded disk with Neumann boundary conditions. Note the influence of the boundary on the bounded spiral.

2.3 Review of Spectral Stability Concepts

Here, we give a review of relevant spectral and stability concepts. First, general spectral definitions and terminology is defined. Then, the spectra of the one-dimensional wave trains is described, followed by the spirals on unbounded domains. In each case, we first consider the patterns on infinite domains and then describe how the spectra is modified by bounded domains. Further details can be found in [40–43].

For a closed linear operator $\mathcal{L} : X \to X$ defined on the Banach space X, the spectrum Σ is defined as

$$\Sigma = \{\lambda \in \mathbb{C} : \mathcal{L} - \lambda \text{ is not boundedly invertible}\}.$$

For $\mathcal{L}$ Fredholm, the spectrum can be decomposed into the following disjoint sets, [43]

$$\Sigma = \Sigma_{\text{pt}} \ \cup \ \Sigma_{\text{Fred}} \ \cup \ \Sigma_{\text{FB}}$$

where

$$\Sigma_{\text{pt}} = \{\lambda \in \mathbb{C} : \mathcal{L} - \lambda \text{ is Fredholm with index 0 but not invertible}\}$$
$$\Sigma_{\text{FB}} = \{\lambda \in \mathbb{C} : \mathcal{L} - \lambda \text{ is not Fredholm }\}$$
$$\Sigma_{\text{Fred}} = \{\lambda \in \mathbb{C} : \mathcal{L} - \lambda \text{ is Fredholm with non-zero index }\}.$$

The set Σ_{pt} is referred to as the point spectrum and contains isolated elements called eigenvalues. Σ_{FB} defines the Fredholm border, which gives boundaries for the set Σ_{Fred}. Often, the essential spectrum Σ_{ess} is defined by $\Sigma_{\text{ess}} = \Sigma / \Sigma_{\text{pt}} = \Sigma_{\text{Fred}} \ \cup \ \Sigma_{\text{FB}}$. The contents of each set will depend on the operator and domain, and in particular, sets may be empty for certain operators. These sets are illustrated in Figure 2.4.

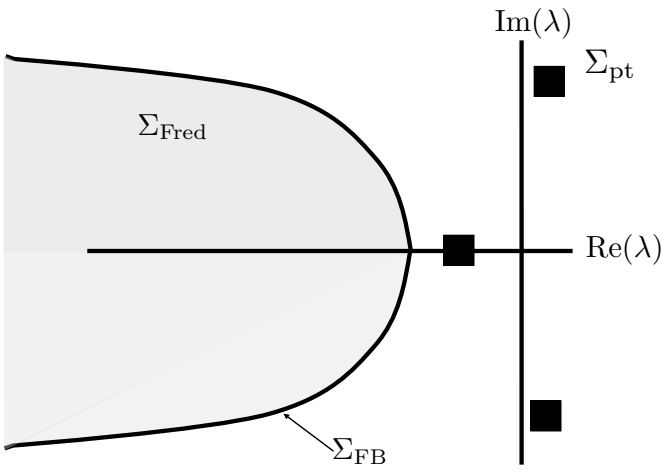

Figure 2.4: Illustration of spectral sets. For large Re λ, the operator $\mathcal{L} - \lambda$ is Fredholm with index 0. Point spectrum (squares) can be found in this region and are defined for λ that make the operator not invertible. Moving to the left, the operator $\mathcal{L} - \lambda$ becomes not Fredholm on the curve Σ_{FB} and is then Fredholm with non-zero index in the shaded region.

2.3.1 Spectral properties of periodic wave trains

Stability of wave trains in the co-moving coordinate frame $\xi = \kappa x - \omega t$ is analyzed by considering the spectrum of the operator

$$\mathcal{L}_\infty^{\text{mv}} V = \kappa^2 D V_{\xi\xi} + \omega V_\xi + F_U(U_\infty) V \tag{2.7}$$

on $L^2(\mathbb{R})$ formed by linearizing (2.3) about the solution U_∞. There are no non-trivial solutions $V \in L^2(\mathbb{R})$ in the kernel of $\mathcal{L}_\infty^{\text{mv}} - \lambda$ and the sets $\Sigma_{\text{pt}} = \Sigma_{\text{Fred}} = \emptyset$. The spectrum Σ of $\mathcal{L}_\infty^{\text{mv}}$ contains only Fredholm borders Σ_{FB}. The linearization $F_U(U_\infty)$ is 2π-periodic, so by Floquet theory we seek non-trivial solutions to $\mathcal{L}_\infty^{\text{mv}} V = \lambda V$ of the form $V(\xi, t) = e^{\nu\xi}\bar{V}(\xi)$ with $\bar{V}(\xi + 2\pi) = \bar{V}(\xi)$ for $\nu \in \mathbb{C}$ and obtain the relation

$$\mathcal{L}_\infty^{\text{mv}}(\lambda, \nu)\bar{V} = \kappa^2 D \left(\partial_\xi + \nu\right)^2 \bar{V} + \omega \left(\partial_\xi + \nu\right) \bar{V} + F_U(U_\infty)\bar{V} - \lambda \bar{V} \tag{2.8}$$

which connects the temporal and spatial Floquet exponents λ and ν, respectively. Therefore, the spectrum Σ of $\mathcal{L}_\infty^{\text{mv}}$ is given by

$$\Sigma_{wt} := \left\{\lambda \in \mathbb{C} : \exists\ \nu \in i\mathbb{R} \text{ and } 2\pi\text{-periodic } V(\xi) \text{ so that } \mathcal{L}_\infty^{\text{mv}}(\lambda, \nu)V = 0\ \forall \xi \in \mathbb{R}\right\}.$$

In particular, Σ_{wt} is the union of smooth curves of the form $\lambda = \lambda_\infty(\nu)$ with $\nu = i\gamma \in i\mathbb{R}$, which are often defined as linear dispersion curves. For each fixed $\lambda \in \mathbb{C}$ in (2.8), there are finitely many $\nu \in \mathbb{C}$ and at least one spatial Floquet exponent crosses the imaginary axis as λ crosses through a spectral curve.

In the laboratory frame, the linearized equation is

$$V_t = D V_{xx} + F_U\left(U_\infty(\kappa x - \omega t)\right) V,$$

which we write as

$$V_t = \mathcal{L}_\infty^{\text{lab}} V.$$

As before, seeking solutions of the form $V(x,t) = e^{\lambda_* t} e^{\nu_* x} \bar{V}(\kappa x - \omega t)$ for 2π-periodic functions $\bar{V}(\kappa x - \omega t) = \bar{V}(\xi)$ yields the relation between temporal and spatial Floquet exponents

$$\mathcal{L}_\infty^{\text{lab}}(\lambda, \nu)\bar{V} = D\left(\kappa\partial_x + \nu\right)^2 \bar{V} + \omega \bar{V}_x + F_U\left(U_\infty(\xi)\right)\bar{V} - \lambda \bar{V}, \tag{2.9}$$

which defines essential spectrum curves $\lambda = \lambda_*(\nu_*)$ for $\nu_* \in i\mathbb{R}$. We note that the essential spectra in the co-moving (2.8) and laboratory frames (2.9) are different: by comparing $\mathcal{L}_\infty^{\text{mv}}(\lambda, \nu)$ to $\mathcal{L}_\infty^{\text{lab}}(\lambda, \nu)$, the spectral curves are related via [33, 44]

$$\lambda_*(\nu_*) = \lambda_\infty(\nu_\infty) - \omega\nu_\infty + i\omega\ell, \quad \ell \in \mathbb{Z}, \quad \nu_* = \kappa\nu_\infty. \tag{2.10}$$

The group velocity in the laboratory frame is also defined by the linear dispersion relation curves via $\mathrm{c_g} = -d\lambda_*/d\nu$.

Essential spectrum computed in the laboratory frame have artificial vertically periodic branches from the $i\omega\ell$ term, which arise from Floquet ambiguity (see Figure 2.5). Additionally, for each fixed $\lambda \in \mathbb{C}$ in (2.8), there are infinitely many $\nu \in \mathbb{C}$ and non-trivial functions $\bar{V}$ such that $\mathcal{L}_\infty^{\text{lab}}(\lambda, \nu)\bar{V} = 0$. Order the spatial eigenvalues ν_j for fixed $\lambda \gg 1$ by real part,

$$\cdots < \mathrm{Re}(\nu_{-j-1}) < \mathrm{Re}(\nu_{-j}) < \cdots < \mathrm{Re}(\nu_{-1}) < 0 < \mathrm{Re}(\nu_1) < \cdots < \mathrm{Re}(\nu_j) < \mathrm{Re}(\nu_{j+1}) < \cdots \tag{2.11}$$

so that $\mathrm{Re}(\nu_{-1}) < 0 < \mathrm{Re}(\nu_1)$. Upon crossing an essential spectrum curve (Fredholm border), one spatial eigenvalue crosses the imaginary axis. Figure 2.6 shows curves of essential spectrum with insets indicating the distribution of spatial Floquet eigenvalues.

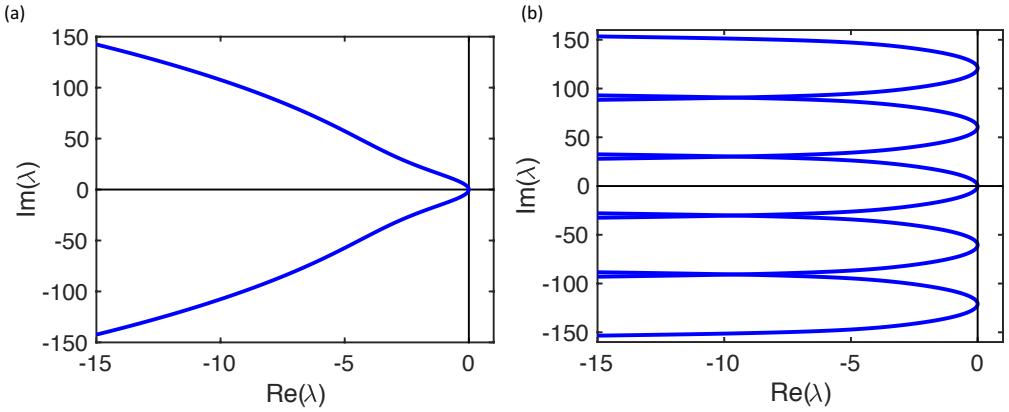

Figure 2.5: Essential spectrum of wave train in (a) co-moving and (b) laboratory frames. In the laboratory frame, curves show Fredholm borders.

Intuitively, the essential spectrum describes convective instabilities, in which growing perturbations are transported away to infinity [41]. If Σ_{ess} crosses into the positive right-half plane, the waves are commonly called convectively unstable. Define the L^2-space with exponential weights by

$$L^2_\eta(\mathbb{R}) := \{u \in L^2_{\mathrm{loc}} : |u|_{L^2_\eta} < \infty\}, \quad |u|^2_{L^2_\eta} := \int_{\mathbb{R}} \left|u(x)e^{\eta x}\right|^2 dx, \quad \eta \in \mathbb{R}. \tag{2.12}$$

The weighted norm permits exponential growth in the eigenfunctions and in $L^2_\eta(\mathbb{R})$ the essential spectrum is characterized by spatial Floquet exponents $\nu = \eta + i\gamma$ [40, 41].

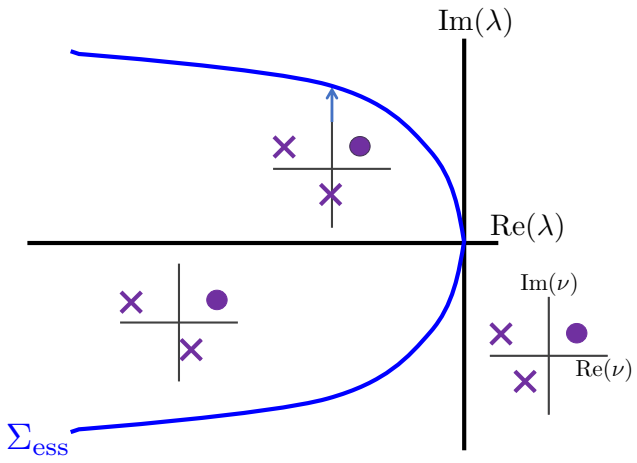

Figure 2.6: Illustration of essential spectrum with spatial Floquet exponent insets. In the insets, crosses (circles) denote spatial eigenvalues with negative (positive) real part for $|\lambda| \gg 1$.

2.3.2 Spectra of spiral waves

2.3.2.1 Spectral stability of planar spiral waves

Stability of planar spirals is similarly performed as the one-dimensional case by considering the spectrum of the operator formed by linearizing (2.5) about $U_*(r,\psi)$

$$\mathcal{L}_* V = D\left(\partial_{rr} + \frac{1}{r}\partial_r + \frac{1}{r^2}\partial_{\psi\psi}\right) V + \omega V_\psi + F_U(U_*(r,\psi))V \tag{2.13}$$

and considering the operator $\mathcal{L}_*$ on $L^2(\mathbb{R}^2)$ with domain $H^2(\mathbb{R}^2)$. Here, the the point spectrum Σ_{pt} contains neutrally stable eigenvalues at the origin and a pair at $\lambda = \pm i\omega$ which arise from rotational and translational symmetries of the planar spiral.

Features of Σ_{ess} depend purely on asymptotic properties of the spiral [41, 44]. In the

formal limit $r \to \infty$, the linear operator $\mathcal{L}_*$ becomes

$$\tilde{\mathcal{L}}_* = D\partial_{rr} + \omega\partial_\psi + F_U(U_\infty). \tag{2.14}$$

Eigenfunctions in the far-field limit take the form [45]

$$V(r,\psi) = e^{\nu r}e^{i\ell\psi}\bar{V}(\xi), \quad \bar{V}(\xi + 2\pi) = \bar{V}(\xi), \tag{2.15}$$

where radial growth or decay is characterized by the real part of the spatial eigenvalue ν and $\bar{V}(\xi)$ is a periodic eigenfunction of the asymptotic wave train. Substitution into $\tilde{\mathcal{L}}_* V = \lambda V$ gives

$$\tilde{\mathcal{L}}_*(\lambda,\nu)\bar{V} = D\left(\kappa\partial_\xi + \nu\right)^2 \bar{V} + \omega\bar{V}_\xi + F_U(U_\infty)\bar{V} - \lambda\bar{V}, \tag{2.16}$$

and we see that the far-field spiral wave linear operator reduces to the case of the laboratory frame wave train (2.9). The Fredholm borders of the essential spectrum are defined by $\lambda = \lambda_*(\nu_*)$ for which one spatial eigenvalue is purely imaginary [41] and in general

$$\begin{aligned}\Sigma_{\text{ess}}\left(\mathcal{L}_*\right) = &\left\{\lambda \in \mathbb{C} : \tilde{\mathcal{L}}_*(\lambda,\nu)\bar{V} = 0 \text{ has a non-trivial solution } \bar{V} \in H^2\left(S^1\right) \text{ for } \nu \in i\mathbb{R}\right\} \\ &\cup \left\{\lambda \in \mathbb{C} : \mathcal{L} - \lambda_* \text{ is Fredholm with non-zero index }\right\}\end{aligned}$$

and are connected to the essential spectrum of periodic wave trains in the co-moving frame via relation (2.10) [44]. Since $\nu_\infty \in i\mathbb{R}$, the mapping does not modify stability properties and $\Sigma_{\text{ess}}\left(\mathcal{L}_\infty\right)$ and $\Sigma_{\text{ess}}\left(\mathcal{L}_*\right)$ destabilize under the same conditions. The additional vertically periodic branches at multiples of $i\omega$ are distinct branches for the spiral and are no longer artifacts from Floquet theory as here, rotational symmetry implies that if $V(r,\psi)$ is an eigenfunction, then so is $e^{i\ell\psi}V(r,\psi)$. As in the

laboratory frame, there exists infinitely many spatial eigenvalues ν for each temporal eigenvalues λ, which we will order by real part, as in (2.11).

Exponential spaces are defined in polar coordinates on $\mathbb{R}^2$ as in (2.12) with weight $\eta \in \mathbb{R}$ in the radial direction

$$L^2_\eta\left(\mathbb{R}^2\right) := \{u \in L^2_{\text{loc}} : |u|_{L^2_\eta} < \infty\}, \quad |u|^2_{L^2_\eta} := \int_{\mathbb{R}^2} \left|u(x)e^{\eta|x|}\right|^2 dx, \quad \eta \in \mathbb{R}.$$

Using the exponentially weighted spaces, we define the extended point spectrum Σ_{expt} by the set of $\lambda \in \mathbb{C}$ such that $\mathcal{L}_* - \lambda$ is not boundedly invertible in $L^2_\eta(\mathbb{R}^2)$ [40, 41]. The exponential weight permits radial growth of eigenfunctions up to weight η.

2.3.2.2 Spectrum of spiral waves on bounded domains

The pertinent linear operator for spiral waves with domain the bounded disk $B_R(0)$ is

$$\begin{aligned} &\mathcal{L}_{*,R}V = D\Delta_{r,\psi}V + \omega V_\psi + F_U(U_{*,R})V, \quad (r,\psi) \in [0,R) \times S^1 \\ &V_r(R,\psi) = 0, \quad \psi \in S^1 \end{aligned} \tag{2.17}$$

and eigenfunctions satisfy the boundary conditions. The spectrum $\Sigma_{*,R}$ of $\mathcal{L}_{*,R}$ contains only point spectrum as the operator $\mathcal{L}_{*,R} - \lambda$ is Fredholm with index zero for all λ, but the set of eigenvalues contains both isolated eigenvalues and infinitely many which converge to well defined continuous limits. We denote the set of isolate eigenvalues by Σ_{isle} and below we will see the continuous part will be described by the absolute spectrum Σ_{abs}.

When posed on domains with separated boundary conditions, convective instabilities described by the essential spectrum are no longer relevant. Instead, perturbations that grow in norm at every point in space become significant and cannot be controlled by an exponentially weighted space. These so-called absolute instabilities arise mathematically when spatial eigenvalues from the groups with positive and negative real parts overlap. The absolute spectrum is defined from the far-field linear dispersion relation $\tilde{\mathcal{L}}_*(\lambda, \nu)$ as

$$\Sigma_{abs} = \{\lambda \in \mathbb{C} : \text{Re } \nu_{-1} = \text{Re } \nu_1\}.$$

Branches are parametrized by $\beta = |\text{Im } \nu_{-1} - \text{Im } \nu_1|$, with $\beta = 0$ at the end points. Curves of Σ_{abs} are not true eigenvalue-eigenfunction pairs related to the invertibility of $\mathcal{L}_{*,R}$, but rather represent limit points of infinitely many discrete eigenvalues as the domain size grows [41]. Note that the absolute spectrum is still defined by the limiting operator $\tilde{\mathcal{L}}_*$ for the planar spiral wave, but is generally distinct from the essential spectrum. An illustration of the spiral spectrum and relation to spatial eigenvalues is shown in Figure 2.7.

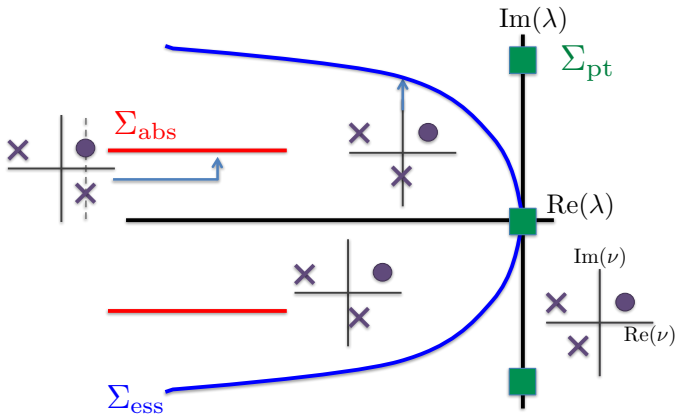

Figure 2.7: Illustration of spectra of linear operator. Inserts show distribution of spatial eigenvalues. Crossing the essential spectrum from right to left results in one spatial eigenvalue crossing the imaginary axis and the real part becoming positive. On absolute spectra curves, the eigenvalue that crossed the imaginary axis aligns with one from the initial positive set.

For every $\lambda \notin \Sigma_{\text{abs}}$, there exists an $\eta \in \mathbb{R}$ such that $\text{Re}\ \nu_{-1} < \eta < \text{Re}\ \nu_1$. Exponentially weighted norms are equivalent on bounded domains, therefore discrete eigenvalues from the extended point spectrum of planar spiral waves $\Sigma_{\text{expt}}(\mathcal{L}_*)$ persist as isolated eigenvalues and are attributed to instabilities from the core. Furthermore, the boundary conditions contribute additional point eigenvalues, which belong to the spectrum of the boundary sink Σ_{bdry} defined above in equation (2.4) [33, 41].

Finally in [46], it was proved that with certain conditions on the asymptotic equations, isolated eigenvalues may emerge from absolute spectrum branch points at predictable angles and destabilize prior to the absolute spectrum. The location of these isolated eigenvalues is predicted by including $1/r$ curvature terms into the asymptotic problem, and has been corroborated in the Barkley Model [47]. Spiral spectra on bounded disks is a union of eigenvalues arising from limiting operators and is summarized in the theorem below [40, Theorem 2.5.5], additional details are in [41].

Theorem 1. *The spectrum $\Sigma(\mathcal{L}_{*,R})$ of $\mathcal{L}_{*,R}$ on $L^2([0,R]\times[0,2\pi))$ under separated boundary conditions converges:*

$$\Sigma(\mathcal{L}_{*,R}) \to \Sigma_{abs}(\mathcal{L}_*) \cup \Sigma_{expt}(\mathcal{L}_*) \cup \Sigma_{bndy} \qquad as\ R\ \to \infty.$$

where $\mathcal{L}_*$ is the operator for a planar spiral wave on $L^2(\mathbb{R}^2)$. Convergence is uniform on bounded subsets of the complex plane in the symmetric Hausdorff distance. Moreover, the multiplicity of the eigenvalues is preserved: the number of eigenvalues, counted with multiplicity, in any fixed open neighborhood of any point $\lambda \in \Sigma_{abs}(\mathcal{L}_*)$ converges to infinity as $R \to \infty$. Multiplicities in neighborhoods of point $\lambda \in \Sigma_{expt}(\mathcal{L}_*), \Sigma_{bndy}$ stabilize and convergence of eigenvalues is of exponential rate in R.

In the notation above, $\Sigma_{\text{isle}} := \Sigma_{\text{expt}}(\mathcal{L}_*) \cup \Sigma_{\text{bndy}}$. Therefore, on bounded domains, eigenvalues fall into one of three sets: (1) extended point spectrum that persist under truncation, (2) eigenvalues converging to and emerging from the Σ_{abs}, and (3) spectrum of the boundary sink.

2.3.2.3 Spatial formulation

The far-field eigenvalue problem (2.16) can also be written as a first-order system in the radial variable. First, transform $(r, \psi) \to (r, \xi) = (r, \kappa r + \psi)$,

$$\lambda V = D\left(\partial_r + \kappa\partial_\xi\right)^2 V + \omega V_\xi + F_U(U_\infty(\xi))V.$$

Then, the first order system is

$$\begin{pmatrix} V_r \\ W_r \end{pmatrix} = \begin{pmatrix} 1 & 0 \\ \kappa^2\partial_{\xi\xi} + D^{-1}\left[\omega\partial_\xi + F_U(U_\infty) - \lambda\right] & 2\kappa\partial_\xi \end{pmatrix} \begin{pmatrix} V \\ W \end{pmatrix} = A(\lambda) \begin{pmatrix} V \\ W \end{pmatrix}. \tag{2.18}$$

This so-called spatial formulation is equivalent to the dispersion relation and provides a geometric interpretation of the continuous spectra. For each fixed λ, the eigenvalues of $A(\lambda)$ are the spatial eigenvalues ν_*. Therefore, elements λ in the Fredholm boundaries of the essential spectrum correspond to values for which $A(\lambda)$ is not hyperbolic, and the distribution of spatial eigenvalues provides the Fredholm index. This formulation will be useful in determining elements in the absolute spectrum, by finding values of λ for which two eigenvalues of $A(\lambda)$ have the same real part (see Section 2.4.4.2).

2.4 Numerical Methods

Many results presented in the following chapters rely on numerical computations. Here, the numerical methods used to compute the asymptotic wave trains, spiral waves, and spectra are described, including the description of the algorithms and implementation details. Computations that are unique to one chapter will be presented there. All computations are performed in MATLAB version 2016b.

2.4.1 Numerical Continuation

Numerical continuation methods are heavily used throughout this thesis to compute asymptotic wave trains, spiral waves, and curves of continuous spectra. Therefore, a short summary of key concepts is provided before discussing the computational details. Additional details can be found in [48, 49].

We wish to find the root U of a smooth, typically nonlinear, equation of the form

$$\mathcal{G}(U,\mu) = 0, \quad U \in \mathbb{C}^n, \ \mu \in \mathbb{C}.$$

Including the parameter μ as input the equation becomes

$$\mathcal{G} : \mathbb{C}^{n+1} \to \mathbb{C}^n. \tag{2.19}$$

If $\tilde{U}_0 = (U_0, \mu_0)$ is a regular solution of (2.19) with full-rank Jacobian matrix, then solution sets of (2.19) will consist of one-dimensional smooth curves, often called solution branches. This result follows from the Implicit Function Theorem.

With an appropriate initial guess, solutions can be found with Newton's method. In this work, numerical continuation is used when a solution for (U_0, μ_0) is known and we want to find solutions for nearby parameter values μ up to a final point μ_*. The basic algorithm to find solution curves is to first update the parameter value μ_{j+1} and then solve for U_{j+1} using Newton's method with U_j as the initial condition. This process is repeated until the final parameter value μ_* is reached.

In basic numerical continuation, the continuation parameter μ is updated with uniform increments and is held fixed during application of Newton's method. Secant continuation is a more advanced method that allows the parameter value to change during the solver step as well. The secant method uses a predictor-corrector framework. In the predictor step, a vector $V_j \in \mathbb{C}^{n+1}$ is found such that $\mathcal{G}'(\tilde{U}_j)V_j = 0$, that is V_j is in the kernel of the jacobian matrix and points in the direction of the solution curve at $\tilde{U}_j$. A step of length h is taken in the direction given by V_j. In the corrector step, the new solution $\tilde{U}_{j+1}$ is solved for by restricting the solution space to the direction normal to V_j. Thus, the modified system solved in the corrector step is

$$\mathcal{G}_{secant}(\tilde{U}_{j+1}) = \begin{pmatrix} \mathcal{G}(\tilde{U}) \\ \langle \tilde{U}_j - \tilde{U}_{j+1}, V_j \rangle - h \end{pmatrix} = 0.$$

The secant algorithm is illustrated in Figure 2.8. Secant methods are particularly helpful when tracing out curves that are non-monotonic in the continuation parameter, such as saddles nodes in bifurcation diagrams. Both basic and secant continuation are used in this study.

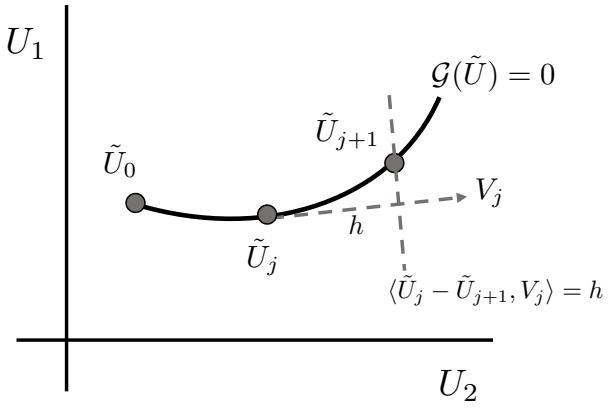

Figure 2.8: Illustration of secant continuation algorithm to trace out curve of solutions.

Symmetries in the equations often result in a one-parameter family of solutions, but a unique solution can be selected by augmenting system (2.19) with a phase condition. The augmented system is now $\mathcal{G} : \mathbb{C}^{n+1} \to \mathbb{C}^{n+1}$ and an additional parameter needs to be allowed to vary to regain the one-dimensional kernel. More will be said about phase conditions and appropriate phase conditions will be defined in the sections that follow.

2.4.2 Computation of one-dimensional wave trains

Asymptotic wave trains $U_\infty(\xi)$ are 2π-periodic one-dimensional stationary solutions of the reaction-diffusion systems in the traveling coordinate $\xi = \kappa x - \omega t$,

$$U_t = \kappa^2 D U_{\xi\xi} + \omega U_\xi + F(U), \quad U \in \mathbb{R}^n \tag{2.20}$$

with $U_\infty(\xi + 2\pi) = U_\infty(\xi)$. We consider (2.20) formulated as a root-finding problem and the wave trains $U_\infty(\xi)$ are non-trivial solutions to $\mathcal{G}_\infty(\tilde{U}) = 0$ where $\tilde{U} = (U_\infty, \omega)$

and

$$\mathcal{G}_\infty(\tilde{U}) = \kappa^2 D U_{\xi\xi} + \omega U_\xi + F(U) \tag{2.21}$$

Numerically, $\mathcal{G}_\infty(\tilde{U}) = 0$ is solved on a 2π-periodic domain discretized with N_θ evenly spaced grid points. Therefore, we can think of the wave train $U_\infty \in \mathbb{R}^{n \times N_\theta}$. Fourier spectral methods are used for differentiation as spectral methods allow for high numerical accuracy with few grid points. Fourier spectral differentiation matrices are computed with the function `fourdif` from the MATLAB Differentiation Matrix Suite [50].

The system $\mathcal{G}_\infty$ is often continued in model parameters μ to find periodic wave trains for a different parameter set. Translational invariance of the wave trains yields a family of solutions, each given by translations on the ξ-axis. To select a unique solution, the phase condition

$$\int_0^{2\pi} \langle U'(y), U_{\text{old}}(y) - U(y) \rangle dy$$

is added to system (2.21) where U_{old} is the solution from the previous continuation step. To counterbalance the addition of the extra phase equation the angular frequency ω is added to the system as a free parameter and is allowed to vary. Selecting ω as the free parameter is a natural choice as modifying system parameters will typically modify the wave shape and speed.

Additionally, the non-linear dispersion relation $\omega = \omega_*(\kappa)$ which relates the wave number and frequency is given by continuing $\mathcal{G}_\infty(\tilde{U}) = 0$ in κ.

2.4.3 Computation of spiral waves

Spiral waves are equilibrium solutions on disks of radius R considered in the polar, rotating frame $(r, \psi) = (r, \phi - \omega t)$

$$U_t = D\Delta_{r,\psi}U + \omega U_\psi + F(U), \quad (r,\psi) \in [0, R) \times [0, 2\pi)$$
$$U_r(R, \psi) = 0, \quad \psi \in S^1.$$

Outer boundary conditions are usually taken to be homogeneous-Neumann. As for the wave train, spirals are numerical computed by solving for roots of the system

$$\mathcal{G}_*(\tilde{U}) = \begin{pmatrix} D\left(\partial_{rr} + \frac{1}{r}\partial_r + \frac{1}{r^2}\partial_{\psi\psi}\right)U + \omega U_\psi + F(U) \\ \partial_r U(R, \cdot) = 0 \end{pmatrix}.$$

Disk domains are discretized on a radial mesh with N_r radial coordinates and N_θ angular grid points. Radial derivatives are approximated by fourth-ordered centered finite difference and Fourier spectral methods with periodic boundary conditions for the angular coordinate. In this formulation, the disk can be thought of as a $N_r \times N_\theta$ rectangle with periodic boundary conditions in the θ direction. Grid sizes and discretizations are chosen to ensure numerical accuracy and to capture a sufficient number of spiral bands for convergence of eigenvalues to occur, while maintaining efficient calculations. As in [47], spiral solutions are solved on a large grid of size $N_\theta \times N_r$ where the origin contains N_θ grid points.

Spirals solutions U_* are given as $N_r \times N_\theta$ vectors with all the angular coordinates for a fixed radius grouped together. The Laplacian on the polar grid takes the form $L = \partial_{rr} + \frac{1}{r}\partial_r + \frac{1}{r^2}\partial_{\phi\phi}$. The three differentiation matrices are formed separately, and are combined with a Kronecker product to create one matrix which acts on the

full 2D structure. Illustrations of the Laplacian differentiation matrix and vector of spiral solutions structures are shown in Figure 2.9. Full differentiation matrices L have a block structure, where each block acts on the angular coordinates for constant radius. Non-zero elements outside of the diagonal blocks act between radii and provide the radial derivative approximations. Therefore, differentiation matrices are composed of N_r blocks of dimension $N_\theta \times N_\theta$ and off-diagonal bands. Outer boundary conditions are implemented in the differentiation matrices; homogeneous-Neumann are incorporated using the ghost point method.

$$L \in \mathbb{R}^{(N_r N_\theta)\times(N_r N_\theta)} =$$

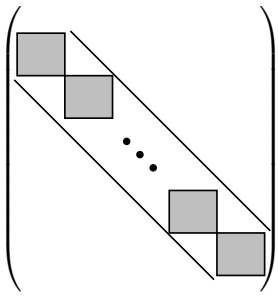

$$U_* \in \mathbb{R}^{N_r N_\theta} = \begin{pmatrix} u_{1,1} \\ \vdots \\ u_{1,N_\theta} \\ u_{2,1} \\ \vdots \\ u_{2,N_\theta} \\ \vdots \\ u_{N_r,1} \\ \vdots \\ u_{N_r,N_\theta} \end{pmatrix}$$

Figure 2.9: Structure of differentiation matrices and numerical spiral solutions.

The polar Laplacian becomes singular at the origin, which is a result of the choice of coordinate system. At the origin, the Laplacian is approximated through the use of an averaging method. Let u_0 be the solution at the origin and $u_{1,j}$ $j = 1, \ldots, N_\theta$ be the N_θ grid points on the first radius Δr. The values of ΔU at the origin are given by an extension of the finite difference 5-point stencil which considers the average of the values on the first radius [47, 51]

$$\Delta U|_{r=0} \approx \frac{4\left[\frac{1}{N_\theta}\sum_{j=1}^{N_\theta} u_{1,j} - u_0\right]}{(\Delta r)^2}.$$

Numerically solving for $\mathcal{G}_*(\tilde{U}) = 0$ using a root finding algorithm is tractable if

starting with a sufficiently good initial condition, such as a spiral on a bounded disk formed under similar parameter values. However, without a good initial condition we can repeatedly solve for the wave train on a growing domain [52]. Asymptotic wave trains are solutions on a ring of radius R_0 and are good approximations for solutions on an annulus with Neumann boundary conditions with inner and outer radii given by $R_{in} = R_0 - \epsilon$ and $R_{out} = R_0 + \epsilon$, respectively. Therefore, we use the one-dimensional wave train as an initial guess for $\mathcal{G}_*(\tilde{U}) = 0$ on the thin annular domain, and use numerical continuation to first grow the domain inward by shrinking R_{in} to 0, and then growing R_{out} to the desired disk size. It is important to start with a initial radius R_0 near $(2\pi\kappa)^{-1}$ where κ is the wave number so that the circumference corresponds to one period. Growing of a spiral wave is shown in Figure 2.10.

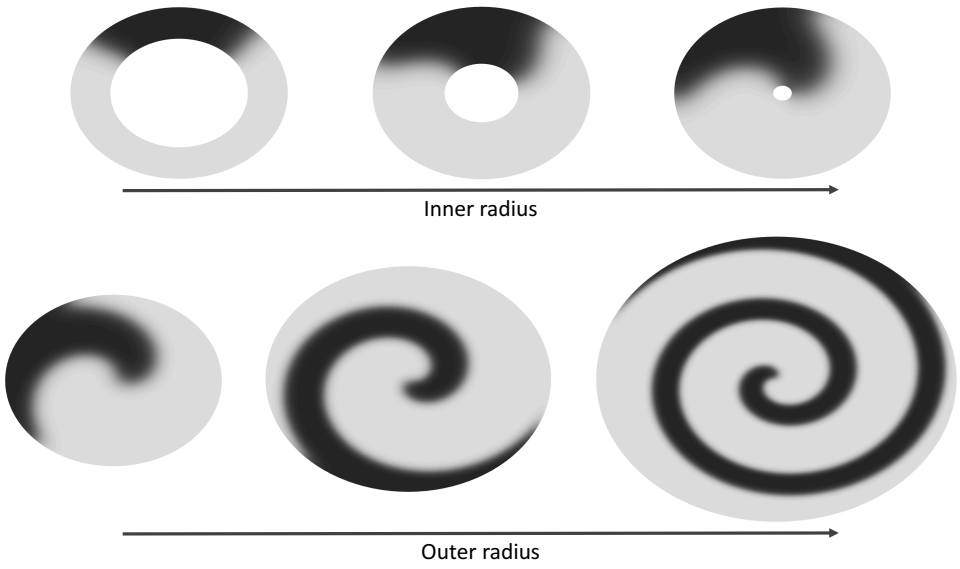

Figure 2.10: Formation of spiral waves on bounded disk by continuation. (Top) Inner radius of annulus is continued to 0. (Bottom) Outer radius of bounded disk continued to form full spiral. Note that figures show growing radius, but are not to scale.

Homogeneous Neumann boundary conditions are also used on the inner radius of the annulus. The disk decomposition described above allows the annulus and spiral to be considered on the same grid. Often, the annulus is started with a low ~ 50 radial grid points, and interpolated onto a finer mesh once the domain is large

enough to support one spiral band.

2.4.4 Computation of continuous spectra

Curves of continuous spectra are calculated using continuation methods described in [53], and are summarized below.

2.4.4.1 Essential spectrum

The essential spectrum curves for spiral waves are defined by values of λ such that $\tilde{\mathcal{L}}_*(\lambda, i\gamma)V = 0$ has a non-trivial solution V. Therefore, curves of essential spectra for the spiral wave are traced out by continuing

$$0 = \tilde{\mathcal{L}}_*(\lambda, i\gamma)V = D\left(\kappa\partial_\xi + i\gamma\right)^2 V + \omega V_\xi + F_U(U_\infty)V - \lambda V$$

in $\gamma = \mathrm{Im}(\nu)$ with free parameter $\lambda \in \mathbb{C}$. The normalization condition

$$\langle V, V\rangle - 1 = 0$$

is included to create a square system. By translational symmetry, $V(\xi) = \partial_\xi U_\infty(\xi)$ is a solution with $(\lambda, \nu) = 0$, and gives an initial condition for the continuation. Basic numerical continuation methods are used in the computation of the essential spectrum because using the secant method allows γ to vary and often results in γ becoming complex. In this case, we do not have to worry about missing features such as saddle nodes using the basic continuation algorithm since the essential spectrum curves are parametrized by γ.

The asymptotic wave train solution $U_\infty \in \mathbb{R}^{n\times N_\theta}$ solved for with methods from Section 2.4.2 is used in the linearization. Likewise, the desired eigenfunction $V \in \mathbb{R}^{n\times N_\theta}$.

2.4.4.2 Absolute spectrum

The absolute spectrum is defined when two spatial eigenvalues have the same real part, thus there are spatial eigenvalues ν_1 and $\nu_2 = \nu_1 + i\beta$, $\beta \in \mathbb{R}$ and non-trivial periodic eigenfunctions $V, \tilde{V}$ such that

$$\begin{aligned} \tilde{\mathcal{L}}_*(\lambda,\nu)\, V &= 0 \\ \tilde{\mathcal{L}}_*(\lambda,\nu+i\beta)\, \tilde{V} &= 0. \end{aligned} \tag{2.22}$$

Following the methods in [53], let $\tilde{V} = V + i\beta W$ and equation (2.22) becomes

$$\tilde{\mathcal{L}}_*(\lambda,\nu+i\beta)\,(V+i\beta W) = 0.$$

Adding in 0,

$$\left[\tilde{\mathcal{L}}_*(\lambda,\nu+i\beta) - \tilde{\mathcal{L}}_*(\lambda,\nu)\right] V + \tilde{\mathcal{L}}_*(\lambda,\nu+i\beta)\, i\gamma W = 0.$$

Plugging in the form of $\tilde{\mathcal{L}}_*(\lambda,\nu)$ and dividing by $i\beta$, the sum reduces to

$$D\left[2(\kappa\partial_\xi+\nu)+i\beta\right](V+i\beta W) + \tilde{\mathcal{L}}_*(\lambda,\nu)\, W = 0.$$

Continuation along absolute spectra curves amounts to solving the system

$$\begin{aligned} &\tilde{\mathcal{L}}_*(\lambda,\nu)\, V = 0 \\ &D\left[2(\kappa\partial_\xi+\nu)+i\beta\right](V+i\beta W) + \tilde{\mathcal{L}}_*(\lambda,\nu)\, W = 0 \end{aligned}$$

along with the two phase conditions

$$\int_0^{2\pi} \langle V_{\text{old}}, V\rangle \, d\xi - 1 = 0$$
$$\int_0^{2\pi} \left[\langle W_{\text{old}}, V\rangle - \langle V_{\text{old}}, W\rangle - i\beta\langle W_{\text{old}}, W\rangle\right] d\xi = 0$$

for eigenfunctions V, W with free parameters ν and λ and continuation parameter $\beta \in \mathbb{R}$. In the phase condition, V_{old} and W_{old} refer to the V, W computed on the previous continuation step. Basic continuation methods are again used to ensure that β remains real.

A starting point for the absolute spectrum continuation is found by directly computing the spatial eigenvalues for fixed $\lambda \in \mathbb{C}$. Under the spatial formulation (2.18) spatial eigenvalues for fixed λ are given by the eigenvalues of $A(\lambda)$. The spatial eigenvalues can be directly computed by approximating the first and second order ξ-derivatives with 2π-periodic Fourier spectral differentiation matrices L_1 and L_2, respectively. Therefore, for each λ spatial eigenvalues are computed from the matrix

$$A(\lambda) = \begin{pmatrix} 1 & 0 \\ \kappa^2 L_2 + D^{-1}\left[\omega L_1 + F_U(U_\infty) - \lambda\right] & 2\kappa L_1 \end{pmatrix}.$$

Note that $A(\lambda)$ only depends on λ, all other quantities are fixed, allowing for efficient computation of ν. Moreover, the movement of spatial eigenvalues can be observed by computing ν for slowly changing values of λ. This computation provides an algorithm for finding points on absolute spectrum curves: start with a value of λ in the positive right-half plane, continue λ through the essential spectrum to observe which ν changes sign, and monitor when $\text{Re}(\nu_1)$ aligns with $\text{Re}(\nu_{-1})$, another

spatial eigenvalue of the opposite sign. The λ value and ν_1, ν_2 pair yield a starting condition for absolute spectrum continuation, with continuation parameter given by $\beta = \mathrm{Im}(\nu_1) - \mathrm{Im}(\nu_2)$.

2.4.5 Computation of spiral point spectra

Finding eigenvalues of a spiral wave on a bounded disk is equivalent to finding the eigenvalues of the Jacobian J matrix of the operator linearized about the wave solution. The Jacobian for a two-variable system $U = (u, v)^T \in \mathbb{R}^2$ with $F(U) = (f(U), g(U))^T$ is given by

$$J = \begin{pmatrix} \delta_1 \Delta_{r,\psi} + \omega \partial_\psi + f_u(U_*) & f_v(U_*) \\ g_u(U_*) & \delta_2 \Delta_{r,\psi} + \omega \partial_\psi + g_v(U_*) \end{pmatrix} \tag{2.23}$$

The eigenvalue problem is solved on a grid of size $N_\theta \times (N_r - 1) + 1$ with one grid point at the origin [47]. A 9-point Laplacian is used for the derivative of the single point at the origin. With the exception of the origin, finite difference and spectral methods are again used for the radial and angular derivatives. The short grid helps to eliminate singularities in the Jacobian for more efficient computations.

Under this formulation, the Jacobian matrix has dimensions $n\,(N_\theta(N_r - 1) + 1) \times n\,(N_\theta(N_r - 1) + 1)$ and eigenvectors V are therefore complex vectors of length $nN_\theta(N_r - 1) + 1$. We expect that most of the $n\,(N_\theta(N_r - 1) + 1)$ discrete eigenvalues will align along the absolute spectrum, but will also contain elements of the extended point spectrum and symmetry eigenvalues.

The built-in MATLAB routines `eig` and sparse version `eigs` are used to find eigenvalues of the Jacobian matrix. The dense solver `eig` is more reliable (see Section 2.4.5.1), but is very computationally expensive.

2.4.5.1 Pseudospectra, computations in weighted spaces, and a word of caution

Important stability properties of non-normal operators can be more accurately captured by the pseudospectrum rather than the traditional spectrum. The ϵ-pseudospectra for an closed, linear operator $A : X \to X$ which maps the Banach space X into itself is defined as

$$\sigma_\epsilon(A) = \left\{\lambda \in \mathbb{C} : ||(\lambda - A)^{-1}|| > \epsilon^{-1}\right\}$$

for $\epsilon > 0$ [54]. By convention, the resolvent norm $||(\lambda - A)^{-1}|| = \infty$ for eigenvalues $\lambda \in \Sigma$. Therefore, ϵ-pseudospectra provide sets of *almost* eigenvalues and eigenfunctions. For normal operators, the pseudospectra is localized around $\lambda \in \Sigma$, but can extend over large regions of the complex plane for highly non-normal operators. Unstable pseudospectra can lead to unstable transient and asymptotic behaviors.

Linear operators associated with reaction-diffusion systems with non-constant coefficient or posed on bounded domains are non-normal. In particular, on bounded domains eigenvalues align along the absolute spectrum and these eigenfunctions share similar spatial growth properties, with growth dictated by the spatial eigenvalue (or Floquet exponent in the case of wave trains). These eigenfunctions do not provide a suitable basis on which to decompose the solutions and instabilities, and cannot be easily extracted by eigenvalue solvers.

Considering exponentially weighted eigenfunctions of the form $v(\xi) = e^{\eta\xi}w(\xi)$ factors out spatial growth and yields a better eigenfunction decomposition. The resulting weighted eigenvalue problem $\mathcal{L}_\eta w = \lambda w$ has the same eigenvalues as the original operator $\mathcal{L}$, and the eigenfunctions now extend influence over the domain.

As an example, consider asymptotic wave trains in the Barkley model on a bounded domain. Pseudospectra curves computed with `eigtool` in Matlab are shown in Figure 2.11. The legend indicates exponential values of ϵ in a $\log_{10}$ scale, hence contours of -14 corresponds to level sets of the ϵ-pesudospectrum with $\epsilon = 10^{-14}$. On the finite domain, eigenvalues should align along curves of absolute spectra, however eigenvalues are observed to convergence to a parabolic curve resembling the essential spectrum (Figure 2.12b), while the absolute spectrum lies in discrete curves far to the left (Figure 2.12a). Representative eigenfunctions from these calculations are shown in Figure 2.12c; observe the similar spatial growth trends. Comparing the discrete eigenvalues from Figure 2.12b with pseudospectra contours, the eigenvalues are converging to roughly the $\epsilon = 10^{-14}$ curve.

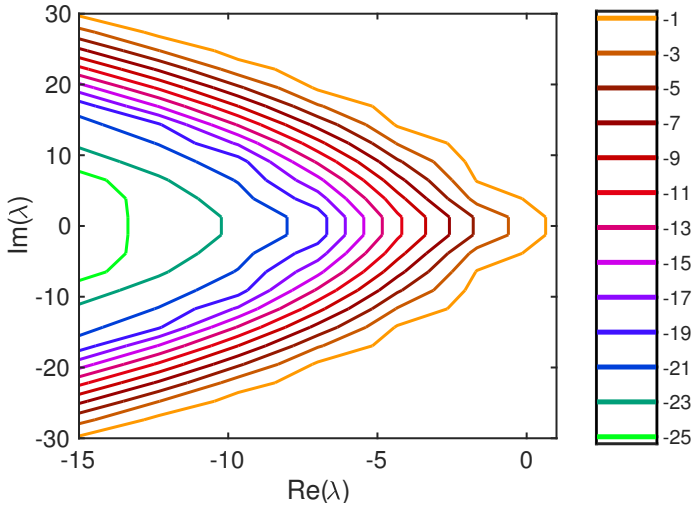

Figure 2.11: Pseudospectra of wave train in Barkley model. Contours indicate ϵ-pseudospectra in $\log_{10}$ scale.

Using eigenfunctions of the form $V(\xi) = e^{\eta\xi}W(\xi)$ where $W(\xi + 2\pi) = W(\xi)$, the weighted eigenvalue problem for $\eta \in \mathbb{R}$ becomes

$$\begin{aligned}\lambda W &= \mathcal{L}_\eta W \\ &= \kappa^2 D\left(\partial_\xi + \eta\right)^2 W + \omega\left(\partial_\xi + \eta\right) W + F_u(U_\infty)W.\end{aligned}$$

The spectrum of $\mathcal{L}_\eta$ is computed using $\eta = -8$, which is suggested from the spatial growth of unweighted eigenfunctions and the absolute spectrum. Eigenvalues from the weighted computation are shown in Figure 2.12a and align along the absolute spectra.

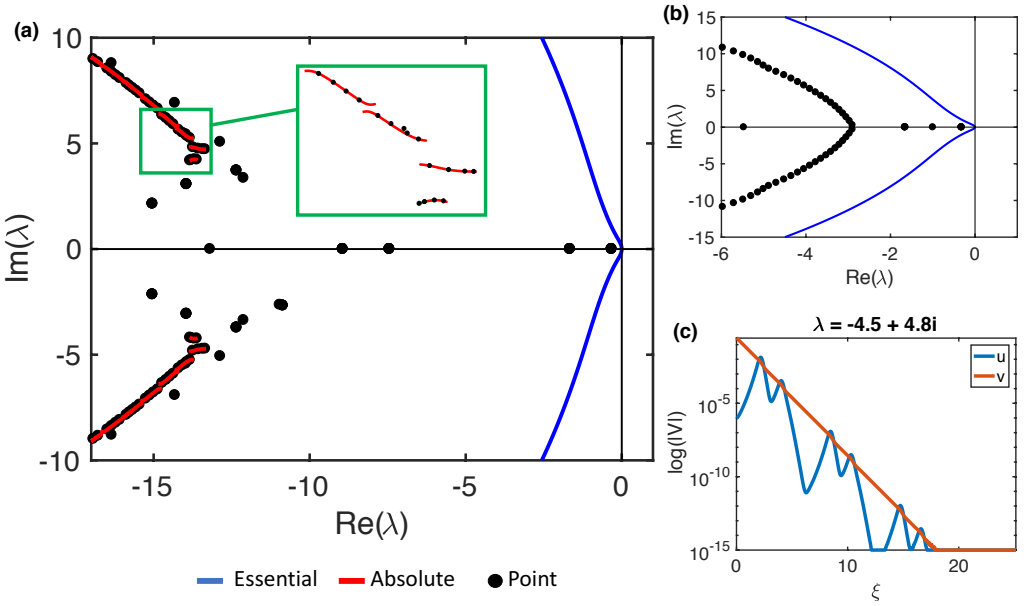

Figure 2.12: (a) Essential, absolute, and point spectra of wave train. Point spectra computed for weighted operator. (b) Spurious eigenvalues from unweighted operator approach parabolic curves resembling the essential spectrum. (c) Spatial growth of eigenfunctions highlighted with log-scale.

The full impact of unstable pseudospectra on spiral stability is not analyzed here, and the reader is referred to [54, 55] for further information about potential problems with pseudospectra. We do supply one final word of caution. Sparse eigenvalue solvers can be efficient ways to compute eigenvalues of large sparse matrices, such

as the Jacobian matrices for spiral waves. However, many of these iterative algorithms, including versions of the restarted Arnoldi algorithm implemented in the MATLAB function `eigs`, compute approximate eigenvalues from Krylov subspace projections and these subspaces can produce false eigenvalues [56]. Additionally, the iterative algorithms often use resolvent estimates as criteria for finding eigenvalues; for non-normal operators the resolvent estimates can generate spurious eigenvalues. Computational problems arising from pseudospectra may be mitigated by using the weighted eigenvalue problem defined above, but this topic is not explored further here.

Chapter Three

Mechanisms driving period-doubling instabilities in spiral waves

3.1 Introduction

Spiral wave patterns observed in models of cardiac arrhythmias and chemical oscillations develop alternans and stationary line defects (Figure 3.1), both of which can be thought of as period-doubling instabilities. These instabilities are observed on bounded domains, and may be influenced by the spiral core, far-field asymptotics, and boundary conditions. In this chapter, we utilize spectra concepts of patterns on bounded domains described in Chapter 2 and introduce a methodology to disentangle the impacts of each region on the instabilities by directly analyzing spectral properties of spiral waves and boundary sinks. In Section 3.5 we apply our technique to spirals formed in reaction-diffusion systems to investigate how and why alternans and line defects develop. Our results indicate that the mechanisms driving these instabilities are quite different; alternans are driven by the spiral core, whereas line defects appear from boundary effects. Moreover, we find that the shape of the alternans eigenfunction is due to the interaction of a point eigenvalue with curves of continuous spectra.

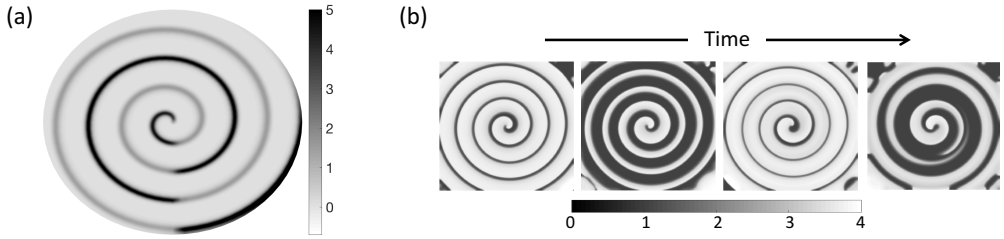

Figure 3.1: (a) Stationary line defect in the Rössler system. (b) Time evolution of alternans instability in the Karma model on square of side length 16 cm with homogeneous Neumann boundary conditions. System parameters as defined in Section 3.3

3.2 Summary of previous results for alternans and line defects

Due to the clinical significance, the alternans instability has been a recent area of focus in the cardiac dynamics community. In single cells, alternans are widely attributed to a period-doubling instability observed in simple 1D maps [57]. However, this condition known as the restitution hypothesis, has received contradictory evidence [16, 58] and does not appear to be relevant for excitable tissues that support traveling waves. The formation and stability of alternans in waves propagating on a ring and line have been analyzed with kinematic descriptions [59] and through linear stability analyses [60–63]. Stability analysis in 1D predicts alternans are the result of a Hopf bifurcation [64], yet analysis of the 1D traveling waves cannot fully capture 2D features.

Linear stability analysis of spirals on bounded domains in the Karma and Fenton-Karma models found a variety of unstable eigenmodes responsible for the formation of alternans [37, 38, 65]. In [38] and [65], Marcotte and Grigoriev find that formation of alternans depends on the domain size. Furthermore, they determine that the alternans eigenmodes are not spatially localized but found numerically that the adjoint eigenfunctions (response functions) are localized near the core.

The rigorous analysis of spiral waves in [33] indicates period-doublings are initiated by a series of Hopf bifurcations with imaginary parts of the eigenvalues robustly at multiples of half the spiral frequency. These Hopf eigenvalues may be induced by period-doubling of the far-field dynamics or boundary sinks. Stationary line defects are hypothesized to stem from bifurcations of the boundary sink, but no direct evi-

dence supporting this claim was found in [33].

The goal of this chapter is to further investigate how and why these period-doubling like instabilities arise on bounded domains. Specifically, we seek to answer whether the instabilities arise from the core, far-field dynamics, or boundary conditions to gain a better understanding of how the spirals destabilize and on what domains the instabilities are relevant. To tackle this problem, we introduce a methodology for disentangling the contributions of each region by forming related patterns on domains whose spectra will contain eigenvalues arising from a subset of the three regions. Three cases are considered and compared with essential and absolute spectra from wave trains: (1) a spiral on a bounded disk with Neumann boundary conditions to provide the full spectra, (2) a boundary sink to demonstrate effects of boundary conditions, and (3) a spiral on a disk with non-reflecting boundary conditions to capture core eigenvalues.

3.3 Description of Karma and Rössler models

Cardiac models range in complexity from biophysically detailed ion-channel models to simplified systems which capture qualitative features, with both categories falling under the reaction-diffusion framework. The Karma system is a two-variable reduction of the Noble ion-channel model [2] and was developed to be a simplified model that reproduces alternans [34, 66]. The model is given by

$$\begin{aligned} \partial_t u &= 1.1\Delta u + 400\left(-u + \left(1.5414 - v^4\right)\left(1 - \tanh(u-3)\right)\frac{u^2}{2}\right) \\ \partial_t v &= 0.1\Delta v + 4\left(\frac{1}{1-e^{-\mu_K}}\theta_s\left(u-1\right) - v\right), \end{aligned} \tag{3.1}$$

where the fast variable u represents voltage and v acts as a slower gating variable. As in [37, 38, 65], we consider a smoothed version of the Karma model where $\theta_s(u) = (1 + \tanh(su))/2$ for $s = 4$. Alternans are observed in planar spirals when the real bifurcation parameter μ_K is increased above 1 [66].

The Rössler model is commonly used to study chaotic turbulence in chemical oscillations, and is known to produce spirals with line defects. The three-variable system is also of the general reaction-diffusion form and is given by

$$\begin{aligned} \partial_t u &= 0.4\Delta u - v - w \\ \partial_t v &= 0.4\Delta v + u + 0.2v \\ \partial_t w &= 0.4\Delta w + uw - \mu_R w + 0.2. \end{aligned} \tag{3.2}$$

Bifurcations to line defects are observed for parameter value $\mu_R > 3$ [32, 33].

Here, we write both models in a general form and for notation purposes define the bifurcation parameters to be μ_K and μ_R, respectively. Standard forms of the models are presented in the chapter appendix (Chapter 3.7), and linked to typical system parameters in Table 3.1. With the exception of the bifurcation parameters, all other parameters are kept fixed in this study.

Both of these models are reaction-diffusion systems of the form

$$U_t = D\Delta U + F(U), \quad U \in \mathbb{R}^n, \quad D \in \mathbb{R}^{n\times n}, \quad x \in \mathbb{R}^2 \tag{3.3}$$

where $n = 2$ in the Karma model and $n = 3$ for Rössler and the diagonal diffusion matrix D has full rank.

3.4 Methodology

Following the framework outlined in Chapter 2, we consider (3.3) in the rotating polar coordinate frame $(r, \psi) = (r, \phi - \omega t)$ where spirals on bounded disks are equilibrium solutions of

$$U_t = D\Delta_{r\psi}U + \omega_R \partial_\psi U + F(U), \quad (r, \psi) \in [0, R) \times S^1 \tag{3.4}$$

$$\partial_r U(R, \psi) = 0, \ \psi \in S^1 \tag{3.5}$$

and associated periodic wave trains are stationary solutions in the frame $\xi = \kappa r - \omega t$ to

$$U_t = \kappa^2 D U_{\xi\xi} + \omega U_\xi + F(U), \quad \xi \in \mathbb{R}. \tag{3.6}$$

Alternans and line defects are observed on bounded domains, in particular on finite disks with homogeneous Neumann boundary conditions in numerical simulations. The instabilities are associated with eigenvalues destabilizing, and as laid out in Theorem 1 the spectrum of spirals on bounded domains is a union of eigenvalues from $\Sigma_{\text{abs}}(\mathcal{L}_*)$, $\Sigma_{\text{expt}}(\mathcal{L}_*)$, and Σ_{bdry}. To investigate which spectral sets these unstable eigenvalues belong to, we consider spirals formed on three domains, each of which captures instabilities from all or a subset of the three sets.

The first is the domain of interest; the standard bounded disk of radius R with homogeneous Neumann boundary conditions which we will denote $B_R(0)$. Here, spirals $U_{*,R}(r, \psi)$ are solutions of (3.4) and analysis of the operator

$$\mathcal{L}_{*,R}V = D\Delta_{r,\psi}V + \omega V_\psi + F_U(U_*)V \tag{3.7}$$

for eigenfunctions in the space $\{V(r,\psi) \in H^1([0,R], S^1) : V_r(R,\cdot) = 0\}$ provides spectral stability. From Theorem 1, the spectrum contains contributions from the core, far field and boundary sink captured by the Σ_{expt}, Σ_{abs}, and Σ_{bdry}, respectively.

Core instabilities associated with Σ_{expt} are analyzed by computing spirals on the bounded disk of radius R with non-reflecting boundary conditions, $B_R^{\text{nr}}(0)$. Non-reflecting boundary conditions mimic an infinite domain by matching the spiral to the asymptotic wave train on the boundary, allowing the spiral to naturally pass through it without interference. Non-reflecting spirals $U_{\text{nr}}(r,\psi)$ are solutions to

$$\begin{aligned} 0 &= D\Delta_{r,\psi}U + \omega\partial_\psi U + F(U), \quad (r,\psi) \in [0,R) \times S^1 \\ 0 &= \partial_r U(R,\psi) - \kappa\partial_\psi U(R,\psi), \quad \psi \in S^1, \end{aligned} \tag{3.8}$$

where the boundary condition is from taking derivatives of the asymptotic matching condition $U_{*,R}(R,\psi) = U_\infty(\kappa r - \omega t)$. The linear operator for the non-reflecting spirals $\mathcal{L}_{\text{R,nr}}$ is

$$\mathcal{L}_{\text{R,nr}}V = D\Delta_{r,\psi}V + \omega V_\psi + F_U(U_{\text{nr}})V \tag{3.9}$$

which acts on eigenfunctions in $\{V(r,\psi) \in H^1([0,R] \times S^1) : V_r(R,\psi) = \kappa V_\psi(R,\psi)\}$.

Finally, effects of the boundary and eigenvalues associated with Σ_{bndy} are captured by direct computation of the boundary sinks. The time T-periodic pattern U_{bdry} is posed on a two-dimensional spatiotemporal domain $\Omega_{\text{bdry}} = [-L,0] \times S^1$, which spatially has Neumann boundary conditions at $x = 0$ and is temporally 2π-periodic.

$U_{\text{bdry}}(x,t)$ is a solution to

$$U_t = \frac{T}{2\pi}\left[DU_{xx} + F(U)\right], \quad (x,t) \in [-L,0) \times S^1 \tag{3.10}$$

$$U_x(0,t) = 0, \ t \in S^1. \tag{3.11}$$

Stability of the boundary sink is given by considering the operator

$$\mathcal{L}_{\text{bdry}} V = -V_t + DV_{xx} + F_U(U_{\text{bdry}})V \tag{3.12}$$

on the space $\{V(x,t) \in H^1([-L,0] \times S^1) : V_x(0,\cdot) = 0\}$. Boundary sinks for the Rössler and Karma models are shown in Figures 3.3a and 3.6b and these will be discussed in further detail below.

Boundary sinks have far-field dynamics and boundary conditions, but lack the core, whereas conversely, non-reflecting spirals contain the core but lack outer boundary effects. On each domain, the patterns of interest are equilibrium solutions, and stability properties are given by spectra of the operator linearized around the solution. Comparing the spectra of these three operators will indicate which region and spectral set is responsible for observed instabilities. We expect all operators to have discrete eigenvalues aligning along the absolute spectrum due to the far-field dynamics, but the spectrum of $\mathcal{L}_{\text{bdry}}$ will not contain isolated core eigenvalues from $\Sigma_{\text{expt}}(\mathcal{L}_*)$, and $\mathcal{L}_{\text{R,nr}}$ will not have eigenvalues from the boundary sink. We remark that for non-reflecting boundary conditions in $\mathcal{L}_{\text{R,nr}}$ discrete eigenvalues from the far-field will still converge to the absolute spectrum. These expectations are summarized in the following lemma.

Lemma 1. *For the operators defined above, the isolated spectra Σ_{isle} is comprised of the following sets where $\mathcal{L}_*$ is the linear operator on $L^2(\mathbb{R}^2)$ with domain $H^1(\mathbb{R}^2)$*

defined in (2.14).

1. *Bounded disk:*

$$\Sigma_{isle}\left(\mathcal{L}_{*,R}\right) = \Sigma_{expt}\left(\mathcal{L}_{*}\right) \cup \Sigma_{bdry}$$

2. *Non-reflecting disk:*

$$\Sigma_{isle}\left(\mathcal{L}_{R,nr}\right) = \Sigma_{expt}\left(\mathcal{L}_{*}\right)$$

3. *Boundary sink:*

$$\Sigma_{isle}\left(\mathcal{L}_{bdry}\right) = \Sigma_{bdry}.$$

3.4.1 Numerical methods for boundary sinks

The patterns and spectra of each operator are computed numerically in Matlab. Patterns are formulated as equilibrium solutions on the proper domains, and the equation $\mathcal{F}(U) = 0$ is solved using Matlab's built-in root finding algorithm `fsolve`.

Periodic wave trains, spirals on disk domains, and spectra of the linear operators are computed using the methods defined in Chapter 2.

The rectangular domain Ω_{bdry} was similarly discretized using fourth-order centered finite differences with N_s grid points in the spatial direction and a Fourier spectral method with N_t grid points in the periodic temporal direction. Following the methods and terminology in [67, 68], the boundary sink is numerically computed by decomposing the domain into a "far-field" region in which the asymptotic wave train is translated in time and space and a "core" region where the Neumann boundary

condition has an effect on the wave shape. Note that in this case the core refers to the area near the boundary. The pattern in the far-field region is fixed by the spatial wave number and frequency of the spiral wave. Smooth cut-off functions, $\chi(x) = 1/2\,(1 + \tanh(x - d))$, match the solution in the far-field $U_{\text{wt}}(x,t)$ and core $W(x,t)$. The full solution is given by

$$U_{bdry}(x,t) = \chi(x)U_{wt}(x,t) + (1 - \chi(x))\,W(x,t).$$

Substituting the form of U_{bdry} into (2.4) allows for $W(x,t)$ to be calculated with Newton's method. To account for numerical inaccuracies, the temporal period is set as a free parameter and an integral phase condition is added to match the U_{wt} and W solutions. That is, computing boundary sinks amounts to solving the system

$$\begin{aligned}
&-\frac{2\pi}{T}\partial_t U_{\text{bdry}} + D\partial_{xx}U_{\text{bdry}} + F\left(U_{\text{bdry}}\right) = 0, \quad (x,t) \in (-L,0) \times [0,2\pi) \\
&\partial_x W(0,t) = 0, \quad t \in S^1 \\
&\int_0^{2\pi/\kappa} \int_0^{2\pi} \partial_x U_{wt}(x,t) W(x,t)\; dt\; dx = 0
\end{aligned}$$

for $W(x,t)$ where the temporal direction is scaled to be 2π-periodic.

Solutions in the far-field are obtained by translating asymptotic wave trains in time and space using the angular frequency and spatial wave number from the spiral and imposing the cutoff function $\chi(x)$. Applying $(1 - \chi(x))$ to the translation yields an initial condition for $W(x,t)$. Domain sizes were selected to fit 6 periods of the wave train, which accurately captured both the Neumann boundary conditions and convergence to the far-field dynamics. Asymptotic wave trains were computed from the one-dimensional problem (3.6) using Fourier spectral methods on a periodic grid of N_t points. The translation of wave train to boundary sink resulted in $N_s = 6N_s$.

To take spatial derivatives, the pattern was initially posed on a larger spatial grid of 8 periods with Neumann boundary conditions on each end. When solving for the final pattern, the left two periods were removed to eliminate left-hand side boundary effects and simulate a half-infinite line.

3.5 Results

Spirals on each domain are numerically calculated for the Karma and Rössler models, and the influence of the spiral regions is determined by comparing the spectra of the three operators $\mathcal{L}_{*,R}$, $\mathcal{L}_{\mathrm{R,nr}}$, and $\mathcal{L}_{\mathrm{bdry}}$.

3.5.1 Rössler Model: Line defects are driven by the boundary

At the onset of period doubling, point eigenvalues with imaginary parts approximately equal to $\frac{\omega}{2} + \ell\omega$, $\ell \in \mathbb{Z}$ destabilize, followed by branches of essential and then absolute spectra upon increasing μ_R further. The unstable eigenfunctions are localized at the boundary (Figure 3.2), indicating that line defects are a result of instabilities of the boundary conditions. The spectra of $\mathcal{L}_{*,R}, \mathcal{L}_{\mathrm{R,nr}}$, and $\mathcal{L}_{\mathrm{bdry}}$ are compared in Figure 3.3. As expected, all patterns have eigenvalues from the far-field dynamics aligning along the absolute spectrum. However, only domains with boundary conditions, that is the spiral on $B_R(0)$ and boundary sink on Ω_{bdry} contain the unstable line defect eigenvalues. Thus, the instability is confirmed to arise from the boundary conditions, and a bounded domain is necessary for the defects to occur.

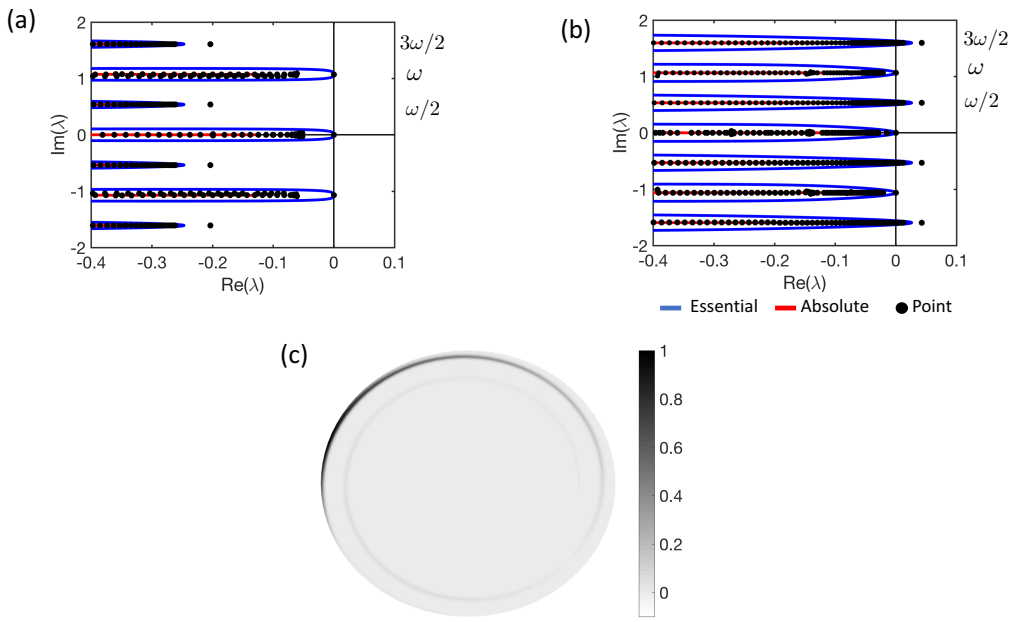

Figure 3.2: Rössler Model: (a) Spectra for stable spiral, $\mu_R = 2$. Labels on right side of imaginary axis indicate half-multiples of angular frequency. (b) Spectra of unstable spiral, $\mu_R = 3.4$, (c) Unstable point eigenfunction responsible for line defects with $\mu_R = 3.4$. Corresponds to eigenvalue $\lambda = 0.043 + 0.54i = 0.043 + \omega/2i$.

For one final test of the boundary influence, the boundary conditions can be modified by changing κ in equation (3.8); $\kappa = 0$ corresponds to homogeneous Neumann conditions and $\kappa = \kappa_*$ is non-reflecting. Therefore, we can start at $\kappa = 0$ with the homogeneous Neumann boundary spiral from $B_R(0)$, numerically continue in κ until reaching the spatial wave number of the spiral κ_* and track the evolution of an unstable eigenvalue. The spiral is already formulated as a root finding problem, and the eigenvalue problem can be as well by solving $\mathcal{L}_{\mathrm{R,nr}}V - \lambda V = 0$. Each continuation stage is a 2-step process. First, a new spiral with updated boundary conditions is computed, and second the linearized operator, $\mathcal{L}_{\mathrm{R,nr}}$, is modified and eigenpair (λ, V) solved for. Starting the continuation at $\kappa = 0$ allows the unstable eigenfunction from $\mathcal{L}_{*,R}$ to be used in the first continuation step. If the eigenvalue is unchanged with the boundary continuation, then it does not originate from the boundary sink.

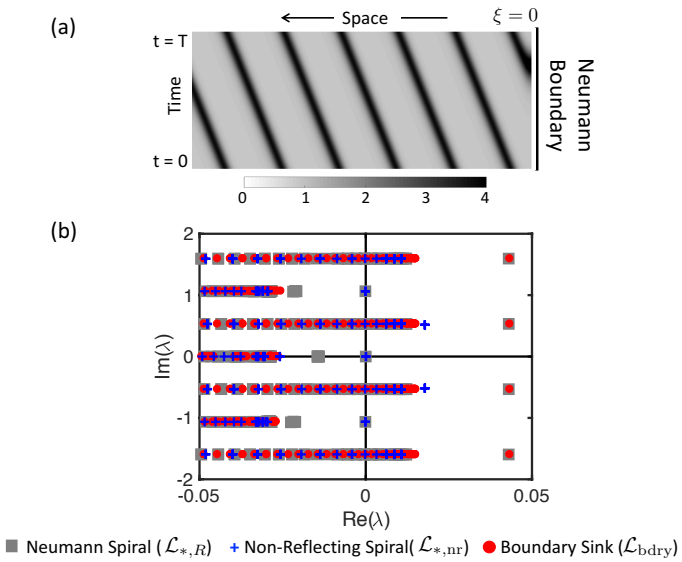

Figure 3.3: Rössler Model: (a) Image of boundary sink. Neumann boundary conditions on the right at $\xi = 0$. Domain is periodic in time (vertical) direction. (b) Spectra of operators $\mathcal{L}_{*,R}$, $\mathcal{L}_{R,\mathrm{nr}}$, $\mathcal{L}_{\mathrm{bdry}}$.

Figure 3.4 shows the evolution of the point eigenvalue during the κ-continuation. The eigenvalue changes with κ, first tracking along the essential spectrum, and then jumping on the absolute spectrum. Increasing κ corresponds to a mixed boundary condition and results in different shapes of unstable eigenfunctions, demonstrating that the boundary conditions will change the observed instability. The eigenfunctions in Figure 3.3(b) show the transition from localization at the boundary to localization at the core as κ is increased from 0 to κ_*. Similar results are obtained for unstable point eigenvalues at other multiples of $i\frac{\omega}{2} + i\omega\ell$ as these eigenvalues arise due to the $e^{i\ell\psi}V(r,\psi)$ symmetry of the eigenfunctions.

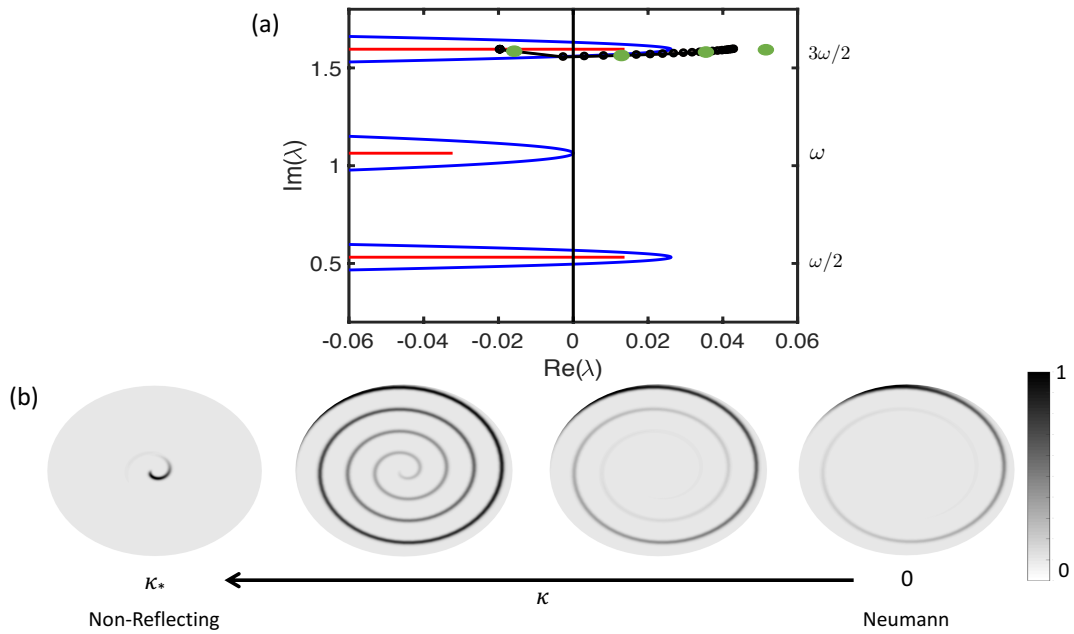

Figure 3.4: Rössler Model: (a) Boundary condition continuation of line defect eigenvalue (black curve), starting with $\kappa = 0$ on the right and ending on absolute spectrum with $\kappa = \kappa_*$. (b) Eigenfunctions from continuation. Locations of eigenvalues indicated by green circles on eigenvalue continuation in (a). Eigenfunctions are on a disk of radius $R = 125$.

3.5.2 Karma Model: Alternans are driven by the core

As the bifurcation parameter μ_K is increased above 1 in the Karma model, the essential spectrum destabilizes in an Eckhaus instability, followed by a single complex-conjugate pair of eigenvalues with imaginary part near $3\omega/2$. Meandering and alternans appear with the Hopf bifurcation from the point eigenvalues. Shown in Figure 3.5d, the unstable point eigenfunction, and hence the form of the instability, has highest magnitude at the boundary of the spiral bands, leading to the observed alternans.

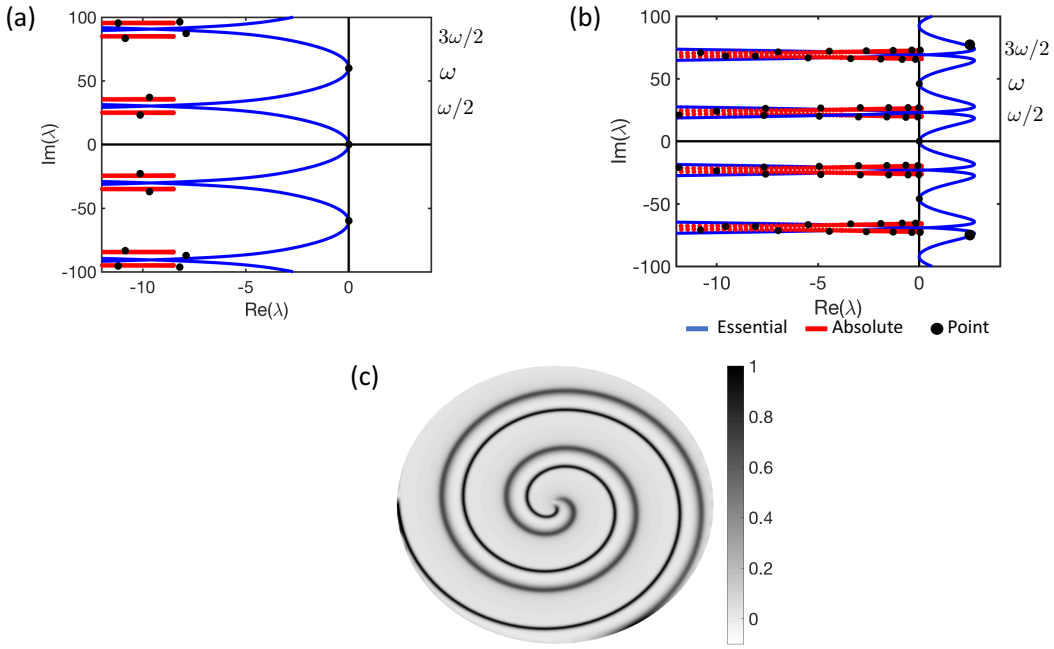

Figure 3.5: Karma Model: (a) Spectra for stable spiral, $\mu_K = 0.6$. Labels on right side of imaginary axis indicate half-multiples of angular frequency. (b) Spectra of unstable spiral, $\mu_K = 1.4$, (c) Unstable point eigenfunction responsible for alternans. Corresponds to eigenvalue $\lambda = 2.6 + 75.9i \approx 2.6 + 3\omega/2i$, $\mu_K = 1.4$. Domain radius $R = 5$ with homogeneous-Neumann boundary conditions.

The single pair of eigenvalues suggests they arise from Σ_{expt} and are instabilities of the core. In this case, comparison of the three operators indicates alternans eigenvalues are present in the spiral spectra for $\mathcal{L}_{*,R}$ and $\mathcal{L}_{\text{R,nr}}$, but are absent in the boundary sink $\mathcal{L}_{\text{bdry}}$. Modification of the boundary conditions in $B_{\text{R,nr}}(0)$ by continuing κ results in no change to the alternans eigenvalue or eigenfunction. Furthermore, the pair is not emitted from the absolute spectrum; continuation of the absolute spectrum branch point λ_{bp} and alternans eigenvalue λ_A in parameter μ_K shows the difference $\text{Re}(\lambda_{bp}) - \text{Re}(\lambda_A)$ is positive over an appropriate range of parameter values (Figure 3.6c). Thus, the point eigenvalues causing the alternans instability stem instead from the unstable pair of eigenvalues originating from Σ_{expt} affiliated with the core.

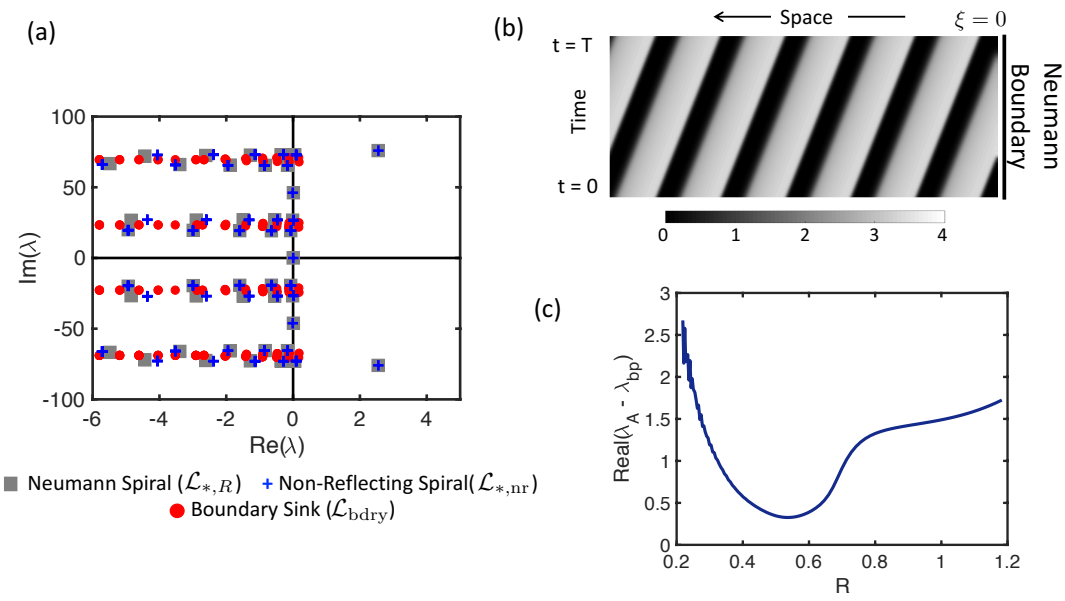

Figure 3.6: Karma Model: (a) Spectra of operators $\mathcal{L}_{*,R}$, $\mathcal{L}_{R,\mathrm{nr}}$, $\mathcal{L}_{\mathrm{bdry}}$. (b) Image of boundary sink. Neumann boundary conditions on right at $\xi = 0$. Periodic in time (vertical) direction. (c) Distance between real part of alternans point eigenvalue and branch point of absolute spectrum as a function of parameter μ_R.

3.5.3 Alternans from interaction of point and essential spectrum

More can be said about the alternans eigenfunction. To leading order in r, spiral eigenfunctions are of the form

$$V(r,\psi) = e^{\nu r} e^{i\ell\psi} \bar{V}(\xi), \quad \bar{V}(\xi + 2\pi) = \bar{V}(\xi)$$

and as the unstable alternans point eigenvalue passes through the essential spectrum, the eigenfunction inherits properties of the continuous spectrum [45]. In particular, Re ν is small when the eigenvalue is near the essential spectrum, with Re ν positive (negative) for the eigenvalue to the left (right) of the continuous spectrum curve. Small Re ν indicates little radial growth, and Im $\nu = \gamma$ is set by the essential

spectrum point. The wave train eigenfunction is determine by the eigenfunction on the essential spectrum, V_{ess}. Using these observations, the spiral eigenfunction to leading order in the radius is given by

$$V(r,\psi) = e^{i\gamma r} e^{\ell\psi} V_{ess}(\kappa r + \psi). \tag{3.13}$$

A numerically constructed eigenfunction is shown at the top of Figure 3.7a. Note that the derivative of the wave train $\partial_\xi U_\infty(\xi)$ is the eigenfunction on the essential spectrum with eigenvalue $\lambda = i\ell\omega$, $\ell \in \mathbb{Z}$. The alternans eigenfunction crosses Σ_{ess} near one of these points, and therefore $V_{ess}(\xi)$ is close to $U'_\infty(\xi)$ (Figure 3.7b). The derivative of the wave train is the highest at the wave fronts and backs and it is this shape that leads to the changing width of the spiral bands and form of alternans. Moreover, the structure of the constructed eigenfunction is in good agreement with the alternans eigenfunction from $\mathcal{L}_{*,R}$ which is reproduced on the bottom of Figure 3.7a.

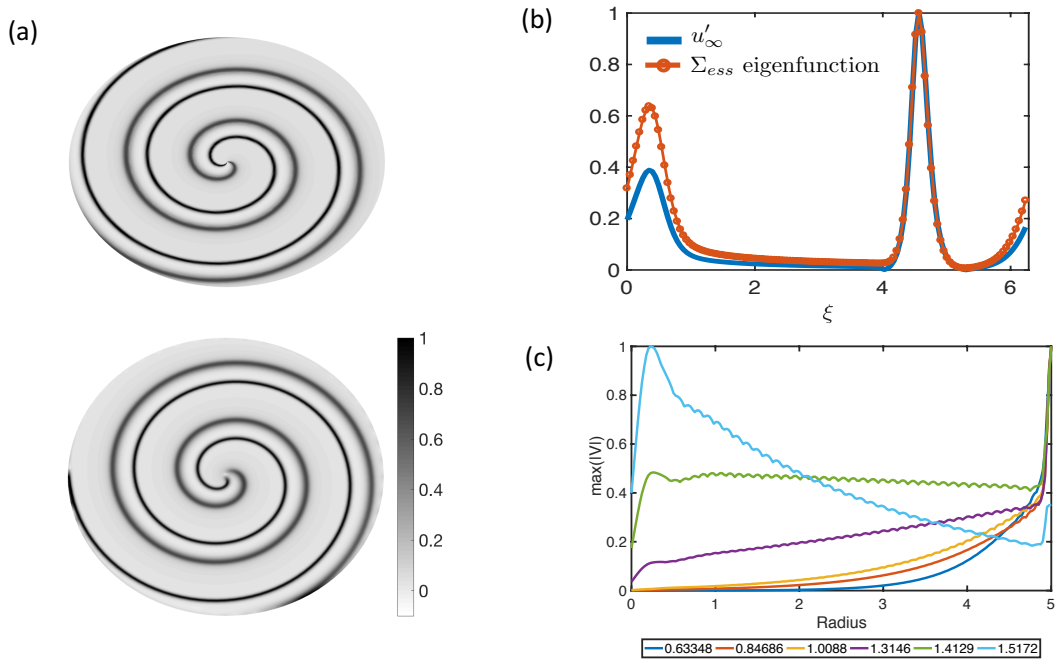

Figure 3.7: (a) Karma model alternans eigenfunction constructed from essential spectrum data. (b) Comparison between derivate of wave train (blue) and essential spectrum eigenfunction (orange dots), (c) Radial growth of alternans eigenfunctions. Legend indicates value of bifurcation parameter μ_K.

When the alternans eigenvalue is to the left of the essential spectrum, approximately $\mu_K < 1.4$, the overall shape of the eigenfunction is comparable to those shown in Figure 3.7c, but there is slight radial growth toward the boundary, corresponding to a spatial eigenvalue, ν, with a small positive real part. Radial growth of the alternans eigenfunction for several values of bifurcation parameter μ_K is shown in Figure 3.6c. As the eigenvalue approaches the essential spectrum, radial growth decreases and is near zero for μ_K near 1.4. Alternans appear when this eigenvalue first destabilizes, but the strength of the instability on the core and far-field regions is determined by the proximity of the point eigenvalue to the essential spectrum.

3.6 Discussion

Instabilities in patterns observed on finite domains may be initiated by unstable eigenvalues stemming from a variety of sources. Determining where unstable eigenvalues originate from yields insight into if and how the instabilities manifest on bounded domains. Here, we present a methodology for unfolding the origin of these eigenvalues and apply it to the specific case of period-doubling like instabilities in spiral waves on bounded disks. This technique of comparing the spectra of the three operators can be applied more generally to pattern forming systems on any domain, as long as the patterns of interest can be formulated as an equilibrium solution.

Our results predict that line defects in the Rössler model will only be seen on bounded domains, and the boundary shape and type of conditions will likely effect the structure of the instability. Similar types of boundary conditions can be formed by the interaction of the outer bands of multiple spirals. Line defects or similar structures may be generated in these situations.

We find that alternans are a product of unstable eigenvalues from Σ_{expt} associated with the spiral core, implying that as long as the core does not directly interact with the boundary, the domain shape and boundary conditions are insignificant factors in the spiral stability and formation of alternans. However, unstable point eigenfunctions do exhibit slight radial growth depending on the value of parameter μ_K, which may impact how prevalent alternans are on a small domain. These results are consistent with [38, 65] which finds that alternans development is most sensitive to perturbations near the core. The results also suggests that to destabilize an alternans spiral, perturbations must be applied to the core region.

Despite the bounded domain, the essential spectrum provides useful information about the source of the alternans instability. Alternans on a ring were previously attributed to destabilization of the continuous spectra [62]. We find that on a bounded disk, an unstable point eigenvalue passing through the Eckhaus unstable essential spectrum is fundamental to the alternans structure. Translational symmetry of the wave train ensures existence of the eigenvalue-eigenfunction pair $(\lambda = 0, V = U'_\infty)$, meaning that essential spectrum curves which passes through the origin must contain the origin. Therefore, these branches generically destabilize through an Eckhaus instability. Point eigenvalues that interact with these essential spectrum branches acquire an eigenfunction with shape close to U'_∞ which impacts the wave fronts and backs observed in the alternans instability.

In the Rössler model, point eigenvalues do not interact with unstable essential spectra branches and unstable continuous spectra branches do not pass through the origin. Our results suggest that alternans instability will appear if a point eigenvalue crosses essential spectrum that has destabilized through an Eckhaus instability. Future work includes investigation into whether an Eckhaus instability is necessary or sufficient for the formation of alternans. If the continuous spectrum can be attributed to formation of alternans, the 1D computation of the essential spectrum provides a tractable tool for analysis of more realistic and complex models.

There are a number of differences between the spectra of the two models. In the Rössler system, countably many discrete eigenvalues destabilize ahead of distinct period-doubling essential and absolute spectrum branches. In contrast, it is a single pair of unstable complex conjugate eigenvalues with imaginary part approximately $3\omega/2$ that leads to alternans. Generically, continuous spectra curves are symmetric around the lines $i\frac{\omega}{2} + i\omega\ell$, $\ell \in \mathbb{Z}$ which may take the form of smooth curves that

intersect with or coincide with symmetry lines, or disjoint branches that do not intersect [33]. The first case is observed in the Rössler system, and latter in Karma. Furthermore, in the Rössler system, the point $\mathrm{Im}(\lambda) = \frac{\omega}{2} + \omega\ell$ on the continuous spectra has spatial eigenvalue $\mathrm{Im}(\nu) = \kappa/2$, which corresponds with robust period-doubling of the far-field dynamics [33]. On bounded domains discrete eigenvalues limit to absolute spectra curves, meaning an unstable absolute spectra for the Rössler system will result in instabilities with temporal frequencies precisely $\omega/2 + \ell\omega$. On the other hand, the disjoint absolute spectrum branches in the Karma model result in an unstable absolute spectrum contributing many frequencies close to, but not specifically period-doubling.

In real cardiac systems, alternans lead to spiral break up, providing evidence they originate through a subcritical bifurcation [17, 69]. Numerical studies are inconclusive and show both immediate break up and short time alternans persistence [34, 66, 70]. In [64], alternans are analytically shown to originate in a subcritical Hopf bifurcation, but this analysis is limited and relies on a specific normal form for systems near a saddle node of a traveling wave and is not satisfied in all alternans generating models. The debate of a sub- versus super-critical bifurcation can be investigated in models by determining if an alternans spiral is stable when considered as a time-periodic three-dimensional structure on a bounded disk.

3.7 Chapter appendix

The standard form of the Karma model in the laboratory frame for $x \in \mathbb{R}^2$ is

$$E_t = \gamma \Delta E + \frac{1}{\tau_E}\left(-E + \left(E^* - n^M\right)(1 - \tanh(E - E_h))\frac{E^2}{2}\right)$$
$$n_t = \delta \Delta n + \frac{1}{\tau_n}\left(\frac{1}{1 - e^{-Re}}\theta_s\left(E - E_n\right) - n\right),$$

where $E = E(x,t)$ represents membrane voltage and $n = n(x,t)$ takes the place of a slower gating variable. In the notation of the main paper, the variables u and v represent E and n, respectively. The Heaviside function has been replaced by the smoothed function $\theta_s(u) = (1 + \tanh(su))/2$. Full parameter values are given in Table 3.1. The bifurcation parameter (typically called the restitution parameter), $\mu_K = Re$ is increased from 0.6 to 1.4 and controls recovery properties of the excitable media. All other parameters are held fixed in this study.

In the laboratory frame, the Rössler model is given by

$$u_t = \delta_1 \Delta u - v - w$$
$$v_t = \delta_2 \Delta v + u + av$$
$$w_t = \delta_3 \Delta w + uw - cw + b.$$

The bifurcation parameter c is increased from 2 to 3.4, with line defects appearing as $\mu_R = c$ passes through 3. Parameters are given in Table 3.1.

Karma	Rössler
$\gamma = 1.1$	$\delta_1 = 0.4$
$\delta = 0.1$	$\delta_2 = 0.4$
$\tau_E = 0.0025$	$\delta_3 = 0.4$
$\tau_n = 0.25$	$a = 0.2$
$E^* = 1.5414$	$b = 0.2$
$M = 4$	$\mu_R = c \in [2, 3.4]$
$s = 4$	$\omega \in [1.08, 1.06]$
$E_h = 3$	
$E_n = 1$	
$\mu_K = Re \in [0.6, 1.4]$	
$\omega \in [60.02, 46.13]$	

Table 3.1: Model parameters: Angular frequency ω is selected by spirals and given intervals align with bifurcation parameter.

Chapter Four

Behavior of continuous spectrum of spiral waves under zero diffusion limit

4.1 Introduction

It is common to use qualitative reaction-diffusion models to understand complex biological and physical processes, and doing so has led to the understanding of spiral wave behaviors including meander and drift. Indeed, this is what we did in Chapter 3 when we applied the spectral analysis techniques to the Karma and Rössler models to learn about alternans and line defects. Moving forward, we want to be able to apply the spectral results to biologically realistic ion-channel models. Even though both ion-channel and qualitative models are reaction-diffusion systems of the form

$$U_t = D\Delta U + F(U), \quad U \in \mathbb{R}^n, \quad D \in \mathbb{R}^{n\times n}, \quad x \in \mathbb{R}^2,$$

there are some key differences. As each equation represents a combination of processes in qualitative models, it is typical for each variable to have positive diffusion, whereas in ion channel models, often one or more species do not diffuse. That is, one or more elements δ_i of the diagonal diffusion matrix D are $\delta_i = 0$. In previous studies, small unphysical diffusion has been added to these components, but the effect this change has on the spectral properties of spiral waves has not been studied. We would expect the continuous spectra should change smoothly as $\delta_i \to 0$, and this is true for the 1D periodic wave trains [71]. Yet, we observe that the continuous spectra for spiral waves has very different limiting behavior as $\delta_i \to 0$, with a discontinuity occurring at $\delta_i = 0$. Figure 4.1 shows the continuous spectra for the two-variable Barkley Model with $\delta_2 = 0.2$ and $\delta_2 = 0$. In the first case, the spectral curves extend to $-\infty$, whereas in the latter, the curves remain bounded. Furthermore at the finite limit points, adjacent curves meet and form the cusps seen in Figure 4.1.

In this chapter, we explore how the essential spectrum for planar spiral waves

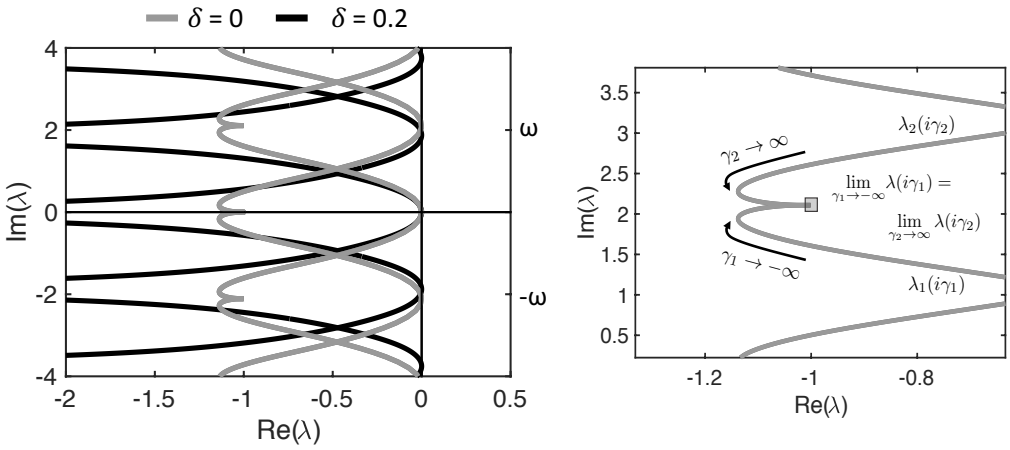

Figure 4.1: (left)Comparison of essential spectrum for the Barkley model with slow diffusing species having diffusion $\delta_2 = 0.2$ and $\delta_2 = 0$. (right) Shows how two branches for $\delta = 0$ limit to the same point (denoted by square) and form a cusp.

changes in the small δ_i limit and investigate the mechanisms responsible for the finite limit points observed in the diffusionless case. Furthermore, under mild conditions on the linearization of the reaction terms, we provide expressions for the spectra and eigenfunctions near the limit points. Our findings indicate the limit points are dictated by the non-diffusing species.

We proceed as follows: In Section 4.2, we state without proof the key results for bounds on and expansions of the eigenfunctions and continuous spectra. The results are applied to the Barkley model and checked numerically in Section 4.3 and implications discussed in Section 4.4. Proofs are given in Section 4.5.

4.2 Statement of key results

The focus is on spiral waves described by a two variable reaction-diffusion system $U = (u, v)^T$ set in a rotating frame with polar coordinates $(r, \psi) = (r, \phi - \omega t)$,

$$\begin{aligned} u_t &= \Delta_{r,\psi} u + \omega u_\psi + f(u, v) \\ v_t &= \delta \Delta_{r,\psi} v + \omega v_\psi + g(u, v). \end{aligned} \tag{4.1}$$

Under this framework, u and v are typically referred to as the fast and slow diffusing species. Many of the reduced systems, including the Barkley and Karma models, have two variables, and we remark that the results can be extended to higher dimensional systems by considering m_1 fast and m_2 slow or non-diffusing species, for $m_1 + m_2 = n$.

Recall that the essential spectrum of planar spiral $\lambda_*(\nu_*)$ waves only depends on the far-field dynamics [41] and is connected with the continuous spectra of the wave trains $\lambda_\infty(\nu_\infty)$ via the relation [44]

$$\lambda_*(\nu_*) = \lambda_\infty(\nu_\infty) - \omega\nu_\infty + i\omega\ell, \quad \nu_* = \kappa\nu_\infty, \ \ell \in \mathbb{Z}. \tag{4.2}$$

Note that since $\nu = i\gamma$, $\lambda_*(\nu_*)$ and $\lambda_\infty(\nu_\infty)$ only differ in the imaginary components and the spiral and wave trains have the same stability properties. Using relation (4.2), the essential spectrum of the spiral is given by curves $\lambda = \lambda_*(\nu_*)$ defined by

$$\lambda_* \tilde{V} = D\left(\kappa\partial_\xi + \nu_*\right)^2 \tilde{V} + \omega\partial_\xi \tilde{V} + F'\left(U_\infty(\xi)\right)\tilde{V} \tag{4.3}$$

where $\nu_* = i\gamma_*$, $\gamma_* \in \mathbb{R}$. Thus, the equations for the essential spectrum of the planar spiral wave are

$$\begin{aligned} \lambda_* u &= (\kappa\partial_\xi + \nu_*)^2 u + \omega\partial_\xi u + f_u\left(U_\infty(\xi)\right) u + f_v\left(U_\infty(\xi)\right) v \\ \lambda_* v &= \delta\,(\kappa\partial_\xi + \nu_*)^2 v + \omega\partial_\xi v + g_u\left(U_\infty(\xi)\right) u + g_v\left(U_\infty(\xi)\right) v, \end{aligned} \tag{4.4}$$

where γ_* parameterizes the essential spectrum curves. The observed changes in the essential spectrum are for values of $|\gamma_*|$ large (see Figure 4.1). To focus on the limiting behavior (and the area near the cusp point for $\delta = 0$), divide (4.4) by γ_*^2, define $\alpha = 1/\gamma_*$, and group by orders of α

$$-u + \alpha\,(2i\kappa u_\xi) + \alpha^2\left(\kappa^2 u_{\xi\xi} + \omega u_\xi + f_u(U_\infty)u + f_v(U_\infty)v - \lambda u\right) = 0 \tag{4.5}$$

$$-\delta v + \alpha\,(2i\delta\kappa v_\xi) + \alpha^2\left(\delta\kappa^2 v_{\xi\xi} + \omega v_\xi + g_u(U_\infty)u + g_v(U_\infty)v - \lambda v\right) = 0. \tag{4.6}$$

We consider values of α in the interval $[0, \bar{\alpha}]$ where $\bar{\alpha} \ll 1$, which corresponds to tails of essential spectrum curves. Theorems 2, 3, and 4 analyze the continuous spectrum using the formulation of equations (4.5 - 4.6).

Theorem 2 shows the existence of the u-eigenfunction and proves that regardless of the diffusion coefficient δ the magnitude of the u-eigenfunction will decay along the essential spectrum like α. Theorems 3 and 4 provide bounds on the v-eigenfunctions for the cases $\delta = 0$ and $\delta > 0$. Bounds from these theorems are used in Corollary 4.1 to find analytic expansions for the essential spectrum and eigenfunctions near the limit points. Proofs of theorems and corollaries are presented in section 4.5. Further assumptions and notations used in the theorems are defined in Hypothesis 1.

Hypothesis 1. *Assume the following:*

1. *$U_*(r,\psi) = (u_*(r,\psi), v_*(r,\psi))^T$ is a spiral wave solution to (4.1) with rotational frequency ω, spatial wave number κ, and associated asymptotic wave train $U_\infty(\xi)$.*
2. *The linearization $g_v(U_\infty)$ is a constant, which we will denote as $\bar{g} = g_v(U_\infty)$.*

The second condition in Hypothesis 1 is necessary for the forms of the analytic expansions given in Corollary 4.1.

Define the function spaces

$$
\begin{aligned}
X^0 &= \mathcal{C}^0\left([0,2\pi],\mathbb{C}\right), \\
X^1_{per} &= \left\{u \in \mathcal{C}^1\left([0,2\pi],\mathbb{C}\right) : u(0) = u(2\pi),\ u'(0) = u'(2\pi)\right\}, \\
X^2_{per} &= \left\{u \in \mathcal{C}^2\left([0,2\pi],\mathbb{C}\right) : u(0) = u(2\pi),\ u'(0) = u'(2\pi),\ u''(0) = u''(2\pi)\right\}.
\end{aligned}
$$

The desired eigenfunctions will be in the space X^2_{per}.

Theorem 2. *Under the conditions of Hypothesis (1) and assuming that $v \in X^0$ is a given function we have the following*

1. *There exists a unique u-eigenfunction $u \in X^2_{per}$ which is a solution of (4.5). The eigenfunction u is defined by the solution operator $u(\xi) = \mathcal{S}_{\alpha,\lambda}[v](\xi)$ which is linear in the given function v.*
2. *The u-eigenfunction has the following bounds*

$$||u||_\infty \leq \alpha\ K\ ||v||_\infty. \tag{4.7}$$

where $K < \infty$ is a real constant independent of α.

3. *Furthermore,* $u = 0$ *for* $\alpha = 0$ *and*

$$\left|\frac{d}{d\lambda}\mathcal{S}_{\alpha,\lambda}[v]\right| \leq K\alpha^{3/2}||v||_\infty$$

Theorems 3 and 4 yield similar results for the existence of and bounds on the v-eigenfunction in the cases $\delta = 0$ and $\delta > 0$, respectively. The cases are separated for clarity and because the proofs will use slightly different techniques. The solution operator $\mathcal{S}_{\alpha,\lambda}[v]$ and the bounds from Theorem 2 will be heavily used in the proofs of the theorems for the v-eigenfunctions.

Theorem 3. *Under the conditions of Hypothesis (1) and with* $u(\xi) = \mathcal{S}_{\alpha,\lambda}[v] \in X^2_{per}$ *as defined by the solution operator in Theorem 2, for* $\delta = 0$*;*

1. *If* $\lambda = \lambda_*(\alpha)$*, then there exists a unique function* $v \in X^1_{per}$ *which is a solution to (4.6) which is defined by the solution operator* $v(\xi) = \mathcal{S}^{v,0}_{\alpha,\lambda_*(\alpha)}[v_0](\xi)$ *and is linear in the initial condition* $v_0 = v(0)$*.*
2. $||v|| \leq K|v_0|$ *where* $K < \infty$ *is a constant independent of* α*,*

Theorem 4. *Assume the conditions of Hypothesis (1) and that* $u(\xi) = \mathcal{S}_{\alpha,\lambda}[v] \in X^2_{per}$ *as defined by the solution operator in Theorem 2. Then, for* $\delta > 0$*, if* $\lambda = \lambda_*(\alpha)$*, then there exists a unique function* $v \in X^2_{per}$ *which is a solution to (4.6). The v-eigenfunction is defined by the solution operator* $v(\xi) = \mathcal{S}^{v,\delta}_{\alpha,\lambda}(\xi)$*.*

Results from Theorems 2 - 4 reveal that the eigenfunctions and essential spectrum are continuous with respect to the parameter α. Therefore, for fixed values of δ we can write the eigenfunctions and eigenvalues as expansions in orders of α to investigate how diffusion modifies continuous spectra curves. Expansions are given in Corollary 4.1.

Corollary 4.1. *Under the conditions of Hypothesis (1) and with* $\delta = \alpha^2\beta^2$*, the essential spectrum curve* $\lambda = \lambda_*(\alpha, \beta)$ *and eigenfunctions* u*,* v *have the following expansions in parameters* α *and* β

$$\begin{aligned} u(\xi;\alpha,\beta) &= \alpha^2 f_v(\xi)e^{in\xi} + \alpha^2\beta f_v(\xi)e^{in\xi} + \alpha^2\beta^2 f_v(\xi)e^{in\xi} + \mathcal{O}(\alpha^3,\beta^3) \\ v(\xi;\alpha,\beta) &= e^{in\xi} + \alpha e^{in\xi} + \beta e^{in\xi} + \alpha\beta e^{in\xi} + \alpha^2 v_{20}(\xi) + \beta^2 e^{in\xi} + \mathcal{O}(\alpha^3,\beta^3) \\ \lambda(\alpha,\beta) &= \bar{g} + i\omega n + \alpha^2\frac{1}{2\pi}\int_0^{2\pi} g_u(s)f_v(s)ds - \beta^2 + \alpha^3\lambda_{30} + \mathcal{O}(\beta^3), \end{aligned}$$

where

$$\lambda_{30} = \frac{\kappa n}{\pi}\int_0^{2\pi} g_u(s)f_v(s)ds - \frac{i\kappa}{\pi}\int_0^{2\pi} g_u(s)f_v'(s)ds.$$

Moreover, for $\delta > 0$ $Re(\lambda) \to -\infty$*, and in the case* $\delta = 0$*, the essential spectrum will limit to the finite point*

$$\lambda_0 = \bar{g} + i\omega n.$$

Theorems 2 - 4 and Corollary 4.1 yield additional insights into the nature of the limit point, λ_0. Using the eigenfunction bound from Theorem 2 with $\delta = 0$, the leading order in α terms in the v-equation are

$$\lambda v = \omega v_\xi + g_v v,$$

and we see that the v-equation is completely decoupled from the rest of the system, with solution $\lambda = \lambda_0$, $v(\xi) = e^{in\xi}$. Furthermore, the only α dependence - the term that defines the continuous spectrum - comes in through the $\mathcal{O}(\alpha)$ u-term. Thus, the continuous spectrum can be thought of as an $\mathcal{O}(\alpha)$-perturbation of this linear

first-order equation, and it is the non-diffusive species that controls the limit point. The proofs of Theorems 3 and 4 and Corollary 4.1 will show that λ_0 is selected by enforcing periodic boundary conditions of the v-eigenfunction.

4.3 Application to Barkley Model

The Barkley model is a nonlinear reaction-diffusion system used to qualitatively study properties of spiral meander and drift [19, 20]. Even though the Barkley model is a qualitative system, we chose to investigate the effects of diffusion in this well studied system [19, 20, 46, 47] to emphasize the consequences. In this section, the results of Theorems 2, 3, and 4 and Corollaries 4.1 and 4.2 are applied to planar spiral waves formed in the Barkley model. The system is given by

$$u_t = \Delta u + \frac{1}{\epsilon} u\,(1-u)\left(u - \frac{v+b}{a}\right)$$
$$v_t = \delta \Delta v + u - v$$

and parameters are fixed at $a = 0.7$, $b = 0.001$, and $\epsilon = 0.02$. Under these conditions, there exists a stable spiral wave [18]. The effects of removing diffusion are studied by modifying the diffusion coefficient δ for the slowly diffusing species v in the interval $[0, 0.2]$. The angular frequency changes with δ and falls between $\omega = 1.87$ ($\delta = 0.2$) and $\omega = 2.09$ ($\delta = 0$).

Essential spectrum curves are calculated using numerical continuation methods described in Chapter 2 [53]. Computations are performed with Matlab on a 256 grid point periodic domain with Fourier spectral methods used for spatial derivatives. The computation provides an associated eigenfunction for each continuation point

on the spectral curve. Denote the eigenvalues and eigenfunction computed by continuation by λ_c and $V_c = (u_c, v_c)^T$. Below, these values will be treated as truth data and compared to the expansion results.

Figure (4.1) show essential spectrum curves of the spiral wave calculated for $\delta = 0$ and $\delta > 0$. Vertical periodicity of the branches arrises due to the Floquet symmetry of the spiral eigenfunctions. As noted above and as indicated in the theorems, the curves exhibit very different limits under the two conditions. For $\delta > 0$, the curves are unbounded and $|\lambda_*| \to \infty$. In the case $\delta = 0$, adjacent branches meet at the limit points λ_0 and form the cusps. The limit points are predicted to be $\lambda_0 = -1 + i\omega n$ from Corollary 4.1. Each branch contributes a distinct purely imaginary spatial eigenvalue, so at λ_0 there are spatial eigenvalues $\nu_1 = i\gamma_1$ and $\nu_2 = i\gamma_2$ with $\gamma_1 \to -\infty$ and $\gamma_2 \to \infty$.

Curves for decreasing δ are shown in Figure 4.2 with the inset focusing on the region near λ_0. For small, non-zero values of δ, curves begin to turn toward the λ_0 limit point before diverging. The value of $\mathrm{Re}(\lambda)$ for which the branch turns can be predicted using the expansions for $\lambda(\alpha, \beta)$.

Corollary 4.2. *To leading order in α, $Re(\lambda(\alpha, \beta))$ is locally maximized by $\alpha_* = \left(-\frac{\delta}{\lambda_{20}}\right)^{1/4}$, with local maximum given by*

$$\lambda_* = \lambda_0 + \alpha_*^2 \lambda_{20} - \frac{\delta}{\alpha_*^2}$$

where $\lambda_{20} = \frac{1}{2\pi}\int_0^{2\pi} g_u(s) f_v(s) ds < 0$.

This result is a direct consequence of finding the value of α which locally maximizes $\mathrm{Re}(\lambda(\alpha, \beta))$ using the expansion in Corollary 4.1. The local maximum of $\mathrm{Re}(\lambda)$ can

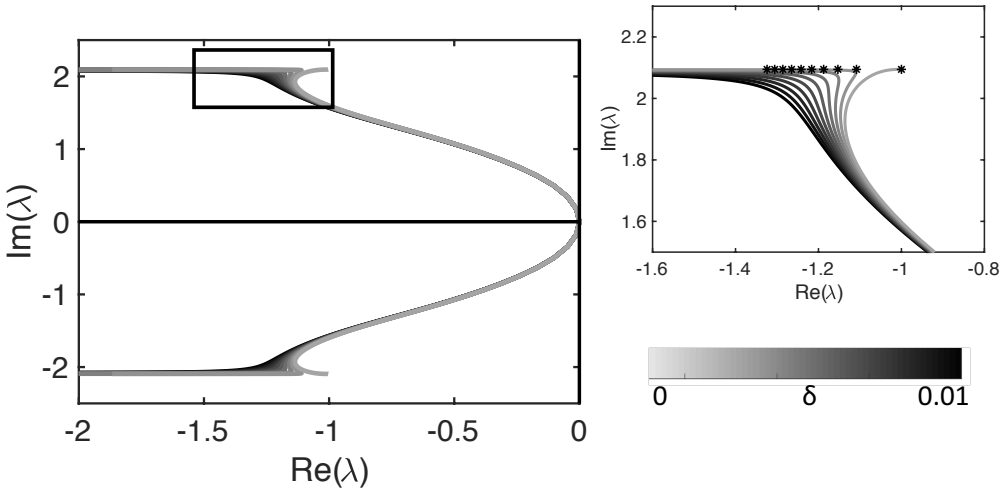

Figure 4.2: Essential spectrum for the Barkley model under changing diffusion. Inset at top right focuses on area near λ_0. Stars indicate the predicted local maxima given by Corollary 4.2.

be computed by applying Corollary 4.2 to the Barkley model. The predicted Re λ location of the maxima are indicated by stars in the inset of Figure 4.2.

The forms of the eigenvalue and eigenfunction expansions calculated in Corollary 4.1 are tested by analyzing convergence of λ_c and V_c. First, consider the case $\delta = 0$. In the $\lambda(\alpha, \beta)$ expansion, the leading order real and imaginary terms are $\mathcal{O}(\alpha^2)$ and $\mathcal{O}(\alpha^3)$, respectively. Therefore, we expect $\mathrm{Re}(|\lambda_c - \lambda_0|) \sim \mathcal{O}(\alpha^2)$ and $\mathrm{Im}(|\lambda_c - \lambda_0|) \sim \mathcal{O}(\alpha^3)$ and when plotted with α on a log-log axis, these relations should have slopes of 2 and 3. Log-log plots of the convergence are shown in Figure 4.3. Note that $\mathrm{Im}(|\lambda_c - \lambda_0|)$ does not follow $\mathcal{O}(\alpha^3)$ and instead mirrors $\mathcal{O}(\alpha^5)$. This leads to the following observation.

Corollary 4.3. *If the linearized term $g_u\left(U_\infty(\xi)\right)$ is a constant, then the order α^3 term in Im(λ) is 0.*

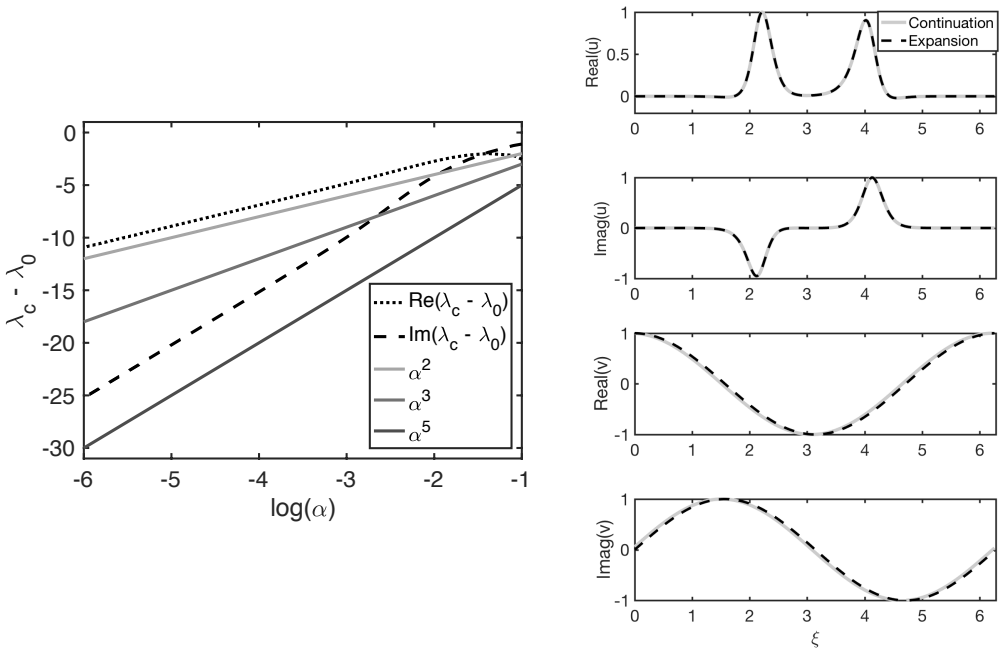

Figure 4.3: Convergence of essential spectrum and eigenfunction expansions for $\delta = 0$. (left) Convergence of real and imaginary parts of the essential spectrum computed with continuation in the Barkley model. (right) Comparison between eigenfunctions computed with continuation methods and expansions from Corollary 4.1.

Proof. Note that the $\mathcal{O}(\alpha^3)$ term of $\lambda(\alpha)$ can be written rewritten as

$$\frac{1}{2\pi}I(2\pi) + \frac{1}{2\pi}I_2(2\pi) = \frac{1}{2\pi}\left[(2 - 2\kappa n)\int_0^{2\pi} g_u(s)f_v(s)ds + 2i\kappa\int_0^{2\pi} g_u(s)f_v'(s)ds\right].$$

Since $g_u,\ f_v \in \mathbb{R}$, the imaginary part comes from the second integral. If g_u is a constant, the second term integrates to 0 by periodicity

$$2i\kappa\int_0^{2\pi} g_u(s)f_v'(s)ds = 2i\kappa g_u\left[f_v(2\pi) - f_v(0)\right] = 0.$$

□

The linearization g_u is constant in the Barkley model and Corollary 4.3 applies.

For a fixed $\delta > 0$, log-log plots of $\mathrm{Re}(|\lambda_c - \lambda_0|)$ and $\mathrm{Im}(|\lambda_c - \lambda_0|)$ show the $\mathcal{O}(\alpha^2)$

and $\mathcal{O}(\alpha^5)$ convergence that the expansions predict (Figure 4.4). To test the leading order β terms, we fix $\alpha > 0$ and continue in $\delta = \alpha^2\beta^2$. Decreasing δ corresponds to increasing β. For small δ (large β), the expansion indicates that $\mathrm{Re}(\lambda)$ will be dominated by $-\beta^2$. These predictions are confirmed in Figure 4.4, which shows that for fixed α $\mathrm{Re}(|\lambda_c - \lambda_0|) \sim \mathcal{O}(\beta^2)$.

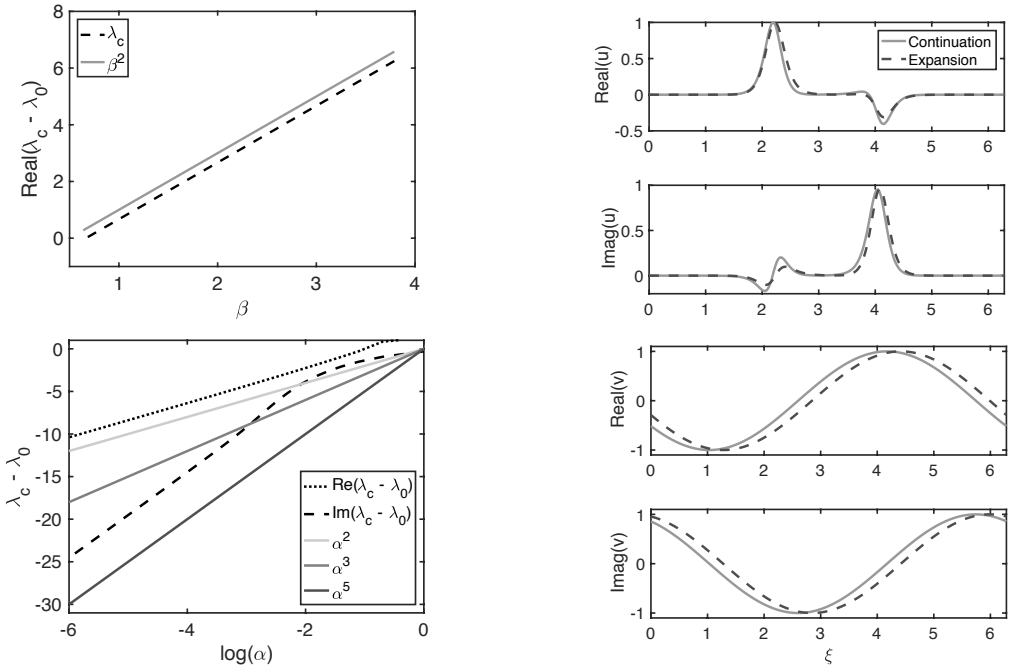

Figure 4.4: Convergence of essential spectrum and eigenfunction expansions for fixed $\delta > 0$. (left) Convergence of real and imaginary parts of the essential spectrum computed with continuation in the Barkley model. (right) Comparison between eigenfunctions computed with continuation methods and expansions from Corollary 4.1.

The eigenfunction expansions are computed through numerical integration of the expansion coefficients. Comparisons between the approximations and continuation eigenfunctions are shown in Figures 4.3 ($\delta = 0$) and 4.4 ($\delta > 0$). Eigenfunctions have been scaled to have maximum 1. The approximations capture the overall shapes remarkably well.

4.4 Discussion

The central question of this study is how and why the essential spectrum is modified in the limit of a diffusionless variable. We find a singular limit develops as $\delta \to 0$ resulting in unexpected limiting behavior of the continuous spectra. The spectra terminates at finite limit points which are predicted by Corollary 4.1 and are fixed by the diffusionless variable. Predictions of the theorems and corollaries are verified with the Barkley model.

These results focus on the continuous spectra of spiral waves formed in 2-variable reaction-diffusion systems on the plane. We expect similar results for general n-variable systems with m-diffusionless dimensions, with each diffusionless variable creating a limit point. Moreover, we predict the limit points will hold for a larger class of 2D patterns in reaction-diffusion systems that limit to a 1D periodic wave train. The periodic structure does appear to be necessary for the sudden spectral changes and plays a key role in determining the limit point in the proofs of Theorems 3 and 4 and Corollary 4.1.

Interestingly, cusp points are not observed for continuous spectra of the wave train. Figure 4.5 shows essential spectra for the wave train in the Barkley model for decreasing values of δ. For the spiral wave at $\delta = 0$, the limit points are a consequence of the v-equation decoupling from the system at small values of α and containing minimal influence from γ_*. Thus, the curves $\lambda = \lambda_*(\nu_*)$ are virtually independent of γ_* for large (small) γ_* (α). Now consider the linear dispersion relation for the wave train in the co-moving frame

$$\lambda_\infty V = D\left(\partial_\xi + \nu_\infty\right)^2 V + \omega\left(\partial_\xi + \nu_\infty\right)^2 V + F_U(U_\infty(\xi))V.$$

With $\delta = 0$ and $\nu_\infty = i\gamma_\infty$, the v-equation takes the form

$$\lambda_\infty v = \omega\left(\partial_\xi + i\gamma_\infty\right) v + g_u(\xi)u + \bar{g}v$$

and still retains input from γ_∞. Using the bounds from Theorem 2, the important terms are captured by the equation

$$\lambda_\infty v = \omega\left(\partial_\xi + i\gamma_\infty\right) v + \bar{g}v$$

which has solutions $v(\xi) = \exp\left[-\frac{1}{\omega}\left(i\gamma_\infty + \bar{g} - \lambda_\infty\right)\xi\right]$ and are periodic if $\lambda_\infty = \bar{g} + i(\omega n + \gamma_\infty)$. The periodic eigenfunctions enforces that $|\lambda_\infty| \to \infty$ as $|\gamma_\infty| \to \infty$.

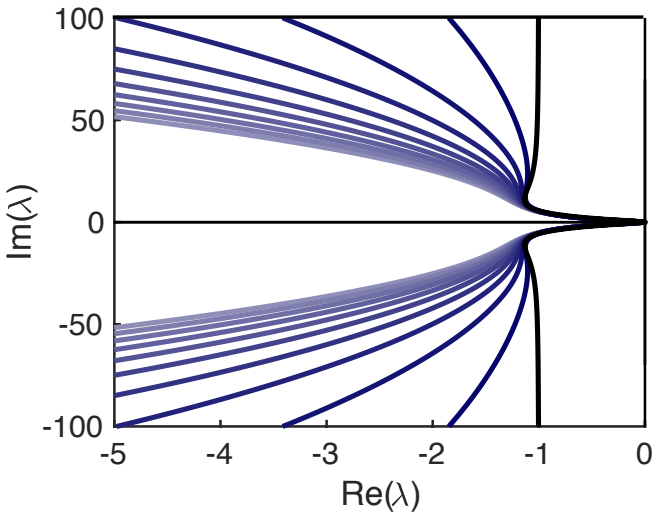

Figure 4.5: Essential spectrum of wave trains in the Barkley model limits to a vertical branch under $\delta \to 0$.

The infinite limit points for the wave train continuous spectra can be obtained directly from the spiral-wave train spectral relationship (4.2) as well. Furthermore, from relation (4.2) only the imaginary parts of the spectra differ between $\lambda_\infty(\nu_\infty)$ and $\lambda_*(\nu_*)$. In the limit $\alpha \to 0$ ($\gamma_* \to \infty$), we have $\mathrm{Re}(\lambda_*) \to g_v$, implying $\mathrm{Re}(\lambda_\infty) \to g_v$ and $\lambda_\infty(\nu_\infty)$ converges to a vertical line, which is observed in Figure 4.5. We recall that the spiral frame is equivalent to the stationary laboratory frame of the wave

trains. Therefore, the limit points obtained for the spiral wave hold for the wave train if computed in the laboratory frame.

Here, we investigate changes to the essential spectrum for planar spirals on unbounded domains. Similar changes are also seen for spectra on bounded disks, with spectra experiencing sudden discontinuous limits. In the case of a spiral truncated to a bounded disk, discrete eigenvalues are predicted to align along curves of the absolute spectrum [41, 44]. Numerical computations show the contrary, and instead eigenvalues cluster at the limit points of the essential spectrum (Figure 4.6). The limits of point spectra for spirals on a bounded disk remains an open question and a brief investigation of exponentially weighted spaces and Fredholm indices provides some insight into the problems that will need to be addressed.

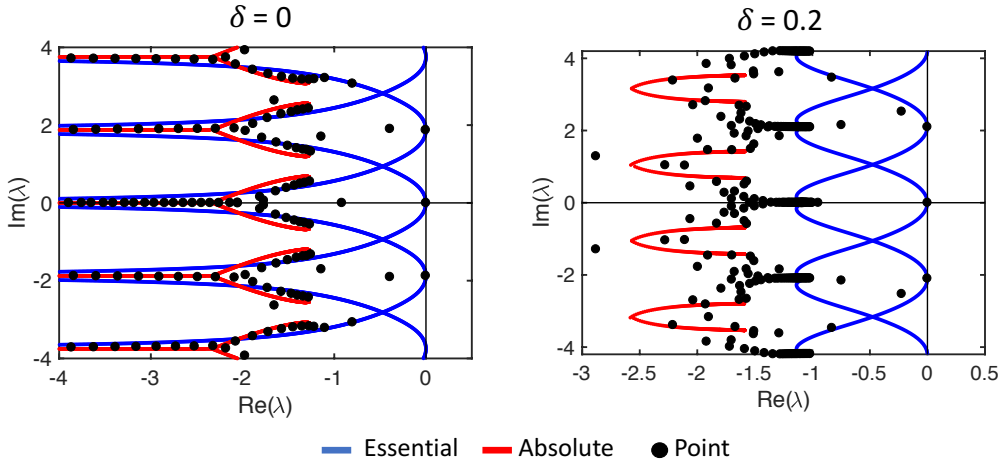

Figure 4.6: Essential, absolute, and point spectrum of spiral wave formed on bounded disk in the Barkley model under $\delta = 0.2$ and $\delta = 0$.

For values of λ such that Re $\nu_{-1} < \eta <$ Re ν_1 for $\eta \in \mathbb{R}$, the essential spectrum can be stabilized by considering an exponentially weighted space of the form

$$L^2_\eta(\mathbb{R}) := \left\{ u \in L^2\text{loc} : |u|_{L^2_\eta} < \infty \right\}, \quad |u|^2_{L^2_\eta} := \int_{\mathbb{R}} \left| u(x) e^{\eta x} \right|^2 dx.$$

The weight allows for unidirectional exponential growth of the eigenfunctions. Ana-

lytically, the exponential weight has the effect of the essential spectrum corresponding to at least one spatial eigenvalue with $\mathrm{Re}(\nu) = \eta$. That is $\nu = \eta + i\gamma$ is instead considered in the relation for $\lambda_*(\nu_*)$ [41, 43]. For $\delta = 0$, this takes the form

$$\begin{aligned}
\lambda_* u &= (\kappa\partial_\xi + \eta + i\gamma_*)^2 + \omega\partial_\xi u + f_u(U_\infty)\, u + f_v(U_\infty)\, v \\
\lambda_* v &= \omega\partial_\xi v + g_u(U_\infty)\, u + \bar{g} v.
\end{aligned}$$

Notice the weight η does not directly appear in the v-equation and the only influence will be through the $g_u(U_\infty)\, u$ term. In particular, exponentially weighted spaces will not impact the limit point λ_0, which is suggestive of absolute spectra at λ_0 [41, 43].

Upon crossing an essential spectrum curve, the real part of one spatial eigenvalue changes sign [41, 43]. In the case of $\delta > 0$, traversing the complex plane results in only crossing one branch at a time and changing the Fredholm index by one. However, for $\delta = 0$, two branches with distinct spatial eigenvalues meet at the cusp points. Consider moving from $\lambda_1 = -0.8 + 0.5i$ to $\lambda_2 = -1.5 + 0.5i$ along a straight line in the Barkley model. Now, crossing the one branch has the effect of crossing two and also changes the Fredholm index by two.

We leave the reader with a word of caution: the essential spectrum may be significantly different in the two cases of small positive and zero diffusion δ. This fact has potentially significant consequences for the stability of patterns formed in ion channel models, and care should be taken during computations. The effect on the spectrum for bounded domains remains yet unknown.

4.5 Proofs

The theorems are restated below for clarity. Recall the equations which determine the essential spectrum in the α-scaling are

$$u + \alpha\left(2i\kappa u_\xi\right) + \alpha^2\left(\kappa^2 u_{\xi\xi} + \omega u_\xi + f_u(U_\infty)u + f_v(U_\infty)v - \lambda u\right) = 0 \tag{4.8}$$

$$-\delta v + \alpha\left(2i\delta\kappa v_\xi\right) + \alpha^2\left(\delta\kappa^2 v_{\xi\xi} + \omega v_\xi + g_u(U_\infty)u + g_v(U_\infty)v - \lambda v\right) = 0. \tag{4.9}$$

We define the following function spaces which will be used in the proofs

$$\begin{aligned}
X^0 &= \mathcal{C}^0\left([0,2\pi],\mathbb{C}\right)\\
X^1 &= \mathcal{C}^1\left([0,2\pi],\mathbb{C}\right)\\
X^2 &= \mathcal{C}^2\left([0,2\pi],\mathbb{C}\right)\\
X^1_{per} &= \left\{u \in X^1 : u(0) = u(2\pi),\ u'(0) = u'(2\pi)\right\}\\
X^2_{per} &= \left\{u \in X^2 : u(0) = u(2\pi),\ u'(0) = u'(2\pi), u''(0) = u''(2\pi)\right\}.
\end{aligned}$$

The proofs of Theorems 2, 3, and 4 all follow a similar formula: the variation of constants method is used to construct an operator for the generalized solution of equations (4.8) and (4.9) by considering the v (u) eigenfunction as a heterogeneous forcing term. The operator is shown to be a uniform contraction on the space X^0 and the desired eigenfunctions are the unique fixed points defined by linear solutions operators. We then restrict to 2π-periodic functions in the periodic spaces X^1_{per} or X^2_{per} which will provide restrictions on constants in the generalized solution and values of λ. In the following, the constant $K \in \mathbb{R}$ is independent of α. Additionally, all norms refer to the infinity-norm, $||\cdot|| = ||\cdot||_\infty$.

Theorem 1 *Under the conditions of Hypothesis (1) and assuming that $v \in X^0$ is a given function we have the following*

1. *There exists a unique u-eigenfunction $u \in X^2_{per}$ which is a solution of (4.5). The eigenfunction u is defined by the solution operator $u(\xi) = \mathcal{S}_{\alpha,\lambda}[v](\xi)$ which is linear in the given function v.*
2. *The u-eigenfunction has the following bounds*

$$||u||_\infty \leq \alpha \; K \; ||v||_\infty.$$

   where $K < \infty$ is a real constant independent of α.
3. *Furthermore, $u = 0$ for $\alpha = 0$ and*

$$\left|\frac{d}{d\lambda}\mathcal{S}_{\alpha,\lambda}[v]\right| \leq K\alpha^{3/2}||v||_\infty$$

Proof. Fix $\lambda \in \mathbb{C}$ such that $|\lambda| \leq M < \infty$.

First, consider the case $\alpha = 0$. Then, equation (4.8) becomes $0 = -u$, and we have the trivial solution $u(\xi) = 0$.

Now, consider $0 < \alpha < \omega\kappa/(||f_u|| + M) = \bar{\alpha}$. Grouping the λu term in with the heterogeneous terms, we have the second order differential equation

$$0 = \alpha^2\kappa^2 u'' + \left(\alpha^2\omega + 2i\alpha\kappa\right) u' - u + \alpha^2 \left[f_u(\xi)u + f_v(\xi)v - \lambda u\right]$$

where $' = \frac{d}{d\xi}$. We will proceed by using variation of parameters to write the solution as a sum of a homogeneous and particular solution. The homogeneous solution is

found by calculating roots, $\eta_{1,2}$, of the characteristic equation

$$0 = \eta^2 + \left(\frac{\omega}{\kappa^2} + \frac{2i}{\alpha\kappa}\right)\eta - \frac{1}{\kappa^2\alpha^2}.$$

The roots are given by

$$\eta_{1,2} = -\frac{\omega}{2\kappa^2} - \frac{i}{\alpha\kappa} \pm \frac{\sqrt{\omega}}{2\kappa^2\sqrt{\alpha}}\left(\alpha^2\omega^2 + 16\kappa^2\right)^{1/4} e^{i\theta/2}$$

for $\theta = \tan^{-1}\left(\frac{4\kappa}{\alpha\omega}\right)$. Note that as $\alpha \to 0$, $\theta/2 \to \pi/4$. Moreover,

$$|\mathrm{Re}\,(\eta_{1,2})\,| \le K\left(\frac{1}{\sqrt{\alpha}}\right), \quad |\mathrm{Im}\,(\eta_{1,2})\,| \le K\left(\frac{1}{\alpha}\right),$$
$$\frac{1}{|\mathrm{Re}(\eta_{1,2})|} \le \frac{\sqrt{\alpha}}{2\sqrt{\kappa\omega}}, \quad \frac{1}{|\eta_2 - \eta_1|} \le \frac{\kappa^2\sqrt{\alpha}}{2\sqrt{\omega\kappa}}$$

with $\mathrm{Re}\,(\eta_1) > 0$ and $\mathrm{Re}\,(\eta_2) < 0$. As $\alpha \to 0$, the homogeneous solutions become increasingly oscillatory, which is compatible with $\gamma = 1/\alpha$ being the eigenfunction wave number. The homogeneous solution is given by

$$u_h(\xi) = c_1 e^{\eta_1(\xi - 2\pi)} + c_2 e^{\eta_2\xi}$$

where the exponential are written so that the solutions decay. Using variation of parameters, a particular solution is given by

$$u_p(\xi) = \frac{1}{\kappa^2(\eta_2 - \eta_1)}\left[- \int_{2\pi}^{\xi} e^{\eta_1(\xi - y)}\left[(f_u(y) - \lambda)u(y) + f_v(y)v(y)\right] dy \right.$$
$$\left. + \int_0^{\xi} e^{(\xi - y)\eta_2}\left[(f_u(y) - \lambda)u(y) + f_v(y)v(y)\right] dy \right],$$

where integrals are written so that solutions decay. Combining the homogeneous and particular solutions gives the operator $\mathcal{T}_{\alpha,\lambda} = \mathcal{T}_{\alpha,\lambda}[C, u, v]$ which depends on (α, λ)

and is linear in u, v and the constants $C = (c_1, c_2)$.

$$\begin{aligned}\mathcal{T}_{\alpha,\lambda}[C,u,v](\xi) =& c_1 e^{\eta_1(\xi-2\pi)} + c_2 e^{\eta_2\xi} + \frac{1}{\kappa^2(\eta_2-\eta_1)}\Bigg[-\int_{2\pi}^{\xi} e^{\eta_1(\xi-y)}\left[(f_u(y)-\lambda)u(y) + f_v(y)v(y)\right]dy \\ &+ \int_0^{\xi} e^{(\xi-y)\eta_2}\left[(f_u(y)-\lambda)u(y) + f_v(y)v(y)\right]dy\Bigg].\end{aligned}$$

We will show that

$$\begin{aligned}\mathcal{T}_{\alpha,\lambda} : \mathbb{C}^2 \times X^0 \times X^0 &\to X^0 \\ [C,u,v] &\mapsto \mathcal{T}_{\alpha,\lambda}[C,u,v]\end{aligned}$$

is a uniform contraction and the desired solution u is the unique fixed point. First, $\mathcal{T}_{\alpha,\lambda}$ applied to $u, v \in X^0$ is continuous in ξ from the variation of constants formulation. Therefore $\mathcal{T}_{\alpha,\lambda}[C,u,v](\xi) \in X^0$.

Now, select $u_1, u_2, v \in X^0$.

$$\begin{aligned}&\left|\mathcal{T}_{\alpha,\lambda}[C,u_1,v](\xi) - \mathcal{T}_{\alpha,\lambda}[C,u_2,v](\xi)\right| \\ &\quad\leq \frac{1}{\kappa^2(\eta_2-\eta_1)}\Bigg|\int_{2\pi}^{\xi} e^{\eta_1(\xi-y)}(f_u(y)-\lambda)(u_1(y)-u_2(y))dy \\ &\qquad + \int_0^{\xi} e^{(\xi-y)\eta_2}(f_u(y)-\lambda)(u_1(y)-u_2(y))dy\Bigg| \\ &\quad\leq \left(\frac{\sqrt{\alpha}}{2\sqrt{\omega\kappa}}\right)\left[\int_{2\pi}^{\xi} e^{\mathrm{Re}(\eta_1)(\xi-y)}dy + \int_0^{\xi} e^{\mathrm{Re}(\eta_2)(\xi-y)}dy\right]\left[||f_u|| + |\lambda|\right]\left|\left|u_1-u_2\right|\right| \\ &\quad\leq \left(\frac{\sqrt{\alpha}}{2\sqrt{\omega\kappa}}\right)\left(\frac{\sqrt{\alpha}}{\sqrt{\omega\kappa}}\right)\left[||f_u|| + |\lambda|\right]\left|\left|u_1-u_2\right|\right| \\ &\quad\leq \frac{1}{2}\left|\left|u_1-u_2\right|\right|.\end{aligned}$$

Therefore, $\mathcal{T}_{\alpha,\lambda}[C,u,v]$ is a uniform contraction on X^0. By the uniform contraction mapping theorem for each given v there exists a unique fixed point u given by the

solution operator $u(\xi) = \tilde{\mathcal{S}}_{\alpha,\lambda}[C,v](\xi)$. The solution operator is linear in C and v and is given by

$$\tilde{\mathcal{S}}_{\alpha,\lambda}[C,v](\xi) = c_1 e^{\eta_1(\xi-2\pi)} + c_2 e^{\eta_2\xi} + \frac{1}{\kappa^2(\eta_2-\eta_1)}\Bigg[- \int_{2\pi}^{\xi} e^{\eta_1(\xi-y)} \Big[(f_u(y)-\lambda)\tilde{\mathcal{S}}_{\alpha,\lambda}[C,v](y) + f_v(y)v(y)$$
$$+ \int_0^{\xi} e^{(\xi-y)\eta_2} \Big[(f_u(y)-\lambda)\tilde{\mathcal{S}}_{\alpha,\lambda}[C,v](y) + f_v(y)v(y)\Big]\, dy\Bigg],$$

where $\tilde{\mathcal{S}}_{\alpha,\lambda} : \mathbb{C}^2 \times X^0 \to X^2$ since for fixed α, λ, and C, $\tilde{\mathcal{S}}_{\alpha,\lambda}$, $\frac{d}{d\xi}\tilde{\mathcal{S}}_{\alpha,\lambda}$, and $\frac{d^2}{d\xi^2}\tilde{\mathcal{S}}_{\alpha,\lambda}$ are all bounded. Now, we directly solve for the unknown constants c_1 and c_2 by restricting u to be a 2π-periodic function. From $\tilde{\mathcal{S}}_{\alpha,\lambda}[C,v](0) = \tilde{\mathcal{S}}_{\alpha,\lambda}[C,v](2\pi)$, we have

$$\left(e^{-2\pi\eta_1} - 1\right) c_1 + \left(1 - e^{2\pi\eta_2}\right) c_2 = \frac{1}{\kappa^2(\eta_2-\eta_1)}\left[J_2 - J_1\right]$$

$$J_1 = \int_0^{2\pi} e^{-\eta_1 y}\left[(f_u(y)-\lambda)\,\tilde{\mathcal{S}}[C,v](y) + f_v(y)v(y)\right] dy$$
$$J_2 = \int_0^{2\pi} e^{(2\pi-y)\eta_2}\left[(f_u(y)-\lambda)\,\tilde{\mathcal{S}}[C,v](y) + f_v(y)v(y)\right] dy.$$

Similarly, $\frac{d}{d\xi}\tilde{\mathcal{S}}_{\alpha,\lambda}[C,v](0) = \frac{d}{d\xi}\tilde{\mathcal{S}}_{\alpha,\lambda}[C,v](2\pi)$ gives

$$\eta_1 c_1\left(e^{-2\pi\eta_1} - 1\right) + \eta_2 c_2\left(1 - e^{2\pi\eta_2}\right) = \frac{1}{\kappa^2(\eta_2-\eta_1)}\left[\eta_1 J_1 + \eta_2 J_2\right]$$

Combining the conditions yields expressions for c_1, c_2

$$c_1 = \left(\frac{1}{e^{-2\pi\eta_1} - 1}\right)\left(\frac{1}{\kappa^2(\eta_2-\eta_1)}\right) J_1$$
$$c_2 = \left(\frac{1}{1 - e^{2\pi\eta_2}}\right)\left(\frac{1}{\kappa^2(\eta_2-\eta_1)}\right) J_2.$$

which enforce periodic boundary conditions. Using these expressions for c_1 and c_2,

we define a final solution operator $\mathcal{S}_{\alpha,\lambda}[v](\xi)$ by

$$\begin{aligned}\mathcal{S}_{\alpha,\lambda}[v](\xi) = &\left(\frac{1}{e^{-2\pi\eta_1}-1}\right)\left(\frac{1}{\kappa^2(\eta_2-\eta_1)}\right)J_1 e^{\eta_1(\xi-2\pi)} + \left(\frac{1}{1-e^{2\pi\eta_2}}\right)\left(\frac{1}{\kappa^2(\eta_2-\eta_1)}\right)J_2 e^{\eta_2\xi} \\ &+ \frac{1}{\kappa^2(\eta_2-\eta_1)}\Bigg[-\int_{2\pi}^{\xi} e^{\eta_1(\xi-y)}\left[(f_u(y)-\lambda)\mathcal{S}_{\alpha,\lambda}[v](y)+f_v(y)v(y)\right]dy \\ &+ \int_0^{\xi} e^{(\xi-y)\eta_2}\left[(f_u(y)-\lambda)\mathcal{S}_{\alpha,\lambda}[v](y)+f_v(y)v(y)\right]dy\Bigg]\end{aligned}$$

where

$$\begin{aligned}\mathcal{S}_{\alpha,\lambda} : X^0 &\to X^2_{per} \\ v &\mapsto u = \mathcal{S}_{\alpha,\lambda}[v]\end{aligned}$$

and u is the desired eigenfunction. Continuity follows from that of $\tilde{\mathcal{S}}_{\alpha,\lambda}$ and selection of constants c_1 and c_2 gives periodicity. Bounds on the solution operator, and hence u are

$$\begin{aligned}\left|\left|\mathcal{S}_{\alpha,\lambda}[v]\right|\right| \leq& |C| + \left(\frac{\sqrt{\alpha}}{2\sqrt{\omega\kappa}}\right)\left(\frac{\sqrt{\alpha}}{\sqrt{\omega\kappa}}\right)\left[(||f_u|| + |\lambda|)\left|\left|\mathcal{S}_{\alpha,\lambda}[v]\right|\right| + ||f_v||\ ||v||\right] \\ \leq& |C| + \left(\frac{\alpha}{2\omega\kappa}\right)(||f_u|| + |\lambda|)\left|\left|\mathcal{S}_{\alpha,\lambda}[v]\right|\right| + \left(\frac{\alpha}{2\omega\kappa}\right)||f_v||\ ||v|| \\ \leq& \alpha K||v|| + \frac{1}{2}\left|\left|\mathcal{S}_{\alpha,\lambda}[v]\right|\right| + \left(\frac{\alpha}{2\omega\kappa}\right)||f_v||\ ||v|| \\ \implies \frac{1}{2}\left|\left|\mathcal{S}_{\alpha,\lambda}[v]\right|\right| \leq& \alpha K||v|| + \left(\frac{\alpha}{2\omega\kappa}\right)||f_v||\ ||v|| \\ \implies \left|\left|\mathcal{S}_{\alpha,\lambda}[v]\right|\right| \leq& \ 2\alpha K||v|| + \left(\frac{\alpha}{\omega\kappa}\right)||f_v||||v|| \\ \leq& \alpha K||v||.\end{aligned}$$

where $|C| = |c_1| + |c_2| \leq \sqrt{\alpha}K\left[|J_1| + |J_2|\right] \leq \alpha K||v||$. Thus, we obtain the desired result that for a given $v \in X^0$ there exists a unique 2π-periodic eigenfunction $u \in X^2_{per}$. Moreover, the norm of u is bounded by the given function v.

Finally, we show the bounds for the $\frac{d}{d\lambda}\mathcal{S}_{\alpha,\lambda}$

$$\begin{aligned}
\frac{d}{d\lambda}\mathcal{S}_{\alpha,\lambda}[v] &= \frac{1}{\kappa^2(\eta_2-\eta_1)}\left[\int_{2\pi}^{0} e^{\eta_1(\xi-y)}\mathcal{S}_{\alpha,\lambda}[v](y)dy - \int_0^{\xi} e^{\eta_2(\xi-y)}\mathcal{S}_{\alpha,\lambda}[v](y)dy\right] \\
\implies \left|\frac{d}{d\lambda}\mathcal{S}_{\alpha,\lambda}[v]\right| &\leq \frac{K\sqrt{\alpha}}{\sqrt{\kappa\omega}}||\mathcal{S}_{\alpha,\lambda}|| \\
&\leq K\alpha^{3/2}||v||.
\end{aligned}$$

□

Theorem 2 *Under the conditions of Hypothesis (1) and with* $u(\xi) = \mathcal{S}_{\alpha,\lambda}[v] \in X^2_{per}$ *as defined by the solution operator in Theorem 2, for* $\delta = 0$*;*

1. *If* $\lambda = \lambda_*(\alpha)$*, then there exists a unique function* $v \in X^1_{per}$ *which is a solution to (4.6) which is defined by the solution operator* $v(\xi) = \mathcal{S}^{v,0}_{\alpha,\lambda_*(\alpha)}[v_0](\xi)$ *and is linear in the initial condition* $v_0 = v(0)$*.*
2. $||v|| \leq K|v_0|$ *where* $K < \infty$ *is a constant independent of* α*,*

Proof. Under the α-scaling, the v-eigenfunction is a solution to (4.9). For $\delta = 0$, equation (4.9) reduces to the linear first order equation

$$v' + \left(\frac{\bar{g}-\lambda}{\omega}\right)v = -\frac{g_u}{\omega}u \tag{4.10}$$

where $' = \frac{d}{d\xi}$. Fix $\lambda \in \mathbb{C}$ such that $|\lambda| < M < \infty$, and $\alpha < \omega/(2||g_u||K) = \bar{\alpha}$ where K is the real constant independent of α in the bounds of u from Theorem 2. Note that this choice of α is in agreement with the α chosen in Theorem 2 since the constant K comes directly from the choice of α and $\omega/||g_u|| \sim \mathcal{O}(1)$.

For each (α, λ) pair, the integrating factors method gives the operator

$$\mathcal{T}^0_{\alpha,\lambda}[v, v_0](\xi) = e^{-\left(\frac{\bar{g}-\lambda}{\omega}\right)\xi} v_0 - \frac{1}{\omega}\int_0^\xi e^{\left(\frac{\bar{g}-\lambda}{\omega}\right)(y-\xi)} g_u(y)\mathcal{S}_{\alpha,\lambda}[v](y)dy \tag{4.11}$$

where $\mathcal{S}_{\alpha,\lambda}[v]$ is the solution operator for u defined in Theorem 2. The operator $\mathcal{T}^0_{\alpha,\lambda}$ is linear in v and the initial condition $v(0) = v_0$. Note that $\mathcal{T}^0_{\alpha,\lambda}[v, v_0](\xi)$ is continuous in ξ from integrating factors and therefore, $\mathcal{T}^0_{\alpha,\lambda} : X^0 \times \mathbb{C} \to X^0$.

Next, we show that $\mathcal{T}^0_{\alpha,\lambda}$ is a contraction on the space X^0 and the desired eigenfunction v will be the unique fixed point. For $v_1, v_2 \in X^0$,

$$\begin{aligned}
\left|\mathcal{T}_{\alpha,\lambda}[v_1, v_0](\xi) - \mathcal{T}_{\alpha,\lambda}[v_2, v_0](\xi)\right| \leq & \frac{1}{\omega}\int_0^\xi \left| e^{\left(\frac{g_v-\lambda}{\omega}\right)(y-\xi)} g_u(y)\left(\mathcal{S}_{\alpha,\lambda}[v_1](y) - \mathcal{S}_{\alpha,\lambda}[v_2](y)\right)\right| dy \\
\leq & \frac{||g_u||_\infty}{\omega}\left|\left|\mathcal{S}_{\alpha,\lambda}[v_1] - \mathcal{S}_{\alpha,\lambda}[v_2]\right|\right| \\
\leq & \alpha K \frac{||g_u||_\infty}{\omega}\left|\left|\,||v_1|| - ||v_2||\,\right|\right| \\
\leq & \alpha K \frac{||g_u||_\infty}{\omega}\left|\left|v_1 - v_2\right|\right| \\
\leq & \frac{1}{2}\left|\left|v_1 - v_2\right|\right|
\end{aligned}$$

where the bounds for the solution operator $\left|\left|\mathcal{S}_{\alpha,\lambda}[v]\right|\right| \leq \alpha K||v||$ and α are used. Thus, $\mathcal{T}^0_{\alpha,\lambda}$ is a uniform contraction on the space X^0 and there exists a unique fixed point which we define by the solution operator $v(\xi) = \tilde{\mathcal{S}}^{v,0}_{\alpha,\lambda}[v_0](\xi)$

$$\tilde{\mathcal{S}}^{v,0}_{\alpha,\lambda}[v_0](\xi) = e^{-\left(\frac{\bar{g}-\lambda}{\omega}\right)\xi} v_0 - \frac{1}{\omega}\int_0^\xi e^{\left(\frac{\bar{g}-\lambda}{\omega}\right)(y-\xi)} g_u(y)\left(\mathcal{S}_{\alpha,\lambda}\left[\tilde{\mathcal{S}}^{v,0}_{\alpha,\lambda}[v_0]\right](y)\right) dy$$

where $\tilde{\mathcal{S}}^{v,0}_{\alpha,\lambda} : X^0 \to X^1$. The fixed point is the desired eigenfunction, and is linear in

the initial condition v_0. Bounds on the operator are given by

$$\begin{aligned} &\left|\tilde{\mathcal{S}}^{v,0}_{\alpha,\lambda}[v_0](\xi)\right| \leq K|v_0| + \alpha K\left|\left|\mathcal{S}^{v,0}_{\alpha,\lambda}\right|\right| \\ \implies &||\tilde{\mathcal{S}}^{v,0}_{\alpha,\lambda}|| \leq K|v_0|. \end{aligned}$$

Furthermore, $\frac{d}{d\xi}\tilde{\mathcal{S}}^{v,0}_{\alpha,\lambda}$ is bounded and $\tilde{\mathcal{S}}^{v,0}_{\alpha,\lambda} \in X^1$. Thus, we have the existence of the eigenfunction $v \in X^1$ and is bounded by the initial condition. Using bounds in Theorem 2 yields $||u|| \leq \alpha K|v_0|$.

Finally, we use periodic boundary conditions to restrict to $v \in X^1_{per}$ which leads to requirements on λ and $\lambda = \lambda_*(\alpha)$. Define the operator $H(\alpha,\lambda)[v] = v(2\pi) - v(0)$ by

$$H(\alpha,\lambda) = \left(e^{-\left(\frac{\bar{g}-\lambda}{\omega}\right)2\pi} - 1\right) v_0 + \frac{1}{\omega}\int_0^{2\pi} e^{\left(\frac{\bar{g}-\lambda}{\omega}\right)(y-2\pi)} g_u(y)\mathcal{S}_{\alpha,\lambda}[v](y)dy \tag{4.12}$$

where $H : [0,\bar{\alpha}] \times \mathbb{C} \times X^1 \to \mathbb{C}$. Note that $H(0, g_v + in\omega)[v] = 0$ for $n \in \mathbb{Z}$ since $\mathcal{S}_{0,\lambda}[v] = 0$ from Theorem 2. Let $(\alpha_*, \lambda_*) = (0, g_v + in\omega)$. We have

$$D_\lambda H(\alpha_*,\lambda_*) = \frac{2\pi}{\omega} + \frac{1}{\omega}\int_0^{2\pi} e^{in(y-2\pi)} g_u(y)\frac{d}{d\lambda}\mathcal{S}_{\alpha_*,\lambda_*}[v](y)dy.$$

Additional, Theorem 2 gives $\frac{d}{d\lambda}\mathcal{S}_{\alpha_*,\lambda_*}[v] = 0$, therefore

$$D_\lambda H(\alpha_*,\lambda_*) = \frac{2\pi}{\omega} > 0$$

and by an application of the implicit function theorem, there exists a function $\lambda = \lambda_*(\alpha)$ such that $H(\alpha,\lambda_*(\alpha)) = 0$ near (α_*,λ_*). With this choice of $\lambda = \lambda_*(\alpha)$, we

have $v \in X^1_{per}$ given by

$$\begin{aligned} v(\xi) &= \mathcal{S}^{v,0}_{\alpha,\lambda_*(\alpha)}[v_0](\xi) \\ &= e^{-\left(\frac{\bar{g}-\lambda_*(\alpha)}{\omega}\right)\xi} v_0 - \frac{1}{\omega}\int_0^\xi e^{\left(\frac{\bar{g}-\lambda_*(\alpha)}{\omega}\right)(y-\xi)} g_u(y)\left(\mathcal{S}_{\alpha,\lambda_*(\alpha)}\left[\mathcal{S}^{v,0}_{\alpha,\lambda_*(\alpha)}[v_0]\right](y)\right) dy \end{aligned}$$

□

Theorem 3 *Assume the conditions of Hypothesis (1) and that $u(\xi) = \mathcal{S}_{\alpha,\lambda}[v] \in X^2_{per}$ as defined by the solution operator in Theorem 2. Then, for $\delta > 0$, if $\lambda = \lambda_*(\alpha)$, then there exists a unique function $v \in X^2_{per}$ which is a solution to (4.6). The v-eigenfunction is defined by the solution operator $v(\xi) = \mathcal{S}^{v,\delta}_{\alpha,\lambda}(\xi)$.*

Proof. Consider equation (4.9) with fixed $0 < \delta \ll 1$ and define $\delta = \alpha^2\beta^2$. Gathering terms in order of derivative yields

$$0 = \alpha^2\beta^2\kappa^2 v'' + \left(2i\alpha\beta^2\kappa + \omega\right) v' + \left(\bar{g} - \beta^2 - \lambda\right) v + g_u u \tag{4.13}$$

for $' = \frac{d}{d\xi}$. Fix $\lambda \in \mathbb{C}$ such that $|\lambda| < M < \infty$ and $0 < \alpha < 1/(2K||g_u||)$ where K is the constant from the bounds of u in Theorem 2. The solution to the homogeneous equation is given by $v_h(\xi) = c_1 e^{\eta_1\xi} + c_2 e^{\eta_2\xi}$ where $\eta_{1,2}$ are roots of the characteristic equation

$$0 = \alpha^2\beta^2\kappa^2\eta^2 + \left(2i\alpha\beta^2\kappa + \omega\right)\eta + \left(\bar{g} - \beta^2 - \lambda\right). \tag{4.14}$$

To leading order in α and β, the roots are

$$\eta_1 = \frac{-\bar{g} + \lambda + \beta^2}{\omega}, \quad \eta_2 = \frac{-\omega + \mathcal{O}(\alpha^2\beta^2)}{\kappa^2\alpha^2\beta^2}. \tag{4.15}$$

From the variation of constants method, a particular solution is given by

$$v_p(\xi) = \frac{1}{\kappa^2\alpha^2\beta^2(\eta_2-\eta_2)}\left[-\int_0^\xi e^{\eta_1(\xi-y)}g_u(y)u(y)dy + \int_0^\xi e^{\eta_2(\xi-y)}g_u(y)u(y)dy\right]. \tag{4.16}$$

Using the solution operator for $u(\xi) = \mathcal{S}_{\alpha,\lambda}[v](\xi)$ from Theorem 2, the eigenfunction v is a fixed point of the operator $\mathcal{T}^\delta_{\alpha,\lambda}[v, C]$ defined by

$$\begin{aligned}\mathcal{T}^\delta_{\alpha,\lambda}[v,C](\xi) =& c_1e^{\eta_1\xi} + c_2e^{\eta_2\xi} + \frac{1}{\kappa^2\alpha^2\beta^2(\eta_2-\eta_2)}\left[-\int_0^\xi e^{\eta_1(\xi-y)}g_u(y)\mathcal{S}_{\alpha,\lambda}[v](y)dy\right. \\ &\left. + \int_0^\xi e^{\eta_2(\xi-y)}g_u(y)\mathcal{S}_{\alpha,\lambda}[v](y)dy\right],\end{aligned} \tag{4.17}$$

where $\mathcal{T}^\delta_{\alpha,\lambda} : X^0 \to X^0$ and is linear in v and coefficients $C = (c_1, c_2)$. Furthermore, $\mathcal{T}^\delta_{\alpha,\lambda}$ is a uniform contraction on X^0 as for $v_1, v_2 \in X^0$,

$$\begin{aligned}&\left|\mathcal{T}^\delta_{\alpha,\lambda}[v_1,c](\xi) - \mathcal{T}^\delta_{\alpha,\lambda}[v_2,c](\xi)\right| \\ &\leq \frac{1}{\kappa^2\alpha^2\beta^2(\eta_2-\eta_2)}\left[\int_0^\xi \left|e^{\eta_1(\xi-y)}g_u(y)\left(\mathcal{S}_{\alpha,\lambda}[v_1](y) - \mathcal{S}_{\alpha,\lambda}[v_2](y)\right)\right|dy\right. \\ &\quad \left. + \int_0^\xi \left|e^{\eta_2(\xi-y)}g_u(y)\left(\mathcal{S}_{\alpha,\lambda}[v_1](y) - \mathcal{S}_{\alpha,\lambda}[v_2](y)\right)\right|dy\right] \\ &\leq \left(\int_0^\xi e^{\mathrm{Re}(\eta_1)(\xi-y)}dy + \int_0^\xi e^{\mathrm{Re}(\eta_2)(\xi-y)}dy\right)||g_u||\ \left|\left|\mathcal{S}_{\alpha,\lambda}[v_1] - \mathcal{S}_{\alpha,\lambda}[v_2]\right|\right| \\ &\leq \alpha K||g_u||\ \left|\left|\ ||v_1|| - ||v_2||\ \right|\right| \\ &\leq \frac{1}{2}\left|\left|v_1 - v_2\right|\right|\end{aligned}$$

since $|\eta_2 - \eta_1|^{-1} \leq \kappa^2\alpha^2\beta^2$. Therefore, there exists a solution operator $\tilde{\mathcal{S}}^{v,\delta}_{\alpha,\lambda}[C]$ which

is linear in C and defines the general solution for $v \in X^2$

$$\begin{aligned}\tilde{\mathcal{S}}^{v,\delta}_{\alpha,\lambda}[C](\xi) =& c_1 e^{\eta_1 \xi} + c_2 e^{\eta_2 \xi} + \frac{1}{\kappa^2 \alpha^2 \beta^2 (\eta_2 - \eta_2)} \Bigg[- \int_0^\xi e^{\eta_1 (\xi - y)} g_u(y) \mathcal{S}_{\alpha,\lambda} \left[\tilde{\mathcal{S}}^{v,\delta}_{\alpha,\lambda}[C] \right](y) dy \\ &+ \int_0^\xi e^{\eta_2 (\xi - y)} g_u(y) \mathcal{S}_{\alpha,\lambda} \left[\tilde{\mathcal{S}}^{v,\delta}_{\alpha,\lambda}[C] \right](y) dy \Bigg],\end{aligned}$$

where

$$\begin{aligned}\tilde{\mathcal{S}}^{v,\delta}_{\alpha,\lambda} : \mathbb{C}^2 &\to X^2 \\ C &\mapsto v = \tilde{\mathcal{S}}^{v,\delta}_{\alpha,\lambda}[C]\end{aligned}$$

and $\tilde{\mathcal{S}}^{v,\delta}_{\alpha,\lambda}$, $\frac{d}{d\xi}\tilde{\mathcal{S}}^{v,\delta}_{\alpha,\lambda}$, and $\frac{d^2}{d\xi^2}\tilde{\mathcal{S}}^{v,\delta}_{\alpha,\lambda}$ are all bounded for fixed $\alpha,\ \lambda$, and C. Last, we restrict our space to the 2π-periodic functions in X^2_{per} and obtain constraints on λ. Periodic boundary conditions on $\tilde{\mathcal{S}}^{v,\delta}_{\alpha,\lambda}$ and $\frac{d}{d\xi}\tilde{\mathcal{S}}^{v,\delta}_{\alpha,\lambda}$ give the system of equations

$$\begin{aligned}&\tilde{\mathcal{S}}^{v,\delta}_{\alpha,\lambda}[C](0) - \tilde{\mathcal{S}}^{v,\delta}_{\alpha,\lambda}[C](2\pi) = 0 \\ &\frac{d}{d\xi}\tilde{\mathcal{S}}^{v,\delta}_{\alpha,\lambda}[C](0) - \frac{d}{d\xi}\tilde{\mathcal{S}}^{v,\delta}_{\alpha,\lambda}[C](2\pi) = 0.\end{aligned} \tag{4.18}$$

Since $\mathcal{S}_{\alpha,\lambda}[v]$ is linear in v and $\tilde{\mathcal{S}}^{v,\delta}_{\alpha,\lambda}[C]$ is linear in C, write

$$\begin{aligned}\mathcal{S}_{\alpha,\lambda}\left[\tilde{\mathcal{S}}^{v,\delta}_{\alpha,\lambda}[C]\right](\xi) &= \alpha K \tilde{\mathcal{S}}^{v,\delta}_{\alpha,\lambda}[C](\xi) \\ &= \alpha K \left(c_1 \tilde{\mathcal{S}}^{v,\delta}_{1,\alpha,\lambda}(\xi) + c_2 \tilde{\mathcal{S}}^{v,\delta}_{2,\alpha,\lambda}(\xi) \right)\end{aligned}$$

where $||\tilde{\mathcal{S}}^{v,\delta}_{1,\alpha,\lambda}||, ||\tilde{\mathcal{S}}^{v,\delta}_{2,\alpha,\lambda}|| \leq K$. Using this notating, integrals in the system (4.18) can be split and terms grouped by c_1 and c_2. Thus, finding c_1, c_2 is reduced to solving

the system

$$AC = \begin{pmatrix} (1-e^{2\pi\eta_2}) - \alpha K B J_1 & (1-e^{2\pi\eta_2}) + \alpha K B J_2 \\ \eta_1\left((1-e^{2\pi\eta_1}) - \alpha K B J_1\right) & \eta_2\left((1-e^{2\pi\eta_2}) + \alpha K B J_2\right) \end{pmatrix} \begin{pmatrix} c_1 \\ c_2 \end{pmatrix} = 0$$

where $B = 1/\alpha^2\beta^2(\eta_2 - \eta_1)$, $J_1 = \int_0^{2\pi} \left(e^{\eta_1(2\pi - y)} - e^{\eta_2(2\pi - y)}\right) g_u(y) \tilde{\mathcal{S}}^{v,\delta}_{1,\alpha,\lambda}(y) dy$, and $J_2 = \int_0^{2\pi} \left(e^{\eta_1(2\pi - y)} - e^{\eta_2(2\pi - y)}\right) g_u(y) \tilde{\mathcal{S}}^{v,\delta}_{2,\alpha,\lambda}(y) dy$. Note that $|J_1|,\ |J_2| \leq K$ since all terms are bounded and the integral is over a finite domain. This system has non-trivial solutions precisely when $\det(A) = 0$. Define $\mathcal{H}(\alpha, \beta, \lambda) = \det(A)$. Then,

$$\mathcal{H}(\alpha, \beta, \lambda) = \det(A) = (\eta_2 - \eta_1)\left((1-e^{2\pi\eta_1}) - \alpha K B J_1\right)\left((1-e^{2\pi\eta_2}) + \alpha K B J_2\right).$$

Since $\eta_2 - \eta_1 \neq 0$, we must have $(1-e^{2\pi\eta_1}) - \alpha K B J_1 = 0$ or $(1-e^{2\pi\eta_2}) + \alpha K B J_2 = 0$. These requirements indicate that either η_1 or η_2 must be $\mathcal{O}(\alpha)$-close to an imaginary integer. Note that it cannot be η_2 since $\mathrm{Re}(\eta_2) \sim (\alpha^2\beta^2)^{-1} \to -\infty$ as $\alpha \to 0$ for fixed δ. Therefore,

$$\begin{aligned} \eta_1 &= in + \mathcal{O}(\alpha), \quad n \in \mathbb{N} \\ \frac{-\bar{g} + \lambda + \beta^2}{\omega} &= in + \mathcal{O}(\alpha) \\ \implies \lambda &= \bar{g} + i\omega n - \beta^2 + \mathcal{O}(\alpha). \end{aligned}$$

Thus, the system has a non-trivial solution for C if $\lambda = \bar{g} + i\omega n - \beta + \mathcal{O}(\alpha)$.

Furthermore, $\mathcal{H}(\alpha_*, \beta_*, \lambda_*) = 0$ for $(\alpha_*, \beta_*, \lambda_*) = \left(\alpha_*, \sqrt{\delta}/\alpha_*, \bar{g} + i\omega n - \beta + \mathcal{O}(\alpha_*)\right)$,

and

$$D_\lambda \mathcal{H}(\alpha_*, \beta_*, \lambda_*) = -\frac{1}{\omega}\left(1 - e^{2\pi(in+\mathcal{O}(\alpha))} - \alpha K B J_1\right)\left(1 - e^{2\pi\eta_2} + \alpha K B J_2\right) \tag{4.19}$$

$$+ (\eta_2 - (in + \mathcal{O}(\alpha)))\left(-\frac{2\pi}{\omega} e^{2\pi(in+\mathcal{O}(\alpha))}\right)\left(1 - e^{2\pi\eta_2} + \alpha K B J_2\right). \tag{4.20}$$

The first term in (4.19) is $\mathcal{O}(\alpha)$ whereas the second term is bounded away from zero, yielding $\left|D_\lambda \mathcal{H}(\alpha_*, \beta_*, \lambda_*)\right| > 0$. By the implicit function theorem, we can write $\lambda = \lambda_*(\alpha, \beta)$ for (α, β) near (α_*, β_*). Using this choice of $\lambda = \lambda_*(\alpha, \beta)$ allows us to solve explicitly for C giving the desired eigenfunction $v \in X^2_{per}$ which is defined by the operator

$$\mathcal{S}^{v,\delta}_{\alpha,\lambda_*(\alpha,\beta)}(\xi) = c_1 e^{\eta_1 \xi} + c_2 e^{\eta_2 \xi} + \frac{1}{\kappa^2 \alpha^2 \beta^2 (\eta_2 - \eta_2)}\left[- \int_0^\xi e^{\eta_1(\xi - y)} g_u(y) \mathcal{S}_{\alpha,\lambda}\left[\mathcal{S}^{v,\delta}_{\alpha,\lambda_*(\alpha,\beta)}\right](y) dy \right.$$

$$\left. + \int_0^\xi e^{\eta_2(\xi - y)} g_u(y) \mathcal{S}_{\alpha,\lambda}\left[\mathcal{S}^{v,\delta}_{\alpha,\lambda_*(\alpha,\beta)}\right](y) dy \right].$$

□

Corollary 1 *Under the conditions of Hypothesis (1) and with $\delta = \alpha^2\beta^2$, the essential spectrum curve $\lambda(\alpha, \beta)$ and eigenfunctions $u(\xi; \alpha, \lambda)$, $v(\xi; \alpha, \lambda)$ have the following expansions in parameters α and β.*

$$\begin{aligned}
u(\xi; \alpha, \beta) &= \alpha^2 f_v(\xi) e^{in\xi} + \alpha^2 \beta f_v(\xi) e^{in\xi} + \alpha^2 \beta^2 f_v(\xi) e^{in\xi} + \mathcal{O}(\alpha^3, \beta^3) \\
v(\xi; \alpha, \beta) &= e^{in\xi} + \alpha e^{in\xi} + \beta e^{in\xi} + \alpha\beta e^{in\xi} + \alpha^2 v_{20}(\xi) + \beta^2 e^{in\xi} + \mathcal{O}(\alpha^3, \beta^3) \\
\lambda(\alpha, \beta) &= \bar{g} + i\omega n + \alpha^2 \frac{1}{2\pi} \int_0^{2\pi} g_u(s) f_v(s) ds - \beta^2 + \alpha^3 \lambda_{30} + \mathcal{O}(\beta^3),
\end{aligned}$$

where

$$\lambda_{30} = \frac{\kappa n}{\pi}\int_0^{2\pi} g_u(s)f_v(s)ds - \frac{i\kappa}{\pi}\int_0^{2\pi} g_u(s)f_v'(s)ds.$$

Moreover, for $\delta > 0$ $Re(\lambda) \to -\infty$, and in the case $\delta = 0$, the essential spectrum will limit to the finite point

$$\lambda_0 = \bar{g} + i\omega n.$$

Proof. From Theorems 2 - 4, the curves of essential spectrum and eigenfunctions can be written as expansions of α and β of the form

$$\begin{aligned}
u(\xi;\alpha,\beta) =& u_0(\xi) + \alpha u_{10}(\xi) + \beta u_{01}(\xi) + \alpha\beta u_{11}(\xi) + \alpha^2 u_{20}(\xi) + \beta^2 u_{02}(\xi) + \alpha^3 u_{30}(\xi) + \beta^3 u_{03}(\xi) \\
&+ \mathcal{O}(\alpha^2\beta, \alpha\beta^2) \\
v(\xi;\alpha,\beta) =& v_0(\xi) + \alpha v_{10}(\xi) + \beta v_{01}(\xi) + \alpha\beta v_{11}(\xi) + \alpha^2 v_{20}(\xi) + \beta^2 v_{02}(\xi) + \alpha^3 v_{30}(\xi) + \beta^3 v_{03}(\xi) \\
&+ \mathcal{O}(\alpha^2\beta, \alpha\beta^2) \\
\lambda(\alpha,\beta) =& \lambda_0 + \alpha\lambda_{10} + \beta\lambda_{01} + \alpha\beta\lambda_{11} + \alpha^2\lambda_{20} + \beta^2\lambda_{02} + \alpha^3\lambda_{30} + \beta^3\lambda_{03} + \mathcal{O}(\alpha^2\beta, \alpha\beta^2)
\end{aligned} \tag{4.21}$$

where the $u_{j,k}$ and $v_{j,k}$ are 2π-periodic. Note that setting $\beta = 0$ corresponds to the case $\delta = 0$. The $u_{j,k}$ and $v_{j,k}$ terms are solved for by substituting the general forms (4.21) into the $\alpha - \beta$ scaling of the essential spectrum curves, matching orders of α and β, and enforcing periodic boundary conditions. Below, we provide the results of matching orders in the u-equation, and focus on the v-equation as this is more insightful and will also determine the expansion for λ

From the u-equation, we find

$$\begin{aligned}
u_0 = u_{10} = u_{01} = u_{02} = u_{11} = u_{12} = 0 \\
u_{20}(\xi) = f_v(\xi) v_0(\xi) \\
u_{21} = f_v(\xi) v_0(\xi) \\
u_{22} = f_v(\xi) v_{01}(\xi)
\end{aligned}$$

Now, in the v-equation, we match orders and solve the resulting differential equations for the $v_{j,k}$ terms:

$\mathcal{O}(1)$:

$$\begin{aligned}
\lambda_0 v_0 &= \omega v_0' + g_v v_0 + g_u u_0 \\
v_0' = \left(\frac{\lambda_0 - \bar{g}}{\omega} \right) v_0 \implies v_0(\xi) &= e^{(\frac{\lambda_0 - \bar{g}}{\omega})\xi}
\end{aligned}$$

By periodic boundary conditions, $\lambda_0 = \bar{g} + i\omega n$, $n \in \mathbb{Z}$, and $v_0(\xi) = e^{in\xi}$.

$\mathcal{O}(\alpha)$:

$$\begin{aligned}
\lambda_{10} v_0 + \lambda_0 v_{10} + \omega v_{10}' + \bar{g} v_{10} + g_u u_{10} \\
v_{10}' = i n v_{10} + \lambda_{10} e^{in\xi} \\
\implies v_{10}(\xi) = e^{in\xi} (c + \lambda_{10} \xi)
\end{aligned}$$

Enforcing periodic boundary conditions gives, $\lambda_{10} = 0$, $v_{10}(\xi) = e^{in\xi}$.

$\mathcal{O}(\beta)$:

$$\begin{aligned}
\lambda_{01} v_0 + \lambda_0 v_{01} = \omega v_{01}' + \bar{g} v_{01} \\
v_{01}' = i n v_{01} + \lambda_{01} e^{in\xi} \\
\implies v_{01}(\xi) = e^{in\xi} (c + \lambda_{01} \xi)
\end{aligned}$$

Periodic boundary conditions gives $\lambda_{01} = 0$, $v_{01}(\xi) = e^{in\xi}$.

$\mathcal{O}(\alpha\beta)$:

$$\lambda_0 v_{11} + \lambda_{10} v_0 + \lambda_{01} v_{10} + \lambda_{11} v_0 = \omega v_{11}' + \bar{g} v_{11}$$
$$v_{11}' = inv_{11} + \frac{\lambda_{11}}{\omega} e^{in\xi}$$

Again, periodic boundary conditions gives, $v_{11}(\xi) - e^{in\xi}$, $\lambda_{11} = 0$.

Continuing to match higher and higher orders gives

$$\begin{aligned}
v_{20}(\xi) &= e^{in\xi} + e^{in\xi}\left(\frac{\lambda_{20}}{\omega}\right)\xi - \frac{e^{in\xi}}{\omega}\int_0^\xi g_u(s) f_v(s) ds \\
\lambda_{20} &= \frac{1}{2\pi}\int_0^{2\pi} g_u(s) f_v(s) ds \ \in \mathbb{R} \\
v_{02}(\xi) &= e^{in\xi} \\
\lambda_{02} &= -1 \\
\lambda_{30} &= \frac{\kappa n}{\pi}\int_0^{2\pi} g_u(s) f_v(s) ds - \frac{i\kappa}{\pi}\int_0^{2\pi} g_u(s) f_v'(s) ds.
\end{aligned}$$

Finally, fix $\delta > 0$ then $\beta = \sqrt{\delta}/\alpha > 0$ and as $\alpha \to 0$, $\beta \to -\infty$ to keep δ constant. Therefore, as long as $\delta > 0$, the limit point of the essential spectrum is found by sending $\alpha \to 0$ and $\beta \to -\infty$ in the expansion for $\lambda(\alpha, \beta)$. Due to the coefficient $\lambda_{02} = -1$, we see that

$$\lim_{\alpha \to 0} \lim_{\beta \to -\infty} \mathrm{Re}(\lambda(\alpha, \beta)) = -\infty.$$

However, in the case $\delta = 0$, all of the β terms in the $\lambda(\alpha, \beta)$ are 0, and the expansion is reduced to

$$\lambda(\alpha, 0) = \lambda_0 + \alpha^2 \lambda_{20} + \mathcal{O}(\alpha^3),$$

and we have

$$\lim_{\alpha \to 0} \lambda(\alpha, 0) = \lambda_0.$$

□

Chapter Five

Geometry-dependent transitions to arrhythmic rhythms

In this chapter, we provide results from an experimental and numerical study that highlight the role of tissue geometry in complex transitions in a model system of electrically excitable cells. This work appears in [39].

Little is known about how individual cells sense the macroscopic geometry of their tissue environment. Here we explore whether long-range electrical signaling can convey information on tissue geometry to individual cells. First, we studied an engineered electrically excitable cell line. Cells grown in patterned islands of different shapes showed remarkably diverse firing patterns under otherwise identical conditions, including regular spiking, period-doubling alternans, and arrhythmic firing. A detailed ion-channel model quantitatively reproduced these effects, showing how the macroscopic geometry affected the single-cell electrophysiology via the influence of gap junction-mediated electrical coupling. Qualitatively similar geometry dependent dynamics were observed in human induced pluripotent stem cell (iPSC)-derived cardiomyocytes. The cardiac results urge caution in translating observations of arrhythmia in vitro to predictions in vivo where the tissue geometry is very different. We study how to extrapolate electrophysiological measurements between tissues with different geometries and different gap junction couplings.

5.1 Introduction

Cells in multicellular organisms sense their location within tissues via diffusible molecules, contact interactions, and mechanical signals [72]. Gap junction-mediated electrical signals can also, in principle, provide long-range positional cues [73], though mechanistic details have been difficult to determine due to simultaneous interactions between all of the above signaling modalities. Here we use a simple genetically engi-

neered excitable tissue to ask how the electrical dynamics of a cell inside the tissue are affected by remote boundaries.

The electrophysiological properties of many types of isolated cells have been probed in detail via patch clamp electrophysiology [74]. For isolated cells or small clusters, spiking dynamics can often be described by simple autoregressive models [75–77]. In tissues, cells form electrical connections with their neighbors via gap junction channels. One can then ask whether this coupling is a minor perturbation on the individual cells, or whether it fundamentally changes the dynamics. In condensed matter physics, the properties of a bulk solid can differ dramatically from those of its constituent atoms. Similarly, the emergent electrical properties of bulk tissue might differ dramatically from those of individual cells. Indeed, recent theoretical work showed that electrical conduction could shift the transitions between stability and arrhythmia in excitable tissues [78, 79].

Much of the interest in long-range electrical coupling has focused on the heart, where transitions between regular and irregular beating can be a matter of life or death. Rearrangements of electrical gap junctions have been implicated in the onset of arrhythmia [80], and structural defects can also act as nuclei for arrhythmias [81]. In both cases, establishing the causal roles of electrical coupling is difficult due to the simultaneous occurrence of mechano-electrical feedbacks [82, 83] and changes in single-cell properties [84–87]. Furthermore, the wide diversity of cardiac models, combined with uncertainty in model parameters, presents a challenge for comparison to experiments [79, 88]. Only a few experiments have explicitly probed the roles of intercellular coupling in cardiac dynamics [89–91].

Uncertainties regarding the role of geometry in cardiac stability have an important

practical implication: it has been widely claimed that if human induced pluripotent stem cell (iPSC)-derived cardiomyocytes (hiPSC-CM) can be made to show mature patterns of ion channel expression [92–95], then in vitro cultures will be a useful substrate for studying arrhythmias [96–99]. This belief underpins a large-scale effort, called the Comprehensive in-vitro Proarrhythmia Assay (CiPA), sponsored by the U.S. Food and Drug Administration (FDA) to use hiPSC-CM as a substrate for evaluating pro-arrhythmia risks in candidate therapeutics. However, this approach would need further consideration if one finds that there are fundamental geometry-driven differences in stability between cultured cells and intact tissue, even when all voltage-dependent conductances are identical.

Here we describe isradipine-OS-HEK (iOS-HEK, where the 'i' stands for isradipine) cells as a model for studying the impacts of geometry on arrhythmia. This synthetic bioelectric system showed dynamical transitions between regimes of regular pacing, complex but repeating patterns, and irregular (non-repeating) dynamics as the pace frequency is increased. We explored in detail how these stability regimes were influenced by the macroscopic tissue geometry. Transitions to complex and irregular patterns depended sensitively on the culture geometry. At a single pacing frequency, we simultaneously observed regular rhythms, alternating patterns, irregular dynamics, or depolarization block in islands that were identical in all respects except for their geometry. A biophysically detailed Hodgkin Huxley-style model captured these geometric effects. The iOS-HEK cells further showed second-degree conduction block in regions of high wavefront curvature, demonstrating sensitivity to two-dimensional geometric features. Finally, we show that similar geometry-dependent transitions occur in cultured human iPSC-derived cardiomyocytes. Together our findings show that macroscopic tissue geometry is a fundamental determinant of bioelectrical dynamics, and not just a perturbation on the cell-autonomous behavior. We discuss

which parameters are sensitive or insensitive to tissue geometry, and propose scaling relations that can be used to extrapolate across tissue geometries and across intercellular coupling strengths.

5.2 Methods

Here, we first describe the structure of the bioengineered iOS-HEK cells and the experimental design in Section 5.2.1. The ion-channel model derivation and simulations are then described in Sections 5.2.2 and 5.2.3, respectively. Additional details about how model parameters were derived and full experimental procedures are included in the chapter appendix (Section 5.5).

5.2.1 Bioengineered iOS-HEK cells support traveling waves, alternans, and arrhythmias

To explore the role of geometry under controlled conditions, we engineered a synthetic excitable tissue where all elements were well understood. Optopatch Spiking Human Embryonic Kidney (OS-HEK) cells were previously introduced in [100] as an engineered excitable cell type with an all-optical electrophysiological interface. HEK293 cells present a clean electrophysiological background, in that their membranes pass little current between -80 and +30 mV [101], while an endogenous Na+/K+ ATPase maintains steady cardiac-like transmembrane concentration gradients for these two cations [102]. The cells were engineered to express just two voltage-dependent channels, the voltage-gated cardiac sodium channel, $Na_V1.5$, and the inward rectifier potassium channel, $K_{ir}2.1$. Expression of a channelrhodopsin, CheRiff, permitted op-

togenetic stimulation. Membrane voltage was recorded optically, via either a far-red voltage-sensitive protein (QuasAr2) [103] or dye (BeRST1) [104]. Endogenous gap junction proteins introduced nearest-neighbor electrical coupling [100]. The individual components of the OS-HEK cells have previously been characterized in detail by manual patch clamp recordings [103, 105].

When optogenetically stimulated, these OS-HEK cells produced single action potentials. When grown into a confluent syncytium, the endogenous gap junctions mediated bulk propagation of electrical waves [100]. The OS-HEK cells previously demonstrated many interesting attributes of excitable tissues, including wave conduction, curvature-dependent wavefront velocity, and re-entrant spiral waves [100], but we did not observe arrhythmias, suggesting that a necessary ingredient was missing from this model system.

Here we describe isradipine-OS-HEK (iOS-HEK) cells as a model for studying the impacts of geometry on arrhythmia. We hypothesized that our previous failure to observe arrhythmia in the OS-HEK system was due to the absence of slowly recovering conductances. In cardiomyocytes, delayed rectifier potassium channels gradually restore excitability after repolarization, so that the waveform of each beat depends on the interval since its predecessor. This beat-to-beat memory can lead to instabilities under periodic pacing. The drug isradipine causes state-dependent block in the $Na_V1.7$ and $Na_V1.5$ sodium channels, with a with a recovery time of $\sim$ 200 ms at 100 mV [105]. We reasoned that isradipine would cause a slow recovery of the $Na_V1.5$ channels in OS-HEK cells after a beat, mimicking via a different ionic mechanism the slow recovery of cardiomyocytes after repolarization. We hypothesized that this slow recovery would be sufficient to support arrhythmic dynamics.

In a confluent monolayer of OS-HEK cells, we observed regular spiking when the cells were optogenetically paced at 4 Hz (10 ms pulses, 100 mW/cm^2). Addition of isradipine (10 μM) converted the spiking to an alternating rhythm between large and small spikes (Figure 5.1c), consistent with a previous report [105]. We refer to the OS-HEK cells with 10 μM isradipine as iOS-HEK cells. This dynamical transition qualitatively resembles the so-called alternans instability in cardiac tissue, in which rapid pacing causes an alternating series of large and small excitations.

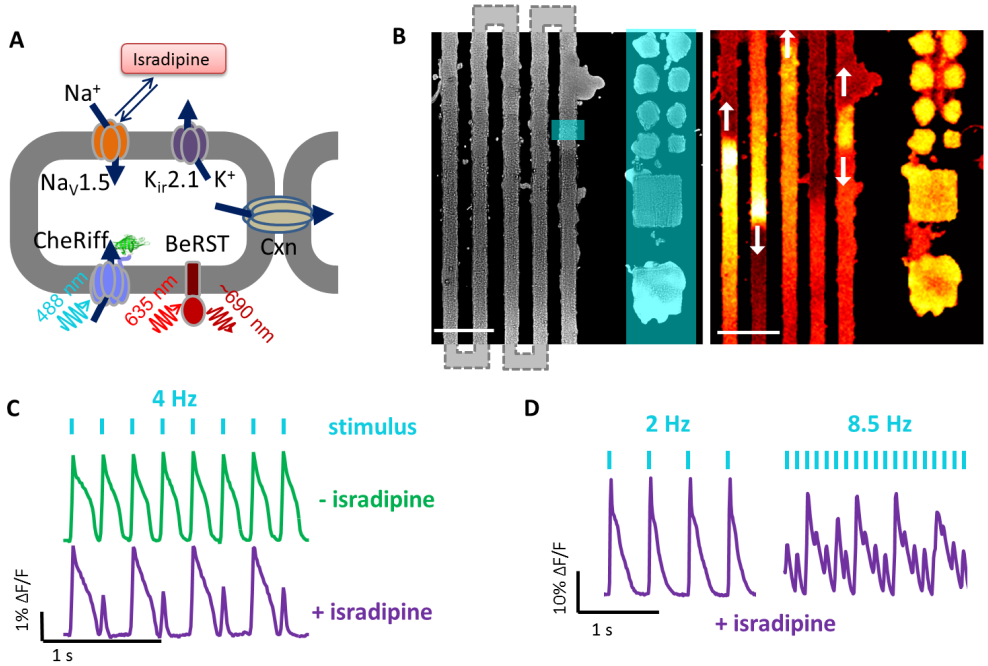

Figure 5.1: Isradipine renders Optopatch-Spiking HEK cells susceptible to arrhythmia. (a) Molecular components of the synthetic excitable tissue. The voltage-gated sodium channel NaV1.5 and inward-rectifying potassium channel Kir2.1 are together sufficient to produce action potentials in response to a depolarizing stimulus. CheRiff is a blue-shifted channelrhodopsin which depolarizes the cells in response to blue light, and BeRST1 is a dye which reports voltage through changes in red fluorescence. Connexin channels (Cxn) introduce electrical coupling between neighboring cells. (b) Left: microcontact printing defines patterns of cell growth. The vertical stripes connect in a serpentine pattern outside the field of view. Blue overlay shows regions of optogenetic stimulation. Zero-dimensional "islands" are tested alongside one-dimensional "tracks". Right: single frame from a movie of BeRST1 fluorescence showing traveling waves in the track region. Scale bars 500 μm. (c) Fluorescence recordings of membrane voltage showing that isradipine (10 μM) induces alternans in OS-HEK cells paced at 4 Hz. (d) At low pace frequency isradipine OS-HEK (iOS-HEK) cells beat periodically in synchrony with the pacing, but at high pace frequency the cells produce an irregular rhythm.

Using microcontact printing [106], we patterned features comprised square is-

lands of linear size 100 μm, 200 μm and 500 μm, as well as serpentine tracks of width 100, 200, 500 μm and edge length of 1 mm and 5 mm. Overall track lengths were as long as 7 cm.

Localized stimulation of the serpentine tracks induced propagating electrical waves. Optogenetically induced waves propagated with a typical conduction velocity of 3.3 cm/s, had an AP width at 50% repolarization of 110 ms, and thus had a depolarized action potential length λ of $\lambda = 3.6$ mm. The fluorescence in the paced region of the track showed complex beat rate-dependent dynamics. At 2 Hz pacing, the cells spiked regularly and in phase with the drive (Figure 5.1d, left). At 8.5 Hz pacing, the cells showed a complex and irregular fluorescence pattern, indicative of arrhythmia (Figure 5.1d, right).

5.2.2 Ion-channel model for iOS-HEK cells

We developed a conductance-based ion-channel model to simulate the dynamics of iOS-HEK cells. The key features of the iOS-HEK cells which contribute to the voltage are the $Na_V1.5$ sodium channel, $K_{ir}2.1$ potassium channel, optical stimulus via CheRiff, and memory effects caused by the isradipine drug. In the model, the sodium channel and isradipine effects are treated as dynamic gating variables and potassium channel and optical stimulation are functions of the voltage.

The properties of $Na_V1.5$, $K_{ir}2.1$, and channelrhodopsin CheRiff are all well known, so we were able to constrain the model with a small number of free parameters (Figure 5.4a). The sodium channel model is comprised of activation m and inactivation gates h which are dimensionless variables that take values between 0 (gate inactive)

and 1 (gate fully active). Governing equations are taken from the literature [107, 108]

$$\frac{dm}{dt} = \tau_m(V)^{-1}\left(m_\infty(V) - m\right)$$
$$\frac{dh}{dt} = \tau_h(V)^{-1}\left(h_\infty(V) - h\right).$$

Here, $\tau_m(V)$ and $\tau_j(V)$ are time constants that tell how quickly the gates approach the asymptotic values $m_\infty(V)$ and $h_\infty(V)$. These quantities are given by

$$\tau_h(V) = \frac{1}{2}\left(1 - \tanh\left(\frac{V+40}{10}\right)\right)\tau_{h1}(V) + \frac{1}{2}\left(1 + \tanh\left(\frac{V+40}{10}\right)\right)\tau_{h2}(V)$$
$$\tau_{h1}(V) = \left(0.057\exp\left(\frac{-70-80}{6.8}\right) + 2.7\exp\left(0.079V\right) + \left(3.1\times 10^5\right)\exp\left(0.3486V\right)\right)^{-1}$$
$$\tau_{h2}(V) = \frac{0.13}{0.77}\left(1 + \exp\left(\frac{-V-10.66}{11.1}\right)\right)$$
$$\tau_m(V) = 0.1\left(1+\exp\left(\frac{-60-V}{50}\right)\right)^{-1}\left[\left(1+\exp\left(\frac{V+35}{5}\right)\right)^{-1} + \left(1+\exp\left(\frac{V-50}{200}\right)\right)^{-1}\right].$$

$$h_\infty(V) = \left(1+\exp\left(\frac{V+71.55}{7.43}\right)\right)^{-2}$$
$$m_\infty(V) = \left(1+\exp\left(\frac{-56.86-V}{9.03}\right)\right)^{-2}.$$

Minor modifications were made to the h time constant τ_h, to smooth the discontinuous function [107, 108].

The drug isradipine acts by binding to and blocking activation of the sodium channels. We introduced an additional slowly activating and slowly recovering gate j to describe the dynamics of isradipine with behavior governed by

$$\frac{dj}{dt} = \alpha m\left(1-j\right) - \mu j.$$

That is, the drug binds to sodium channels in its open state with rate α and unbinds with rate μ. The equation for the isradipine dynamics can be rewritten in the form

$$\frac{dj}{dt} = \tau_j(V)^{-1}\left(j_\infty(V) - j\right)$$

where

$$\tau_j(V) = \left(\alpha m(V) + \mu\right)^{-1}, \quad j_\infty(V) = \frac{\alpha m(V)}{\alpha m(V) + \mu}.$$

Plots of the time constants and asymptotic states are shown in Figure 5.2. Since the time constant of the sodium activation gate m is orders of magnitude faster than the other gates, the gate was replaced with the asymptotic limit m_∞. This standard approximation allowed for more efficient computations without impacting the simulation results.

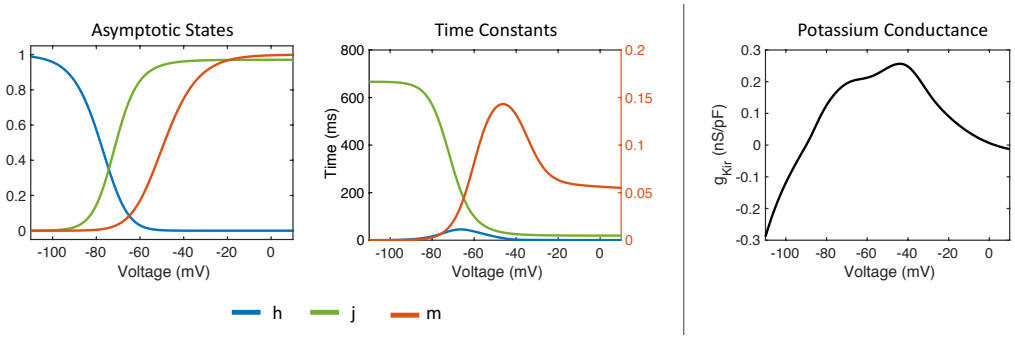

Figure 5.2: (a) Shape of asymptotic gating variables $m_\infty, h_\infty, j_\infty$. (b) Time constants associated with each channel. τ_m follows scale on right vertical axis. (c) Potassium K_{ir} conductance fit from experimental data.

The $K_{ir}2.1$ conductance was modeled as an instantaneous function of voltage, derived from a smoothing spline fit to the action potential waveform at low drive frequency $f = 2$ Hz. The spline fit is shown in Figure 5.2c. The channelrhodopsin was modeled as a linear conductance with a 0 mV reversal potential, modulated in space and time by the blue light illumination. A diffusive term captured the nearest-neighbor gap junction coupling. The voltage dynamics V are governed by

the equation

$$C_m \frac{\partial V}{\partial t} = G_{\text{Cxn}} \Delta V - (I_{\text{NaV}} + I_{\text{Kir}} + I_{\text{ChR}}) \tag{5.1}$$

where V is the voltage in mV and C_m is the membrane capacitance of a cell. The ionic currents (I_{NaV}, I_{Kir} and I_{ChR}) drive local dynamics, while the diffusion term couples neighboring regions. Units of space are 10^{-5} m (corresponding to linear size of one cell), and time is in ms. Conductances are measured in nS/pF and ionic currents in pA/pF. Ionic currents are

$$\begin{aligned} I_{\text{NaV}} &= g_{\text{NaV}} m_\infty^3(V) h \, (1 - j) \, (V - E_{\text{Na}}) \\ I_{\text{Kir}} &= g_{\text{Kir}}(V) \, (V - E_K) \\ I_{\text{ChR}} &= g_{\text{ChR}}(x, t) \, (V - E_{ChR}) \, . \end{aligned}$$

Model parameters are defined in Table 5.1. Unknown parameters (C_m, g_{Cxn}, g_{Kir}, g_{ChR}) were determined by fitting to observed fluorescence waveforms, conduction velocities, patch clamp measurements, and experimentally observed dynamical transitions. Additional details about how these values were selected are included in the chapter appendix (Section 5.5).

We set $G_{\text{Cxn}} = g_{\text{Cxn}} \times \ell^2$ where g_{Cxn} is the strength of the gap junction conductance between cells, and ℓ is the linear dimension of a cell. The electrical diffusion coefficient is given by G_{Cxn}/C_m. To simulate 0D dynamics, g_{Cxn} was set to zero. Equation (5.1) represents a continuum model, which treats the domain as homogeneous tissue. In simulations, the cell discreteness is recovered by setting the spatial discretization equal to cell length.

Capacitance	$C_m = 1$
Sodium reversal potential	$E_{Na} = 75$ mV
Potassium reversal potential	$E_K = -107$ mV
CheRiff reversal potential	$E_{ChR} = 0$mV
Sodium conductance	$g_{NaV} = 1.5$ nS/pF
CheRiff conductance	$g_{ChR} = 15$ pS/pF
Connexin conductance	$g_{Cxn} = 40$ nS/pF
Length of one cell	$\ell = 10^{-6}$ m
Isradipine binding rate	$\alpha = 0.5$ ms^{-1}
Isradipine unbinding rate	$\mu = 0.015$ ms^{-1}

Table 5.1: Values and descriptions of system parameters used in simulations of the iOS-HEK conductance model. All conductances were expressed as specific conductances per unit capacitance, allowing us to set $C_m = 1$.

5.2.3 Numerical simulations of iOS-HEK cells

Action potential waveforms were numerically simulated in a 0D geometry and in a linear 1D track comprising 2000 cells, with pacing delivered to 40 cells on one end. The near-field response was monitored in the paced zone, and the far-field response was monitored at a distance of 3 mm from the stimulus.

The 1D tracks were discretized with a spatial step size δx equal to 10 μm, the length of one OS-HEK cell. With this discretization size, each grid point represented one cell, allowing the simulations to have similar spatial resolution as the experiments. Neumann boundary conditions are used at each end of the 1D tracks.

The Laplacian was modelled with a fourth-order centered finite difference scheme. Boundary conditions were implemented using the standard ghost-point method. A combination IMEX scheme was used for the time evolution, with implicit Crank-Nicholson applied to the diffusion terms and explicit Adams-Bashforth applied to the remaining nonlinear terms (ion currents and gating dynamics). A time step of 0.1 δx ms (10^{-6} ms in the case of 10 μm spatial step) was used, which is well

within the accuracies of the numerical scheme and is significantly smaller than any time scales in the model. Single cell, 0D dynamics were modelled by setting g_{Cxn} to zero, and time evolution was performed with the same Adams-Bashforth scheme. All computations were performed using MATLAB.

5.3 Results

5.3.1 Geometry dependent instabilities observed in experiments of iOS-HEK cells

We characterized in detail the dependence of the electrical dynamics on local geometry in the experiments. Cells were grown either in small square 'islands' or on adjacent linear 'tracks', and paced simultaneously in both geometries at frequencies between 2 and 11 Hz. The islands were paced with spatially homogeneous illumination, so cells across each island spiked synchronously and gap junction-mediated conduction did not contribute to the dynamics. We refer to these as zero-dimensional (0D) dynamics.

Tracks were stimulated in small regions (200 μm wide, 100 μm long) to induce 1D propagating waves. We observed the response in both the directly stimulated region (near field) and in the conductively stimulated region (far field; Figure 5.3a). Electrical waveforms stabilized to their far-field dynamics within a distance $d \approx 0.05$ λ from the stimulus ($d = 180\mu$ m in our experiments), so we characterized the far-field dynamics at a distance 750 μm from the stimulus. In the far-field, the waves propagated stably, reaching > 1 cm from the stimulated zone. Island and track fea-

tures were intermixed within each dish, were seeded with the same stock of OS-HEK cells, and were measured simultaneously. Thus, any differences in dynamics between regions could be ascribed to the island geometry.

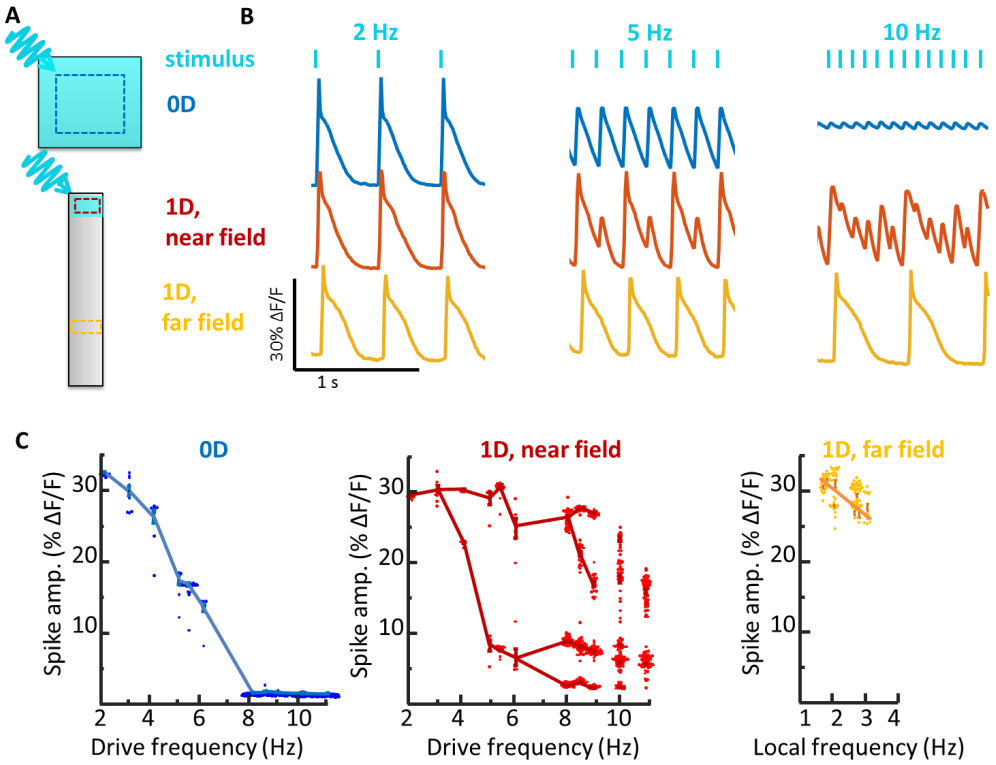

Figure 5.3: Stability of spiking in iOS-HEKs cells depends on sample geometry and location of pacing. (a) Cell culture geometries, with locations of optogenetic stimulus shown in blue and regions of fluorescence voltage imaging shown with dotted lines. (b) Simultaneously recorded electrical dynamics in 0D, 1D near-field, and 1D far-field. At pacing frequencies of 5 and 10 Hz the cells showed different dynamics in the three regions. (c) Geometry-dependent spike amplitude as a function of beat frequency. The plots for 0D and 1D near field show spike amplitude as a function of pacing frequency. The plot for 1D far-field shows spike amplitude as a function of local frequency, which can be a sub-harmonic of the pacing frequency. Fluorescence dynamics were recorded from regions of interest typically 100 μm on a side, containing $\sim$100 cells. Due to the strong gap junction coupling between cells, the fluorescence waveforms of individual cells closely matched the local population average. For each stimulus frequency, the amplitudes of up to 100 spikes were displayed in a beeswarm plot. The lines are a guide to the eye connecting clusters of spikes with similar amplitudes. The data for all plots were recorded simultaneously from adjacent features in the same dish. Each plot represents a recording from a single feature. Similar dynamics were observed in $n = 4$ 0D features and $n = 3$ 1D features.

At low pace frequencies (≤ 3 Hz), all three regions spiked with a stable rhythm in synchrony with the pacing (Figure 5.3b). To our surprise, at higher pace frequencies we observed dramatically different dynamics in the three regions. The 0D

islands always produced regular electrical oscillations at the pace frequency. As the pace frequency increased, the amplitude of these oscillations diminished, up to 8 Hz, beyond which the responses were undetectable (Figure 5.3c).

The 1D near-field response developed a 1:1 alternans pattern at frequencies > 3 Hz. Additional bifurcations arose at 6 Hz and 8 Hz. At 10 Hz the dynamics no longer showed any repeating pattern, suggesting a transition to irregular dynamics (Figure 5.3).

Remarkably, the 1D far-field showed no transitions to alternans or irregular dynamics (Figure 5.3b). All spikes in the far-field had nearly equal amplitude and waveform. At pace frequencies between 3 and 6 Hz, only every other spike propagated to the far-field, that is, the local beat frequency was half the pace frequency. At higher pace frequencies, a smaller portion of spikes reached the far-field. These spikes had irregular timing in the near-field but conducted at velocities which gradually evened out timing variations, such that the spiking appeared regular in the far-field, always at a frequency < 3 Hz. The 1D track acted as a filter which converted high-frequency arrhythmic spiking in the near-field into lower frequency rhythmic spiking in the far field. Together these experiments gave the unanticipated result that under regular pacing, iOS-HEK cells showed irregular dynamics only in the 1D near-field, not in the 0D or 1D far-field regions.

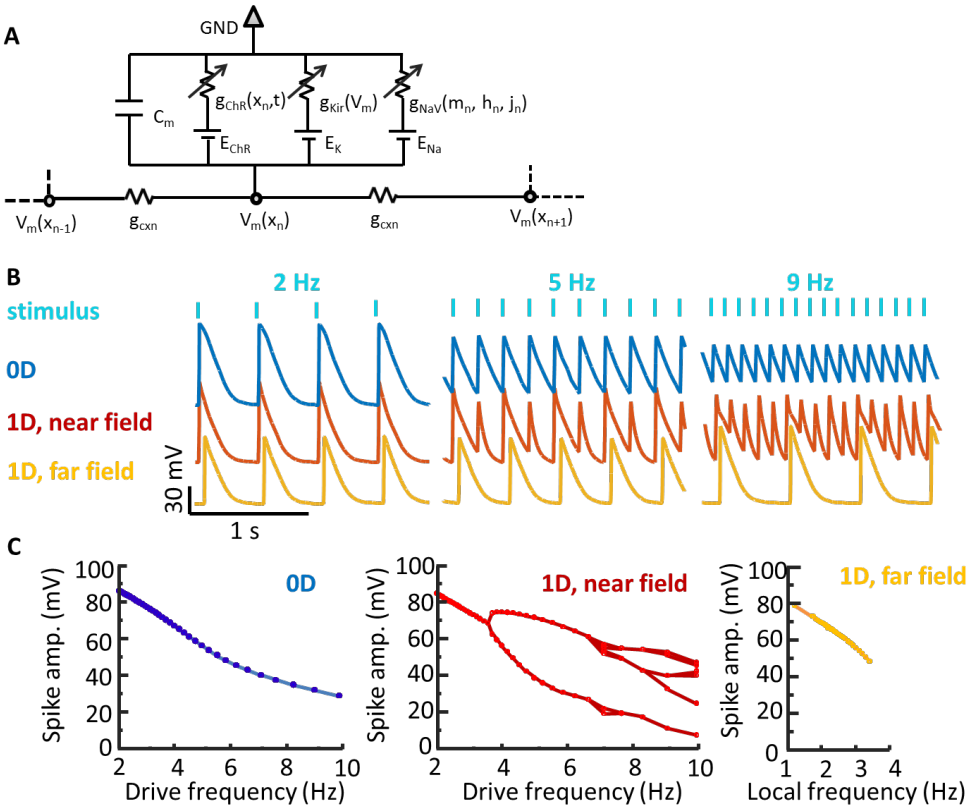

Figure 5.4: (a) Model schematic. Each cell has a channelrhodopsin (ChR), an inward-rectifier potassium channel (K_{ir} 2.1) and a voltage-gated sodium channel (Na_V1.5). The Na_V is further gated by a state-dependent isradipine block. Neighboring cells are coupled via gap junctions. (b) Simulated action potential waveforms in different geometries and pace frequencies (analogous to data in Figure 5.3b). (c) Simulated spike amplitude as a function of frequency for three geometries (analogous to data in Figure 5.3c).

5.3.2 An ion-channel model captures geometry dependent iOS-HEK dynamics

Simulated electrical waveforms (Figure 5.4b) captured the main geometry and frequency-dependent features of the data. Specifically, the simulations in 0D showed a smooth and monotonic decrease in spike amplitude with increasing pace frequency. At high pace frequencies, the baseline potential increased in both simulation and experiment, reflecting simultaneous Na_V channel inactivation and stimulus-driven depolarization relative to the K_{ir} reversal potential (i.e. depolarization block).

Simulations in the 1D near-field showed a series of frequency-dependent bifurcations that became increasingly irregular at high pace frequency. In the 1D far-field, these bifurcations were suppressed: spikes that propagated to the far-field had full amplitude, regular spacing, and were within the narrow band of frequencies that supported far-field propagation.

The simulated 0D waveforms had greater amplitude than the experimental waves at high stimulus frequencies. This minor discrepancy traces to an overestimate of the strength of the channelrhodopsin drive. In all other circumstances, the strength of channelrhodopsin stimulation was not a critical parameter because the channelrhodopsin only served to raise the membrane voltage above threshold. But in the 0D high frequency case, the other ion channels were largely inactive, so the amplitude of the residual voltage fluctuations depended on the strength of the channelrhodopsin drive. Overall, these simulations confirmed that cells with identical conductances, paced at the same frequency, can show widely divergent behavior depending upon the geometry of the surrounding excitable tissue.

5.3.3 Mapping the transition between the near- and far-field responses

We next investigated the transition from near-field to far-field behavior. How does alternans, or even irregular spiking, in the near-field lead to regular spiking in the far-field? We mapped the fluorescence dynamics of 1D tracks as a function of distance from the stimulated zone, across a range of stimulus frequencies (Figure 5.5a,b). There was a clear bifurcation in the ability of spikes to propagate into the far-field.

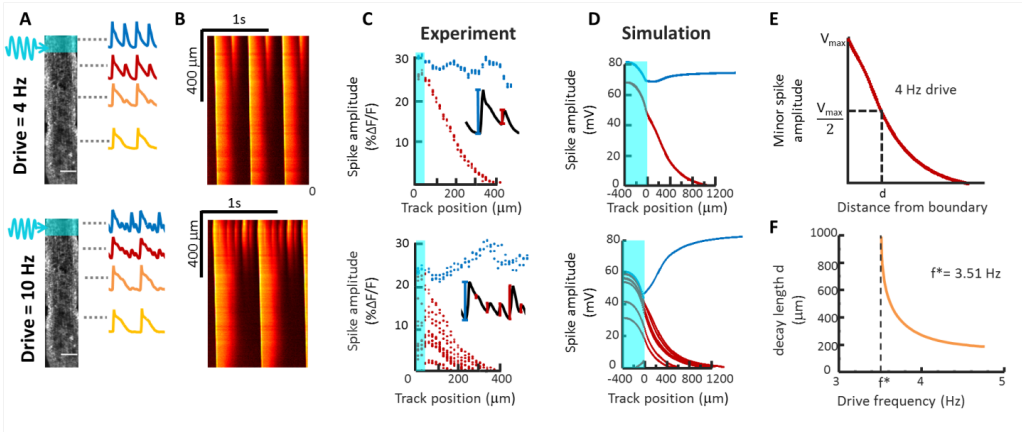

Figure 5.5: Mapping the transition from near field to far field dynamics. (a) 1D tracks were stimulated at one end and action potential waveforms were recorded as a function of distance from the pacing stimulus. (b) Kymographs showing electrical dynamics as a function of distance from the pacing stimulus. Some spikes decay in amplitude, while others grow in amplitude. (c) Quantification of spike amplitude as a function of distance from the stimulus (shown in cyan). Spikes that reach the far-field are shown in blue and spikes that decay are shown in red. (d) Numerical simulations under conditions matched to the experiments. (e) Definition of the spike decay length, corresponding to 50% loss of amplitude. (f) Simulated decay length for near-field spikes as a function of pacing frequency. Below a critical frequency f_* all spikes reach the far field.

Near-field spikes with amplitude lower than a critical threshold decayed as a function of distance, while spikes above this threshold grew to become propagating far-field spikes. Once in the far-field, spikes propagated stably for several cm, until reaching a break in the track. Spatially resolved simulations yielded similar results (Figure 5.5d). The simulations showed that the conduction velocity of each far-field spike decreased as it approached the preceding spike such that irregularities spike spacing gradually evened out. The small dip in the amplitude of propagating spikes near the stimulated zone (Figure 5.5c,d) was traced to a buildup of bound isradipine in cells subjected to rapid optogenetic stimulation.

The propagation of spikes in the far-field is governed by the nonlinear dispersion relation, which defines the relationship between wavenumber and frequency. The numerically simulated dispersion relation shown in Figure 5.8b indicated that the far-field dynamics only supported frequencies up to $f_{max} = 3.85$ Hz. Waves of greater

frequency could not propagate into and are not supported by the far field. More information about the dispersion relation is given in Section 5.5.

At pace frequencies just above the transition to near-field alternans (experimentally observed between 3 and 4 Hz), one might expect period-doubling deviations from a regular spike train to arise slowly. We defined an alternans decay length d as the distance over which a near-field alternans beat decayed to 50% of its initial height (Figure 5.5e). Simulations near the alternans transition indeed revealed a divergence in d near the critical frequency. At pace frequencies far above the critical frequency, the alternans decay length became a small fraction of the far-field action potential length with $d \approx 0.04\lambda$ (Figure 5.5f), consistent with experimental results in Figure 5.5c.

5.3.4 Second-degree conduction blocks in iOS-HEK cells

Conduction block and consequent arrhythmias can arise when a region of the heart acts as a partial barrier to conduction [109]. This effect can arise from spatial variations in either ion-channel expression [110], or gap junctional coupling [111]. We thus explored the effect of local defects on spike propagation in iOS-HEK cell tracks. In a serpentine track with sharp turns, we observed that stably propagating far-field waves sometimes failed at the turns (Figure 5.6a). Furthermore, failures occurred in a regular temporal sequence, that is Figure 5.6a shows a pattern that after the first few beats stabilized into a 3:2 block (3 upstream spikes triggered 2 downstream spikes). The waves developed a curved wavefront and slowed repolarization at the turns, a purely geometrical consequence of the increased electrotonic loading associated with bending a wavefront around a corner. Thus, geometrical effects alone are

sufficient to cause conduction block, even in a background of homogeneous ion channel levels and gap junction strengths. A related effect has been reported in cultured cardiomyocytes, where a junction of a thin strand of cells to a large island showed unidirectional conduction block due to the inability of the thin strand to drive the large island [112].

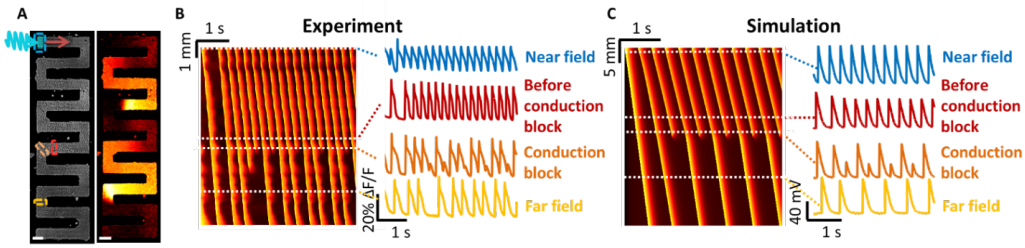

Figure 5.6: Curvature-induced second-degree conduction block in iOS-HEK cell tracks. (a) Left: image of an iOS-HEK cell track showing stimulus region highlighted in cyan and regions of fluorescence monitoring shown with dashed rectangles. Right: single frame from an optical voltage recording showing two action potentials propagating through the track. Scale bars 200 μm. (b) Left: kymograph showing action potential propagation with a 4 Hz pacing frequency. The vertical axis represents contour coordinate along the track. All spikes conducted into the far-field, but conduction showed second-degree block at a corner where there was a slight defect in the pattern, corresponding to the red and orange rectangles. (c) Numerical simulations of second-degree conduction block in a 1D track with a 10 cell zone of 3-fold reduced gap junctional coupling.

In our experiments, the conduction block was attributable to a 2D wavefront curvature effect. To capture this effect in computationally tractable 1D simulations, we simulated linear tracks in which a small region (10 cells) had a reduced gap junctional coupling given by locally setting $G'_{\mathrm{Cxn}} = G_{\mathrm{Cxn}}/3$. The simulated waves showed a 1:1 conduction block (Figure 5.6c), qualitatively similar to that observed experimentally. These experiments and simulations show that local perturbations in the electrotonic coupling, are sufficient to lead to second-degree conduction block.

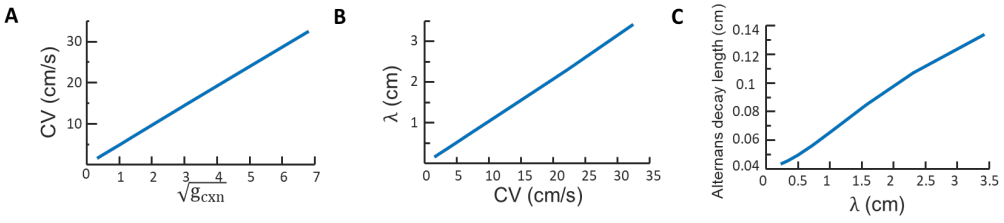

Figure 5.7: Effect of gap junction coupling on dynamics in Hodgkin-Huxley simulations of iOS-HEK cells. (a) Linear scaling of conduction velocity with g_{Cxn}. (b) Linear scaling of depolarized pulse length λ with conduction velocity CV. (c) Relation of the alternans decay length to propagating pulse wavelength at a pacing frequency of 5 Hz, far above the onset of alternans.

5.3.5 Scaling properties of electrical instabilities

Given the importance of gap junction strength and sample geometry, it is interesting to ask whether one can scale both parameters to preserve the overall dynamics. Such scaling could be useful, for instance, in modeling *in vivo* cardiac dynamics in a cell culture system. We explored this question by systematically varying the gap junction strength in iOS-HEK simulations of a 1D track (Figure 5.8a). As anticipated from dimensional analysis, the far-field conduction velocity scaled as $CV \propto \sqrt{g_{\mathrm{Cxn}}}$ (Figure 5.10a). The action potential duration (APD) was largely insensitive to g_{Cxn}, so the action potential length λ scaled as $\lambda \propto \sqrt{g_{\mathrm{Cxn}}}$ (Figure 5.10b). Together these results imply that scaling the size of a system by some factor k and the gap junction strength by $\sqrt{k}$ will preserve the overall dynamics.

The transition frequency for alternans f_* was largely insensitive to g_{Cxn}, varying by $< 2\%$ over a 100-fold change in g_{Cxn} (Figure 5.8a), but f_* depended sensitively on the dynamics of the slow recovery variable (Figure 5.8c). This effect can be understood from the dispersion relation of the iOS-HEK system (Figure 5.8b). Without isradipine ($\alpha = 0$), the far field can support drive frequencies of up to $f_* = 6.5$ Hz (set by the action potential width). As the slow recovery variable j is turned on ($\alpha > 0$), the transition frequency f_* is reduced dramatically. Thus, the maximum

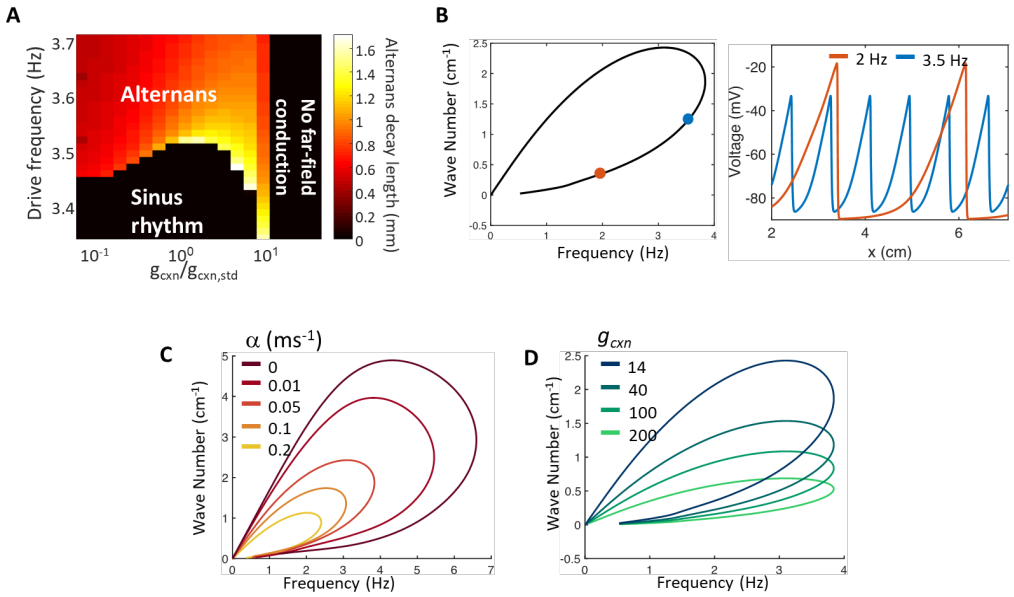

Figure 5.8: Scaling properties of instabilities in iOS-HEK cells. (a) Frequency of near-field alternans onset as a function of gap junction coupling strength. The onset frequency varies by $<$ 2% over a 100-fold variation in g_{Cxn}. Pseudocolor shows the spatial extent of alternans, measured as the distance over which alternans beats decay to half of their value in the stimulus region. (b-d) Nonlinear dispersion relations show which frequencies are stable in far-field and the corresponding wave numbers (inverse of peak-to-peak wavelength) selected by each frequency. In panels b-d, bottom branches of nonlinear dispersion relations are stable and the top branches are unstable. (b) Left: nonlinear dispersion relation under conditions corresponding to experimental data. Right: spatial structure of voltage waves in the far-field with frequencies 2 and 3.5 Hz. Position on nonlinear dispersion relation indicated by correspondingly colored dots. (c) Effect of varying the isradipine binding rate α on the nonlinear dispersion relation. Increasing α decreases the maximum frequency that propagates to the far field. (d) Changes in the connexin strength g_{Cxn} affect the wavelength but have little effect on the maximum stably propagating frequency. Thus, the maximum frequency prior to alternans onset is a parameter that is largely independent of gap junction strength, and by extension, tissue geometry.

stable frequency is a parameter that should be largely independent of gap junction strength, and by extension, tissue geometry – provided that the cells are paced via gap junction-mediated conduction rather than by direct pacing.

Can one extrapolate from in vitro measurements of small samples with relatively weak gap junction coupling to larger tissues with stronger gap junctional coupling? In iOS-HEK simulations, the alternans decay length d scaled almost linearly with λ (Figure 5.7c). These simulations suggest that the action potential length λ sets a natural length scale for a bioelectric tissue. Moreover, using λ as a scaling param-

eter is advantageous since this parameter can be experimentally measured without knowledge of gap junction conductance or other system parameters.

The conduction velocity in the atria and ventricles of the human heart in vivo is approximately 50 cm/s [113, 114], and action potential durations are typically 350 ms, implying an action potential length of $\lambda = 18$ cm. An adult human heart is approximately $L = 12$ cm long, so $L \approx 0.7\lambda$. Pacemaker-triggered action potentials *in vivo* are thus primarily in the near-field and close far-field regimes. Remarkably, the near-field is the only regime in which we observed arrhythmias in either the iOS-HEK cells or in the hiPSC-CMs, either in experiment or in simulation.

In the cultured hiPSC-CM the action potential length was λ =2.6 cm, so to best match the geometrical regime of the heart, the culture should have size $L \approx 0.7\lambda$, or ~ 1.7 cm. Others have reported conduction velocities in vitro ranging from 3.5 to 20 cm/s [93, 115, 116], corresponding to λ =1.2 to 7 cm (assuming a 350 ms AP width). While cultures of size $L \approx 0.7\lambda$ are easily accessible on the smaller end of the λ-range, 5 cm-wide hiPSC-CM cultures are impractical. This challenge can be addressed either by cell patterning to produce serpentine tracks, or by adding gap junction blockers such as 2-APB to diminish the strength of the gap junction coupling and thereby to slow the conduction velocity.

In vivo, the heart is paced by autonomous cells in the sinoatrial node, which initiate waves that propagate across the myocardium. To best mimic wave conduction in the heart, cultures of hiPSC-CM should be stimulated locally to launch propagating waves. Whole-field stimuli, e.g. as delivered by field stimulation electrodes or wide-area optogenetic stimulation, will induce synchronous depolarization of all cells, mimicking the 0D case and missing possibly important gap junction-mediated

dynamical instabilities. One should ideally perform spatially-resolved voltage measurements to reveal the distinct dynamics in the near- and far-field regimes. While it is not possible to recapitulate the full spatial structure of connectivity of the adult myocardium *in vitro*, one can use the *in vitro* measurements to benchmark dynamical regimes according to biophysical parameters (e.g. λ and L) which can be measured *in vivo*. We expect that these considerations will be important for ongoing efforts to develop *in vitro* models of cardiac dynamics.

5.3.6 Geometry dependent instabilities in human iPSC cardiomyocytes

Finally, we explored whether the geometry-dependent effects observed in iOS-HEK cells also occurred in human iPSC-derived cardiomyocytes (hiPSC-CM) [117]. Due to the significant commercial interest in using these cells as an *in vitro* model for cardiotoxicity testing [96, 97, 118–120], the correspondence (or lack of) between *in vitro* and *in vivo* arrhythmias has some practical importance.

We used microcontact printing to define side-by-side patterns of 0D islands and 1D tracks and then plated hiPSC-CM onto these patterns (Figure 5.9b). CheRiff was expressed using a lentiviral vector to allow patterned blue light stimulation [115], and BeRST1 was used to image changes in membrane potential. We optogenetically paced 0D islands and 1D tracks simultaneously across a range of frequencies with pulses of 50 ms duration. In the 1D tracks, waves propagated with a conduction velocity of 7.2 cm/s and had an AP duration of 360 ms, corresponding to a depolarized action potential length of 2.6 cm.

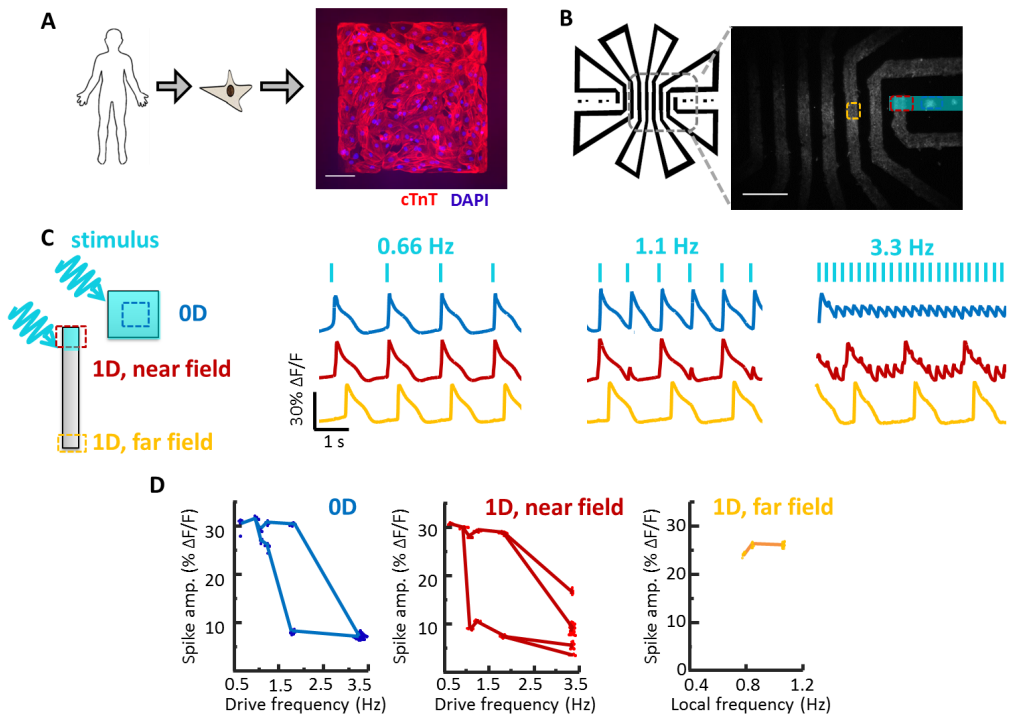

Figure 5.9: Geometry-dependent arrhythmias in cultured human iPSC-derived cardiomyocytes (hiPSC-CM). (a) Image of hiPSC-CM grown on a patterned square island. Scale bar 100 μm. (b) Patterned hiPSC-CM cell growth in a set of 0D islands and a long 1D track. The track geometry was designed to interpose long path lengths between returns to the field of view (2 cm between red and yellow regions of interest), to account for the high propagation speed of action potentials in hiPSC-CM compared to iOS-HEK cells. Scale bar 1 mm. (c) Simultaneously recorded electrical dynamics in 0D, 1D near field, and 1D far field. At elevated pacing frequencies the cells showed different dynamics in the three geometrical regimes. (d) Quantification of the action potential height as a function of frequency in the three geometrical regimes.

As with the iOS-HEK cells, we observed that the dynamics depended strongly on the geometry (Figure 5.9c). At high pace frequency (3.3 Hz), the 0D islands showed small regular oscillations, the 1D near-field showed an erratic pattern of large beats with small oscillations superposed, and the 1D far-field only showed the large beats at a sub-harmonic of the pace frequency. As in the iOS-HEK cultures, the alternans beats decayed over a distance much less than the action potential length (decay length $d = 535\mu$m, corresponding to $d = 0.2\lambda$). Thus the qualitative geometry-dependent behavior of the hiPSC-CM largely mirrored the behavior of the iOS-HEK cells.

The hiPSC-CM cells differed from the iOS-HEK cells in several important regards. First, the hiPSC-CM were spontaneously active, imposing a minimum on the optogenetic pace frequency. Second, the 0D hiPSC-CM islands showed a transition to alternans (Figure 5.9c,d) which disappeared at high drive frequencies (3 Hz). Third, the 1D bifurcation to alternans was continuous in the iOS-HEK cells but discontinuous in the hiPSC-CM. In iOS-HEK simulations, these last two differences can be captured simply by tuning the isradipine unbinding rate (Figure 5.10b). We also simulated the Noble model, a more realistic cardiac model based on recordings from Purkinje fibers [121]. As in the simplified Hodgkin-Huxley model, we observed clear geometry-dependent differences in the onset of instabilities (Figure 5.10c). Finally, real cardiac tissue can support alternans in far-field traveling waves 50, while both the iOS-HEK cells and the hiPSC-CM seemed only to support this phenomenon in the near field. Thus there remain important dynamical features of real cardiac tissue which appear not to be captured by either the iOS-HEk cells or the hiPSC-CM.

5.4 Discussion

Gap junction-mediated currents convey the effects of boundaries to all cells in the tissue. In the highly simplified iOS-HEK 'toy' model, the qualitative spiking dynamics depended in a sensitive way on the overall geometry. Islands of composed of identical cells and differing only in geometry showed vastly different dynamics under identical pacing frequencies, including regular spiking, complex but repeating multi-spike patterns, and irregular spiking. This work further highlighted the importance of a slowly recovering conductance (in our case state-dependent isradipine block) to support transitions to alternans and arrhythmia.

Our experimental and theoretical approach was guided by the aim to make the simplest possible models that captured key aspects of excitable dynamics. The iOS-HEK system was simple enough to model with biophysically realistic numerical simulations, which confirmed that the observations could be explained by geometry alone. The iOS-HEK cells bore little resemblance to cardiomyocytes from a molecular perspective, lacking, for instance, voltage-gated Ca^{2+} channels, calcium-induced calcium release, delayed rectifier potassium channels, and mechano-electrical feedbacks. The observation of similar geometry-dependent bifurcations in hiPSC-CM cultures suggests that similar principles apply to physiological tissues, despite the myriad differences in channel expression and electrophysiological details between the iOS-HEK cells and cardiomyocytes. Indeed, several distinct models of excitable dynamics all showed geometry dependent bifurcations and transitions to irregular dynamics (Figure 5.10c). Based on these observations, we propose that long-range electrical signaling may be a generic mechanism for conveying information on tissue geometry to cells interior to a tissue [122].

To demonstrate that the observed geometry effects are not unique to the iOS-HEK cell model and are of importance in cardiac dynamics, we performed 0D and 1D simulations in the Noble model. The Noble model is an ionic channel model for Purkinje fibers in cardiac tissue. The full model, ionic currents and system parameters are described in Section 5.5.3. The Noble model was chosen for its ability to reproduce realistic behaviors observed in cardiac cells and the relatively low number of ionic currents allowed for efficient simulation. The Noble model simulations also exhibit geometry-dependent changes in stability (Figure 5.10). The 1D near-field results show a dramatic transition first to alternans at 4.5 Hz, and then to irregular dynamics at 8 Hz. Similar transitions are not observed in the 0D or far-field results, which

instead display monotonically decreasing spike amplitude for higher frequencies. As before, the model selects a narrow range of wave frequencies which propagate into the far-field.

We argue that a cardiomyocyte in isolation would behave very differently from one embedded in a two-dimensional culture or one embedded in a real heart – even if the ion channels were identical in all three cases. This fact suggests skepticism toward the aspects of the CiPA initiative which propose extrapolating from *in vitro* measurements of arrhythmia to *in vivo* predictions. One should not naively infer that a pro-arrhythmic compound *in vitro* will be pro-arrhythmic *in vivo*. Indeed, different cell culture geometries and different mechanisms of pacing can produce dramatically different results *in vitro*. By analyzing the scaling properties of waves in excitable tissues, we propose that to best mimic conditions *in vivo*, hiPSC-CM should (a) be stimulate via gap junction-mediated conduction, and not by direct electrical or optogenetic stimulation, and (b) that the ratio of culture size to action potential length should approximately mimic the corresponding ratio *in vivo*.

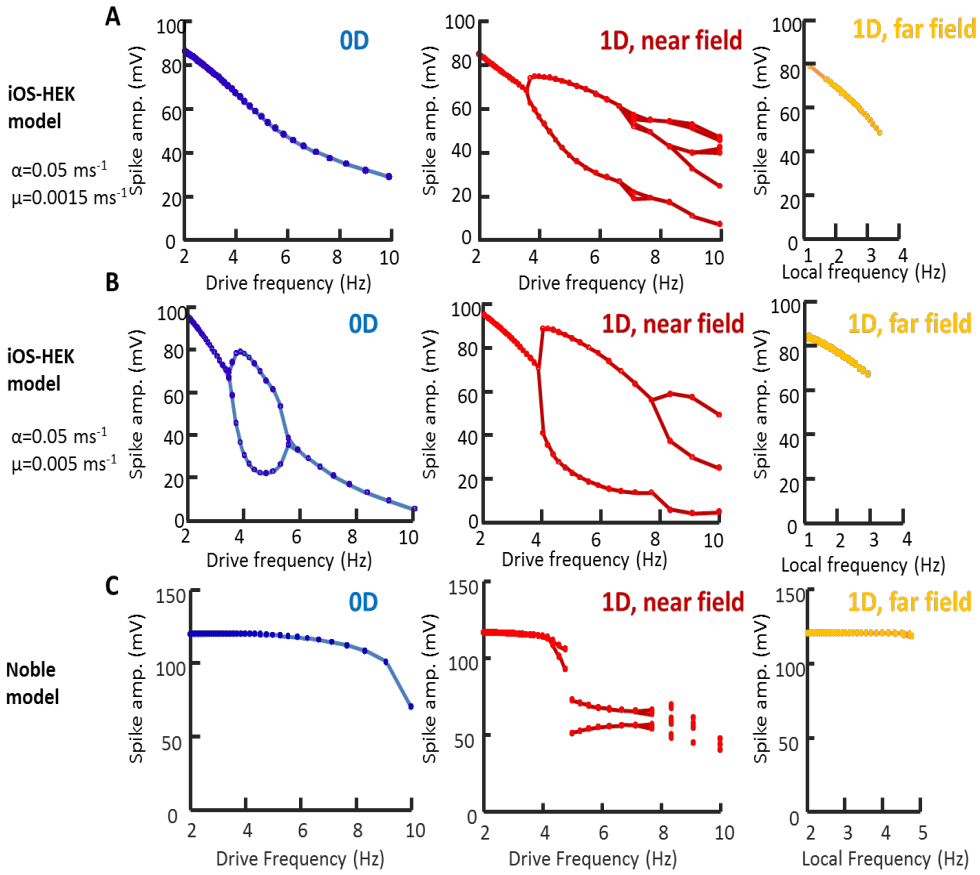

Figure 5.10: (a) Hodgkin Huxley model of iOS-HEK cells (same as Figure 5.4c, repeated here for comparison to other models). (b) Same as (a) with artificially accelerated israpidine unbinding kinetics ($\mu = 0.005$ ms^{-1}). 0D features show alternans at intermediate drive frequencies. The 1D near field shows a discontinuous alternans transition. (c) Simulation of the cardiac Noble model [121], which also shows geometry-dependent changes in dynamics.

5.5 Chapter Appendix

5.5.1 Fitting model parameters and sensitivity analysis

Initial model parameters were experimentally constrained and fit using a combination of patch clamp measurements and fluorescent voltage recordings. Reversal potentials of $E_{Na} = 75$ mV, $E_K = $ -107 mV, and $E_{ChR} = 0$ mV were determined according to

Nernst equation for the corresponding intracellular and extracellular ionic concentrations. All conductances were expressed as specific conductances per unit capacitance, allowing us to set $C_m = 1$. The sodium conductance g_{NaV} was set to 1.5 nS/pF, corresponding to a maximum transient current of 3 nA at -25 mV ($V - E_{Na} = -100$ mV) measured in a 20 pF patch clamp recording. The channelrhodopsin conductance was determined to be 15 pS/pF following similar methodology. The inward rectifying potassium current g_{Kir} was represented as an instantaneous function of voltage, determined by fitting to the experimentally observed fluorescence repolarization waveform at low drive frequency (2 Hz). Because fluorescence traces do not report absolute voltage, we assumed a resting potential of -90 mV and peak voltage of + 30 mV, in accordance with patch clamp recordings. The diffusion coefficient G_{Cxn} is given by $G_{\mathrm{Cxn}} = g_{\mathrm{Cxn}} \times \ell^2$, where $\ell = 1$ cell. The connexin conductance g_{Cxn} was estimated according to measurements of the static electronic coupling length [100] as 40 nS/pF.

The parameters α and μ were chosen to match experimentally determined dynamical regimes. Setting $\alpha = 0.5\mathrm{ms}^{-1}$ and $\mu = 0.015\mathrm{ms}^{-1}$ gave close agreement with the complex landscape of dynamical transitions observed experimentally (Figure 5.4c) as well as simulated voltage traces which closely resembled experimental observations (Figure 5.4b). Sensitivity analysis was performed to validate these parameter choices.

Model dynamics were characterized using analogous parameters as for experimental results. Simulations were conducted for both an isolated cell which was directly paced as well as for linear tracks of 2000 cells (i.e. $L = 2$ cm) in which 40 cells were paced on one end. Simulations were run across a range of stimulus intervals between 500 ms (2 Hz) and 100 ms (10 Hz), sampled at 10 ms intervals. For each numerical experiment, we detected spike upstrokes as upward deflections of the derivative of

the simulations.

Parameter values for $\alpha, \mu, g_{\text{NaV}}$, and g_{Cxn} were selected to match as closely as possible the experimental results in both the 0D and 1D settings. The model was simulated for 1,500 ms with a given set of parameters under 2 Hz stimuli, and the resulting voltage at times t_k, $V(x, t_k)$ was compared to analogous experimental results $W(x, t_k)$ using the ordinary least squares (OLS) objective function

$$OLS_{obj} = \sum_k \left| W(x, t_k) - V(x, t_k) \right|^2.$$

Simulated and experimental voltage values were scaled to be between 0 and 1 to allow for direct comparison. An optimal set of parameters minimizes the objective function; minimization was performed with the MATLAB constrained optimization function fmincon. Realistic parameter constraints were chosen from the patch clamp data.

Sensitivity of model parameters was tested using Latin Hypercube Sampling (LHS) [123]. The LHS results identified α, μ, and g_{NaV} as the most sensitive parameters with g_{Cxn} as the least. That is, small changes in the connexin strength, g_{Cxn} had negligible impact on the simulated voltages. Regardless, changing any model parameters over a modest regime maintained the main geometry-dependent differences in stability, giving confidence in the appropriateness of the model.

5.5.2 Nonlinear dispersion analysis of far-field dynamics

In the far-field, the waves become spatially periodic structures of constant shape and velocity, both of which are uniquely determined by the frequency. The nonlinear dis-

persion relation of the far-field equation indicates which wave number (inverse of peak-to-peak wavelength) is selected by each frequency (Figure 5.8(b-d)). The nonlinear dispersion relation is computed by considering the far-field traveling waves as periodic stationary solutions in a moving frame, which allows for the traveling wave and wave number to be solved for as a function of frequency. The full dispersion relation curve is traced out with pseudo-arclength numerical continuation implemented in MATLAB, and using the spatial discretization scheme as in the numerical simulations.

Each frequency has two associated wave numbers, with the bottom branch stable and top branch unstable. Two examples of the spatial structure of the far-field waves are given, and their positions along the dispersion relation marked. The curve does not extend past 3.85 Hz, indicating the far-field equation does not support waves of higher frequencies. Therefore, for drive frequencies above 3.85 Hz, each stimulus will not propagate into the far-field, leading to the appearance of near-field alternans, and aligning with the experimentally and numerically observed behavior.

Changing the drug binding rate α (Figure 5.8c) and connexin strength g_{Cxn} (Figure 5.8d) have different impacts on the nonlinear dispersion relation. Small changes in α lead to large shifts in the transition frequency, indicating that faster binding rates will induce near-field alternans at lower drive frequencies. However, large changes to the coupling strength change properties of the traveling waves, such as wave number, wave length, and speed, but do not appreciably change the range of allowed frequencies or transition frequency. Changes to model parameters μ (drug unbinding rate) and g_{Na} (sodium conductance) are not shown, but have a similar effect as changing α.

The 2:1 conduction block observed from local changes in the connexin strength

(Figure 5.6) is also explained from the nonlinear dispersion relation. As the spike propagates through the small region of lower connexin strength, the wavenumber and frequency are adjusted to values that are no longer stable when the wave reenters the region of higher connexin strength (observe the differences in the curves with g_{Cxn} values of 40 and 14 in Figure 5.8d). The modification of wavenumber and frequency upon the reentry results in the observed 2:1 conduction block.

5.5.3 Noble model of cardiomyocyte dynamics

The Noble model is an ionic channel model for Purkinje fibers and the voltage dynamics are governed by sodium, potassium, and background chloride currents (I_{Na}, I_K, and I_{cl}, respectively). Spatial coupling between cells was again incorporated through a Laplacian Δ. Model equations are given by

$$\begin{aligned}
C_m \frac{\partial V}{\partial t} &= \delta \Delta V - (I_{Na} + I_{K1} + I_{K2} + I_{cl} + I_{ext}) \\
I_{Na} &= \left(\bar{g}_{na} m^3 h + g_{Na}\right)(V - E_{Na}) \\
I_{K1} &= \left[g_k \exp\left(\frac{-V - 90}{50}\right) + 0.015 \exp\left(\frac{V + 90}{60}\right)\right](V - E_K) \\
I_{K2} &= g_K n^4 (V - E_K) \\
I_{cl} &= g_{cl}(V - E_{cl}) \\
I_{ext} &= g_{stim}(V - E_{ChR}).
\end{aligned}$$

The dynamics of the dimensionless ionic gates for sodium activation m sodium deactivation h and potassium n take the form

$$\frac{dz_i}{dt} = \alpha_i(V)(1 - z_i) - \beta_i(V) z_i,$$

where z_i stands for m, h, and n and α_i and β_i similarly correspond to opening and closing rates of the m, h, and n channels. The rates are given by

$$\alpha_m(V) = 0.1(V+48)\left(1-\exp\left(\frac{-V-48}{15}\right)\right)^{-1}$$
$$\beta_m(V) = 0.12(V+8)\left(\exp\left(\frac{V+8}{5}\right)-1\right)^{-1}$$
$$\alpha_h(V) = 0.17\exp\left(\frac{-V-90}{20}\right)$$
$$\beta_h(V) = \exp\left(\frac{-V-42}{10}\right)^{-1}$$
$$\alpha_n(V) = -0.0001(V+50)\left(\exp\left(\frac{-V-50}{10}\right)-1\right)^{-1}$$
$$\beta_n(V) = 0.002\left(\exp\left(\frac{-V-90}{80}\right)\right)^{-1}.$$

All ionic currents, dynamic gating variables, and parameter values were set from literature. Membrane capacitance, conductances, and Nernst potentials are given in Table 5.3 [121, 124]. The form of the applied current I_{ext} was set to mimic the channelrhodopsin stimulus.

$C_m = 12\mu\text{F/cm}^2$	$\bar{g}_{Na} = 400\ \text{mS/cm}^2$
$E_{Na} = 40\ \text{mV}$	$g_K = 1.2\ \text{mS/cm}^2$
$E_K = -100\ \text{mV}$	$g_{cl} = 0.075\ \text{mS/cm}^2$
$E_{cl} = -60\ \text{mV}$	$g_{stim} = 0.5\ \text{mS/cm}^2$
$\delta = 0.001\ \text{cm}^2\text{/ms}$	

Table 5.2: Values of membrane conductance, conductances, and Nernst potentials used in simulations of the Noble model.

Numerical simulations in 0D and 1D geometries used the same centered finite-difference Laplacian and IMEX time evolution schemes described above. Simulations were run on 1D tracks of up to 6 cm in length with spatial grid spacing set to 0.1 mm and time step of 0.01 ms. Due to the higher cell coupling and conduction values, the stimulus duration was increased to 50 ms. Simulations were run for at least two

forcing cycles before recording results to remove any transient effects caused by the self-spiking behavior of the Noble model. Model output was analyzed in a similar fashion to the OS-HEK model results.

5.5.4 Experimental details

5.5.4.1 iOS-HEK cell line generation, culture, and patterning

All HEK cells were maintained in Dulbecco's modified Eagle medium with 10% fetal bovine serum (DMEM-10), penicillin (100U/mL), and streptomycin (100μg/mL). OS-HEK cells were generated as described previously [100]. Briefly, a $Na_V1.5$ plasmid (Johns Hopkins University ChemCORE) containing a puromycin selection marker was transfected into HEK cells using TransIT-293 transfection reagent (Mirus Bio). 48 hours after transfection, 2 μg/mL puromycin was introduced into the culture medium for 14 days to select for stably expressing $Na_V1.5$ cells. Following this selection, an Optopatch construct containing coding sequences of CheRiff-eGFP and QuasAr2-mOrange (separated by a self-cleaving P2A peptide sequence) was introduced using a lentiviral construct [103]. GFP-expressing cells were enriched 10 days after infection via fluorescence-activated cell sorting (FACS). Finally, a $K_{ir}2.1$ lentiviral construct containing a blasticidin selection marker was introduced. After 2 days, cell culture media was supplemented with 5 μg/mL blasticidin (to select for $K_{ir}2.1$-expressing cells) and 2 μg/mL puromycin (to ensure continued $Na_V1.5$ expression). After 14 days, cells were dispersed as single cells into a 48 well plate, and clonal populations were selected on their ability to spike robustly in response to a blue light stimulus.

Clonal cell lines were maintained in DMEM-10 supplemented with 5 μg/mL blasticidin and 2 μg/mL puromycin in 10 cm tissue culture dishes up until 80% confluence, after which they were trypsinized and cryopreserved at 500,000 cells/vial in 90% DMEM-10, 10% dimethylsulfoxide (DMSO). Cryopreserved vials were then thawed and subcultured in antibiotic-supplemented DMEM-10 in 10 cm tissue culture dishes, and were passaged via trypsinization at 80% confluence at a 1:3 ratio. A given subculture typically maintained robust blue-light induced spiking for approximately seven passages, or 2 weeks, after which cells become less excitable (presumably due to decreased $K_{ir}2.1$ expression over time).

To prepare OS-HEK cells as iOS-HEK cells for functional experiments, cells were incubated in Tyrodes solution (containing 125 mM NaCl, 2 mM KCl, 2 mM $CaCl_2$, 1 mM $MgCl_2$, 10 mM HEPES, 30 mM glucose; pH 7.3, osmolality 305-310 mOsm) further supplemented with 10 μM isradipine and 1 μM BeRST1 voltage-sensitive dye for 30 minutes in a mammalian tissue-culture incubator prior to imaging.

5.5.4.2 Cell patterning

Patterned cell growth was achieved using previously microcontact printing described methods [100, 106]. Cytophilic fibronectin patterns were defined on a functionalized cyotophobic polyacrylamide gel using microcontact printing with patterned PDMS stamps. Patterns were first designed *in silico* (Inkscape) and printed onto a Mylar transparency mask (CAD Art Services). Pattern negatives were then transferred onto silicon wafers coated in SU-8 3025 via contact photolithography and subsequent development of unexposed photoresist. PDMS stamps were then cast from the silicon wafer template.

Functionalized polyacrylamide dishes were prepared from MatTek 35 mm-glass bottom dishes. Glass coverslips were chemically activated by plasma cleaning and then incubated for 30 min in a nitrogen-purged glovebox with silane solution (v/v: 0.5% 3-methacryloxypropyltrimethoxysilane, 2% acetic acid, 97.5% anhydrous EtOH). A 40:1 acrylamide:bisacrylamide gel doped with 4.2 mg/mL acryl-NHS (to allow for covalent bonding of fibronectic matrix) was then gelled for 2-3 minutes in ambient air under siliconized coverslips (to ensure smooth gel surfaces). Functionalized acryl-NHS dishes were then sealed in nitrogen and drierite and transferred to -80 C for long-term storage.

To complete dish preparation, patterned PDMS stamps were first coated in fibronectin protein (Yo Proteins no. 663) dissolved in PBS (0.05mg/mL fibronectin final concentration) in a sterile tissue culture hood. Coating was allowed to settle for 30 minutes, after which excess fibronectin-PBS solution was carefully removed via aspiration. Stamps were further air-dried for 10 minutes to remove excess moisture that could blur pattern transfer. Functionalized dishes were then printed with fibronectin-coated stamps for 1 hour in a tissue-culture incubator, after which stamps were gently removed and dishes re-sterilized for 10 minutes with UV illumination. Cells were deposited by gently pipetting 500 μL DMEM-10 droplet containing the desired cell density (typically between 500,000 and 1M cells/mL). Cells were allowed to adhere for 30 minutes in a tissue culture laminar hood before an additional 2 mL of DMEM-10 was added and cells were transferred to an incubator.

5.5.4.3 Wide-field all-optical electrophysiology

All-optical electrophysiology of iOS-HEK and hiPSC-CM cells was performed using an adapted 'Firefly' ultrawidefield inverted microscope [125]. Spatially patterned

blue excitation for optogenetic stimulation was achieved using digital micromirror device (DMD) module with an onboard 460 nm LED (Wintech DLP Lightcrafter 4500). Pixels of linear dimension 7.637 μm were demagnified 2x for optical pattern resolution of approximately 3.8 μm. Action potentials in iOS-HEK cells were triggered with 10 ms pulses at 100 mW/cm^2; action potentials in hiPSC cardiomyocytes were triggered with 50 ms stimuli. Patterns were defined using custom software (MATLAB). DMD pixels were mapped to sample pixels by calibrating a linear transformation to a test pattern on a fluorescent target.

Near-infrared voltage sensors were excited using widefield 635 nm illumination (DILAS 8 W diode laser, M1B-638.3-8C-SS4.3-T3) configured in a near-TIRF configuration (to reduce background autofluorescence). Robust signals from BeRST1 were obtained at an illumination intensity of 2 W/cm^2. Near-infrared fluorescence emission was filtered using emission filters (Chroma ET665lp and Semrock quadband 336/510/581/703) and reimaged onto a sCMOS camera (Hamamatsu Orca Flash 4.2). Movies were acquired at 100 Hz over a 5 mm x 5 mm field of view.

Custom LabView software allowed for synchronization of time-modulated signals controlling blue and red light excitation, DMD patterns, and camera acquisitions over experimental runs. All data were processed and analyzed using custom software (Quantification and Statistical Analysis). To investigate geometry-dependent dynamical regimes, spatial regions of interest (ROIs) were defined and averaged across pixels to give fluorescence time-traces. A single set of ROIs was defined for a given sample dish and was applied uniformly across movies at different drive frequencies to systematically investigate dynamical responses (Figures 5.3b and 5.9c). Using these spatially resolved measurements, we extract information from multiple replicates of 0D, 1D near-field, and 1D far-field responses all in a single dish.

5.5.4.4 Image processing and experimental data analysis

All data were processed and analyzed using custom software (MATLAB). For each pixel, a baseline fluorescence F was calculated from the first percentile of the values in the recorded time-trace. The movie was then converted into units of $\Delta F/F$. Pixels that did not contain cells were set to zero (using a criterion that the 99th percentile of a time trace must be over a user-specified threshold). A spatial median filter (5x5 pixel filter) was further applied to account for measurement noise. At the illumination intensities used, BeRST1 photobleaching was negligible.

To investigate geometry-dependent dynamical regimes, spatial regions of interest (ROIs) were defined and averaged across pixels to give fluorescence time-traces. A single set of ROIs was defined for a given sample dish and was applied uniformly across movies at different drive frequencies to systematically investigate dynamical responses (Figsures 5.3b and 5.9c). Using these spatially resolved measurements, we extract information from multiple replicates of 0D, 1D near-field, and 1D far-field responses all in a single dish.

We extracted action potential amplitudes for each spike detected in each feature across movies taken at different pacing frequencies. Spike upstrokes were detected via a threshold on the time derivative. Spike amplitudes (in units $\Delta F/F$) were defined as the difference between the maximum value after a given upstroke and the minimum value preceding the upstroke. Between 10 and 300 spikes per feature were collected in a given movie, depending on drive frequency and acquisition time. Beeswarm plots of spike amplitudes at each pacing frequency were used to visualize the dynamical patterns of activity (Figures 5.3c and 5.9d). Only spikes taken from the second half of movies are visualized to avoid early transients which decay as

patterns converges to a stable cycle. The drive frequency in 0D and 1D near field measurements was set by the frequency of the blue light-gated CheRiff activation; in 1D far-field measurements, the pacing frequency is defined as the local frequency (i.e., the reciprocal of the interval between successive spikes).

The transition between the near-field and far-field region was mapped using kymographs (Figures 5.5b and 5.6b). Kymographs were generated by spatially averaging $\Delta F/F$ movies across the short dimension of a linear track. For serpentine tracks (Figure 5.6), tracks segments were first computationally aligned into a single long track, and then spatially averaged along the short dimension. Alternans transitions were spatially mapped by performing spike detection (as described above) across linear windows of 8 pixels (Figure 5.5c).

5.5.4.5 Key Resource Table

Reagent or Resource	Source	Identifier
Chemicals, Peptides, and Recombinant Proteins		
Isradipine	Tocris Bioscience	2004
Puromycin	ThermoFisher	A1113802
Blasticidin	ThermoFischer	A1113902
Fibronectin	Yo Proteins	Cat #663
Acrylic acid N-hydroxysuccinimide ester	Sigma	A8060
Acrylamide solutoin (40%)	Sigma	A4058-100ML
Acrylamide/Bisacrylamide, (40% solution, 19:1)	Sigma	A9926-100ML
SU-8 3025 Photoresist	Microchem	SU-8 3025
SU-8 Developer	Microchem	N/A
3-(Trimethoxysilyl)propyl methacrylate	Sigma	2530-85-0
Anhydrous ethanol	Sigma	277649-100ML
Glacial acetic acid	Sigma	A6283-100ML
Potassium persulfate	Sigma	7727-21-1
Experimental Models: Cell Lines		
Optopatch-Spiking HEK Cells	This paper, [100]	N/A
iCell Cardiomyocytes	Cellular Dynamics	Kit 01434
Recombinany DNA		
pENTR-L5-Kir2.1-mCherry-L2	Addgene	32,699
pIRESpuro3-NaV1.5	Johns Hopkins University ChemCORE	N/A
FCK-Optopatch1	[103], Addgene	51695
FCK-CMV-CheRiff-CFP	N/A	
psPAX2	Addgene	12260
VsVg	Addgene	12259
Software and Algorithms		
MATLAB code for image processing and data analysis	This paper	Supplement
MATLAB code for iOS-HEK model simulation and dispersion analysis	This paper	Supplement
MATLAB code for Noble model simulation	This paper	Supplement
Other		
Firefly Widefield Microscope	This paper, [125]	N/A/
Silicon Wafers	University Wafers	58.52-1
Lithography transparency mask	CADArt Services	N/A (custom order)

Table 5.3: Key resource table.

Chapter Six

Conclusions

6.1 Summary of contributions

In this work we explored the stability of and transitions observed in periodic traveling waves in chemical oscillations and excitable systems, focusing on domain geometry and extension of spectral stability concepts to systems with a singular diffusion matrix. Below we summarize the findings and contributions related to each factor.

6.1.1 Domain geometry

Physical domains are often spatially extended with separated boundary conditions and understanding how patterns behave on these domains is not only an interesting mathematical problem, but is important for applications. We find that the domain directly influences the development of instabilities in the case of externally forced tissues and in the self-sustained oscillations of spiral waves. Our results of traveling waves and spirals urge caution to scientists trying to extrapolate findings from small patches of cells to spatially extended tissues or in restricting patterns from infinite to bounded domains: the types of behaviors observed in one setting are not necessarily true or relevant for all others.

In Chapter 3 we presented a technique for determining if point eigenvalues arise from extended point spectrum associated with the spiral core, absolute spectrum and far-field dynamics, or the boundary sink. Bifurcations arising from boundary effects will only be relevant on finite domains and the specific boundary conditions will influence the structure of the instability. This phenomenon is seen in the Rössler system, where we find line defects are a direct consequence of unstable point eigenvalues from the boundary sink. Using mixed Robin-style boundary conditions changes the

form and stability of the line defects eigenfunction, meaning the boundary conditions (and likely the domain shape) directly define the structure of the perturbation.

The methodology can also be used to rule out boundary contributions. Unstable eigenvalues responsible for alternans in the Karma model arise from the spiral core and were unaffected by modifications to the boundary conditions. These results reveal that alternans will be generated regardless of the domain and provide justification for studying spiral waves in cardiac models on the simpler geometry of bounded disks.

Moreover, experimental and numerical results of iOS-HEK cells show how the dynamics and transitions to arrhythmic rhythms depends on the tissue geometry and proximity to pacing site. In the 0D cell islands, stimuli and spikes are in a 1-1 correspondence independent of pacing frequency, but is not true in tissues where differences in voltage responses depend on the distance from stimuli. The dispersion relation of the far-field traveling waves provides mathematical understanding of why pacing rates above 3.5 Hz do not propagate into the far-field - the media does not support waves with frequencies above this threshold. In particular, care needs to be taken to determine if the near or far-field region is relevant, and we suggested a scaling based on the far-field wave length.

6.1.2 Effect of singular diffusion matrix on essential spectrum

Many realistic reaction-diffusion systems describing biological and physical phenomenon contain variables for which diffusion is unphysical; gating variables in the

iOS-HEK system is an example. The effect of the non-full rank and singular diffusion matrix on spectral properties has not previously been explored. Here, we determined that the spectra on unbounded and bounded domains exhibits abrupt discontinuous transitions as the diffusion of the slow species limits to zero, and in Chapter 4 focused on understanding the behaviors in the essential spectrum.

Regardless of the diffusion coefficients, the eigenfunction of the fast species decays in norm along the essential spectrum branches and is bounded by the slow-diffusing eigenfunction. In the limit of a non-diffusing slow species, the perturbation analysis of the essential spectrum near the finite limit point indicated the location is set by the non-diffusing species. An application to the Barkley model numerically confirms the theoretical predictions and reveals the spectral differences caused by the diffusion coefficient.

6.2 Future directions

The numerical and analytical techniques that applied in this thesis can be extended to patterns formed in reaction-diffusion systems across a wide variety of applications. In particular, the methodology presented in Chapter 3 can be applied to understand origins of instabilities in patterns forming systems in biology, social systems, or ecology.

6.2.1 Spiral waves in cardiac dynamics

There are two natural directions to broaden the presented results on spiral waves. The first is to extend the results from qualitative systems to medically applicable settings by considering more realistic models and tissue properties, and there are several questions that can be investigated here. For example, is the interaction of the point and essential spectrum that creates alternans in the Karma model responsible for alternans across all systems? With the added dynamics in realistic models also comes increased complexity and number of variables, making full 2D spectral calculations computationally expensive. If the continuous spectrum can be attributed to formation of alternans, the 1D computation of the essential spectrum provides a more tractable tool for analysis. Additionally, spiral tips are known to pin to defects in the cardiac tissue, leading to the question of how the spectral properties are impacted by an inhomogeneous material.

A second direction is to look at mechanisms for controlling spiral waves and the arrhythmic patterns they induce. In recent years, there have been a number of methods proposed to terminate arrhythmias with external forcing from a series of electrical pulses [126], but there is no formal understanding of when these methods effectively work. Considering how external forcing impacts the stability of spirals in qualitative and then realistic models may provide the foundation for a rigorous explanation of these methods.

6.2.2 Spectra under zero-diffusion limits

In Chapter 4 we analyzed the shifting limits of the essential spectrum as the slow species becomes diffusionless. The absolute spectra curves also exhibit singular transformations in the zero-diffusion limit, and point eigenvalues converge to the finite limit points of essential spectra. It is unclear what induces these additional changes, and the discussion in Chapter 4 points out difficulties in studying the spectra on bounded domains. Regardless, we hope that the results presented for the essential spectrum lay the groundwork for future studies.

6.2.3 Pseudospectra of spiral waves

In Chapter 2, we commented on how the pseudospectra of the linear operators impacts the computation of discrete eigenvalues. A weighted operator was introduced and provided more accurate computations, but a full investigation of this operator and computation method was not studied here and it leads to several interesting questions. In particular, can the weighted operator be extended from the wave trains to spiral waves in a similar manner by factoring out radial growth given by the spatial eigenvalue of the absolute spectrum. Doing so may lead to a more efficient method of computing point eigenvalues.

Reaction-diffusion operators are inherently non-normal and an investigation into the pseudospectra could provide additional information about the transient behavior of spiral waves. Furthermore, our preliminary results indicated that the pseudospectra for the operators with a full-rank diffusion matrix is more well-behaved than the case of a singular diffusion matrix. It is possible that the pseudospectral bounds is

a factor in the unusual behavior observed for the zero-diffusion limits.

Bibliography

[1] A. L. Hodgkin and A. F. Huxley. "Resting and action potentials in single nerve fibres". In: *The Journal of Physiology* 104.2 (Oct. 1945), pp. 176–195.

[2] D. Noble. "A Modification of the Hodgkin-Huxley Equations Applicable to Purkinje Fibre Action and Pace-Maker Potentials". In: *Journal of Physiology* 160 (1962), pp. 317–352.

[3] G. W. Beeler and H. Reuter. "Reconstruction of the action potential of ventricular myocardial fibres". In: *The Journal of Physiology* 268.1 (June 1977), pp. 177–210.

[4] A. Winfree. "Electrical turbulence in three-dimensional heart muscle". In: *Science* 266.5187 (Nov. 1994), pp. 1003–1006.

[5] A. N. Zaikin and A. M. Zhabotinsky. "Concentration Wave Propagation in Two-dimensional Liquid-phase Self-oscillating System". In: *Nature* 225 (1970), pp. 1–3.

[6] A. T. Winfree. "Spiral Waves of Chemical Activity". In: *Science* 175 (1972), pp. 634–636.

[7] I. R. Epstein and J. A. Pojman. *An Introduction to Nonlinear Chemical Dynamics : Oscillations, Waves, Patterns, and Chaos*. Topics in Physical Chemistry. New York: Oxford University Press, 1998.

[8] A. Volkening and B. Sandstede. "Modelling stripe formation in zebrafish: an agent-based approach". In: *Journal of The Royal Society Interface* 12.112 (Nov. 2015), pp. 20150812–17.

[9] K. Siteur et al. "Beyond Turing: The response of patterned ecosystems to environmental change". In: *Ecological Complexity* 20 (Dec. 2014), pp. 81–96.

[10] J. H. P. Dawes and J. L. M. Williams. "Localised pattern formation in a model for dryland vegetation". In: *Journal of Mathematical Biology* 73.1 (Aug. 2016), pp. 63–90.

[11] This Wikipedia, Wikimedia Commons image is from the user Chris 73, and is freely available at //commons.wikimedia.org/wiki/File:NautilusCutawayLogarithmicSpiral.jpg under the creative commons cc-by-sa 3.0 license.

[12] Wikimedia Commons. URL: https://en.wikipedia.org/wiki/File:Low_pressure_system_over_Iceland.jpg.

[13] X-ray: NASA/CXC/SAO; Optical: Detlef Hartmann; Infrared: NASA/JPL-Caltech, May 2014. URL: https://www.nasa.gov/mission_pages/chandra/multimedia/spiral-galaxy-m81.html.

[14] A. M. Zhabotinsky and A. N. Zaikin. "Spatial effects in a self-oscillating chemical system". In: *Science Publ.* (1971).

[15] P. C. Newell and F. M. Ross. "Inhibition by Adenosine of Aggregation Centre Initiation and Cyclic AMP Binding in Dictyostelium". In: *Journal of General Microbiology* 128.11 (Nov. 1982), pp. 2715–2724.

[16] E. M. Cherry and F. H. Fenton. "Suppression of alternans and conduction blocks despite steep APD restitution: electrotonic, memory, and conduction velocity restitution effects". In: *AJP: Heart and Circulatory Physiology* 286.6 (June 2004), H2332–H2341.

[17] D. S. Rosenbaum et al. "Electrical Alternans and Vulnerability to Ventricular Arrhythmias". In: *New England Journal of Medicine* 330.4 (Jan. 1994), pp. 235–241.

[18] D. Barkley. "Linear stability analysis of rotating spiral waves in excitable media". In: *Physical Review Letters* 68.13 (Mar. 1992), pp. 2090–2093.

[19] D. Barkley. "Euclidean symmetry and the dynamics of rotating spiral waves". In: *Physical Review Letters* 72.1 (Jan. 1994), pp. 164–167.

[20] D. Barkley. "Spiral Meandering". In: *Chemical Waves and Patterns*. Dordrecht: Springer Netherlands, 1995, pp. 163–189.

[21] M. Yoneyama, A. Fujii, and S. Maeda. "Wavelength-Doubled Spiral Fragments in Photosensitive Monolayers". In: *Journal of the American Chemical Society* 117.31 (Aug. 1995), pp. 8188–8191.

[22] V. Perez-Munuzuri et al. "Super-spiral structures in an excitable medium". In: *Nature* 353.6346 (Oct. 1991), pp. 740–742.

[23] J. E. Hall and A. C. Guyton. *Guyton and Hall Textbook of Medical Physiology*. 13th ed. Elsevier, 2016. ISBN: 9781455770052.

[24] Conduction system of heart. Wikimedia Commons, This file is licensed under the Creative Commons Attribution 3.0 Unported license. URL: https://commons.wikimedia.org/wiki/File:2018_Conduction_System_of_Heart.jpg.

[25] J. M. Pastore et al. "Mechanism Linking T-Wave Alternans to the Genesis of Cardiac Fibrillation". In: *Circulation* 99.10 (Mar. 1999), pp. 1385–1394.

[26] S. Alonso, M. Bar, and B. Echebarria. "Nonlinear physics of electrical wave propagation in the heart: a review". In: *Reports on Progress in Physics* 79.9 (Aug. 2016), pp. 1–57.

[27] E. M. Cherry et al. "Introduction to Focus Issue: Complex Cardiac Dynamics". In: *Chaos: An Interdisciplinary Journal of Nonlinear Science* 27.9 (Sept. 2017), pp. 1–9.

[28] R. A. Schmitz, K. R. Graziani, and J. L. Hudson. "Experimental evidence of chaotic states in the Belousov-Zhabotinskii reaction". In: *The Journal of Chemical Physics* 67 (7 1977), pp. 3040–3044.

[29] V. Castets et al. “Experimental evidence of a sustained standing Turing-type nonequilibrium chemical pattern”. In: *Physical Review Letters* 64.24 (June 1990), pp. 2953–2956.

[30] A. T. Winfree. *The Geometry of Biological Time*. Springer New York, 2001.

[31] J.-S. Park and K. J. Lee. “Line-defects-mediated complex-oscillatory spiral waves in a chemical system”. In: *Physical Review E* 73.6 (June 2006), pp. 535–15.

[32] A. Goryachev, H. Chate, and R. Kapral. “Synchronization Defects and Broken Symmetry in Spiral Waves”. In: *Physical Review Letters* 80.4 (Jan. 1998), pp. 873–876.

[33] B. Sandstede and A. Scheel. “Period-Doubling of Spiral Waves and Defects”. In: *SIAM Journal on Applied Dynamical Systems* 6.2 (2007), pp. 494–547.

[34] A. Karma. “Spiral Breakup in Model Equations of Action Potential Propagation in Cardiac Tissue”. In: *Physical Review Letters* 71.7 (Aug. 1993), pp. 1103–1106.

[35] F. Fenton and A. Karma. “Vortex dynamics in three-dimensional continuous myocardium with fiber rotation: Filament instability and fibrillation”. In: *Chaos: An Interdisciplinary Journal of Nonlinear Science* 8.1 (Mar. 1998), pp. 20–47.

[36] B. Sandstede, A. Scheel, and C. Wulff. “Bifurcations and Dynamics of Spiral Waves”. In: *Journal of Nonlinear Science* (June 1999), pp. 1–40.

[37] D. Allexandre and N. F. Otani. “Preventing alternans-induced spiral wave breakup in cardiac tissue: An ion-channel-based approach”. In: *Physical Review E* 70.6 (Dec. 2004), pp. 1–16.

[38] C. D. Marcotte and R. O. Grigoriev. “Unstable spiral waves and local Euclidean symmetry in a model of cardiac tissue”. In: *Chaos: An Interdisciplinary Journal of Nonlinear Science* 25.6 (June 2015), pp. 1–17.

[39] H. M. McNamara et al. “Geometry-Dependent Arrhythmias in Electrically Excitable Tissues”. In: *Cell Systems* 7.4 (Oct. 2018), pp. 359–370.

[40] B. Fiedler and A. Scheel. “Spatio-Temporal Dynamics of Reaction-Diffusion Patterns”. In: *Trends in Nonlinear Analysis*. Springer, 2000, pp. 23–152.

[41] B. Sandstede and A. Scheel. “Absolute and convective instabilities of waves on unbounded and large bounded domains”. In: *Physica D: Nonlinear Phenomena* (2000), pp. 233–277.

[42] B. Sandstede. “Stability of Travelling Waves”. In: *Handbook of Dynamical Systems, Volume 2*. Ed. by B. Fiedler. Elsevier, 2002, pp. 983–1055.

[43] T. Kapitula and K. Promislow. “Essential and Absolute Spectra”. In: *Spectral and Dynamical Stability of Nonlinear Waves*. Springer, 2013, pp. 39–74.

[44] B. Sandstede and A. Scheel. “Absolute versus convective instability of spiral waves”. In: *Physical Review E* (2000), pp. 1–7.

[45] B. Sandstede and A. Scheel. “Superspiral Structures of Meandering and Drifting Spiral Waves”. In: *Physical Review Letters* 86.1 (2001), pp. 171–174.

[46] B. Sandstede and A. Scheel. “Curvature effects on spiral spectra: Generation of point eigenvalues near branch points”. In: *Physical Review E* 73.1 (Jan. 2006), pp. 1–8.

[47] P. Wheeler and D. Barkley. “Computation of Spiral Spectra”. In: *SIAM Journal on Applied Dynamical Systems* 5.1 (Jan. 2006), pp. 157–177.

[48] B. Krauskopf, H. M. Osinga, and J. Galan-Vioque, eds. *Numerical Continuation Methods for Dynamical Systems: Path Following and Boundary Value Problems*. Dordrecht: Springer, 2007.

[49] E. L. Allgower and K. Georg. *Introduction to Numerical Continuation Methods*. Society for Industrial and Applied Mathematics, 2003.

[50] J. A. C. Weideman and S. C. Reddy. “A MATLAB differentiation matrix suite”. In: *ACM Transactions on Mathematical Software* 26.4 (Dec. 2000), pp. 465–519.

[51] J. W. Thomas. *Numerical Partial Differential Equations: Finite Difference Methods*. Vol. 22. Texts in Applied Mathematics. New York, NY: Springer New York, 1995.

[52] G. Bordyugov and H. Engel. “Continuation of spiral waves”. In: *Physica D: Nonlinear Phenomena* 228.1 (Apr. 2007), pp. 49–58.

[53] J. D. M. Rademacher, B. Sandstede, and A. Scheel. “Computing absolute and essential spectra using continuation”. In: *Physica D: Nonlinear Phenomena* 229.2 (2007), pp. 166–183.

[54] L. N. Trefethen and M. Embree. *Spectra and Pseudospectra: The Behavior of Nonnormal Matrices and Operators*. Princeton University Press, Jan. 2005.

[55] S. C. Reddy and L. N. Trefethen. “Pseudospectra of the Convection Diffusion Operator”. In: *SIAM Journal on Applied Mathematics* (Dec. 1994), pp. 1–16.

[56] M. Embree. “The Arnoldi Eigenvalue Iteration with Exact Shifts Can Fail”. In: *SIAM Journal on Matrix Analysis and Applications* 31.1 (Jan. 2009), pp. 1–10.

[57] M. R. Guevara et al. “Electrical alternans and period-doubling bifurcations”. In: *IEEE Computers in Cardiology* (Sept. 1984), pp. 1–5.

[58] E. Cytrynbaum and J. P. Keener. “Stability conditions for the traveling pulse: Modifying the restitution hypothesis”. In: *Chaos: An Interdisciplinary Journal of Nonlinear Science* 12.3 (Sept. 2002), pp. 788–799.

[59] B. Echebarria and A. Karma. “Amplitude equation approach to spatiotemporal dynamics of cardiac alternans”. In: *Physical Review E* 76.5 (Nov. 2007), pp. 1–23.

[60] M. Bar and M. Or-Guil. “Alternative Scenarios of Spiral Breakup in a Reaction-Diffusion Model with Excitable and Oscillatory Dynamics”. In: *Physical Review Letters* 82.6 (Feb. 1999), pp. 1160–1163.

[61] B. Echebarria and A. Karma. “Spatiotemporal control of cardiac alternans”. In: *Chaos: An Interdisciplinary Journal of Nonlinear Science* 12.3 (Sept. 2002), pp. 923–930.

[62] M. Bar and L. Brusch. “Breakup of spiral waves caused by radial dynamics: Eckhaus and finite wavenumber instabilities”. In: *New Journal of Physics* 6 (Jan. 2004), pp. 1–22.

[63] S. Bauer, G. Röder, and M. Bär. “Alternans and the influence of ionic channel modifications: Cardiac three-dimensional simulations and one-dimensional numerical bifurcation analysis”. In: *Chaos: An Interdisciplinary Journal of Nonlinear Science* 17.1 (Mar. 2007), pp. 1–16.

[64] G. A. Gottwald. "Bifurcation analysis of a normal form for excitable media: Are stable dynamical alternans on a ring possible?" In: *Chaos: An Interdisciplinary Journal of Nonlinear Science* 18.1 (Mar. 2008), pp. 1–17.

[65] C. D. Marcotte and R. O. Grigoriev. "Adjoint eigenfunctions of temporally recurrent single-spiral solutions in a simple model of atrial fibrillation". In: *Chaos: An Interdisciplinary Journal of Nonlinear Science* 26.9 (Sept. 2016), pp. 1–15.

[66] A. Karma. "Electrical alternans and spiral wave breakup in cardiac tissue". In: *Chaos: An Interdisciplinary Journal of Nonlinear Science* 4.3 (1994), pp. 461–472.

[67] D. J. B. Lloyd and A. Scheel. "Continuation and Bifurcation of Grain Boundaries in the Swift–Hohenberg Equation". In: *SIAM Journal on Applied Dynamical Systems* 16.1 (Jan. 2017), pp. 252–293.

[68] R. Goh and A. Scheel. "Pattern-forming fronts in a Swift-Hohenberg equation with direction quenching – parallel and oblique stripes". In: *preprint* (Aug. 2017), pp. 1–22.

[69] L. H. Frame and M. B. Simson. "Oscillations of conduction, action potential duration, and refractoriness. A mechanism for spontaneous termination of reentrant tachycardias." In: *Circulation* 78.5 (Nov. 1988), pp. 1277–1287.

[70] M. Courtemanche, L. Glass, and J. P. Keener. "Instabilities of a propagating pulse in a ring of excitable media". In: *Physical Review Letters* 70.14 (Apr. 1993), pp. 2182–2185.

[71] J. D. M. Rademacher. "Homoclinic Bifurcation from Heteroclinic Cycles with Periodic Orbits and Tracefiring of Pulses". PhD thesis. University of Minnesota, May 2004.

[72] A. Warmflash et al. "A method to recapitulate early embryonic spatial patterning in human embryonic stem cells." In: *Nat. Methods* 11 (2014), pp. 847–854. ISSN: 1548-7091. DOI: 10.1038/nmeth.3016.

[73] S. Sundelacruz, M. Levin, and D. Kaplan. "Role of membrane potential in the regulation of cell proliferation and differentiation." In: *Stem Cell Rev.* 5 (2009), pp. 231–246. ISSN: 1550-8943. DOI: 10.1007/s12015-009-9080-2.

[74] B. Hille. *Ion channels of excitable membranes*. Sunderland, MA: Sinauer, 2001.

[75] J. Nolasco and R. Dahlen. "A graphic method for the study of alternation in cardiac action potentials." In: *J. Appl. Physiol.* 25 (1968), pp. 191–196. ISSN: 0021-8987. DOI: 10.1152/jappl.1968.25.2.191.

[76] D. Kaplan et al. "Subthreshold dynamics in periodically stimulated squid giant axons." In: *Phys. Rev. Lett.* 76 (1996), pp. 4074–4077. ISSN: 0031-9007. DOI: 10.1103/PhysRevLett.76.4074.

[77] J. Clay and A. Shrier. "On the role of subthreshold dynamics in neuronal signaling." In: *J. Theor. Biol.* 197 (1999), pp. 207–216. ISSN: 0022-5193. DOI: 10.1006/jtbi.1998.0867.

[78] E. Cherry and F. Fenton. "Suppression of alternans and conduction blocks despite steep APD restitution: electrotonic, memory, and conduction velocity restitution effects." In: *Am. J. Physiol. Heart Circ. Physiol.* 286 (2004), H2332–H2341. ISSN: 0363-6135. DOI: 10.1152/ajpheart.00747.2003.

[79] E. Cytrynbaum and J. Keener. "Stability conditions for the traveling pulse: modifying the restitution hypothesis." In: *Chaos* 12 (2002), pp. 788–799. ISSN: 1054-1500. DOI: 10.1063/1.1503941.

[80] H. Jongsma and R. Wilders. "Gap junctions in cardiovascular disease." In: *Circ. Res.* 86 (2000), pp. 1193–1197. ISSN: 0009-7330. DOI: 10.1161/01.RES.86.12.1193.

[81] S. Roes et al. "Infarct tissue heterogeneity assessed with contrast-enhanced MRI predicts spontaneous ventricular arrhythmia in patients with ischemic cardiomyopathy and implantable cardioverter-defibrillator." In: *Circ Cardiovasc Imaging* 2 (2009), pp. 183–190. ISSN: 1941-9651. DOI: 10.1161/CIRCIMAGING.108.826529.

[82] D. Bers. "Cardiac excitation-contraction coupling." In: *Nature* 415 (2002), pp. 198–205. ISSN: 0028-0836. DOI: 10.1038/415198a.

[83] I. Nitsan et al. 2016.

[84] S. Ng, C. Wong, and S. Tsang. "Differential gene expressions in atrial and ventricular myocytes: insights into the road of applying embryonic stem cell-derived cardiomyocytes for future therapies." In: *Am. J. Physiol. Cell Physiol.* 299 (2010), pp. C1234–C1249. ISSN: 0363-6143. DOI: 10.1152/ajpcell.00402.2009.

[85] A. Amin, H. Tan, and A. Wilde. "Cardiac ion channels in health and disease." In: *Heart Rhythm* 7 (2010), pp. 117–126. ISSN: 1547-5271. DOI: 10.1016/j.hrthm.2009.08.005.

[86] J. Hume and A. Uehara. "Ionic basis of the different action potential configurations of single guinea-pig atrial and ventricular myocytes." In: *J. Physiol.* 368 (1985), pp. 525–544. ISSN: 0022-3751. DOI: 10.1113/jphysiol.1985.sp015874.

[87] C. A. Werley et al. 2017. DOI: 10.1002/cpph.25.

[88] R. Clayton et al. "Models of cardiac tissue electrophysiology: progress, challenges and open questions." In: *Prog. Biophys. Mol. Biol.* 104 (2011), pp. 22–48. ISSN: 0079-6107. DOI: 10.1016/j.pbiomolbio.2010.05.008.

[89] G. Bub, A. Shrier, and L. Glass. "Spiral wave generation in heterogeneous excitable media." In: *Phys. Rev. Lett.* 88 (2002), p. 058101. ISSN: 0031-9007. DOI: 10.1103/PhysRevLett.88.058101.

[90] G. Bub, A. Shrier, and L. Glass. "Global organization of dynamics in oscillatory heterogeneous excitable media." In: *Phys. Rev. Lett.* 94 (2005), p. 028105. ISSN: 0031-9007. DOI: 10.1103/PhysRevLett.94.028105.

[91] S. Rohr et al. "Paradoxical improvement of impulse conduction in cardiac tissue by partial cellular uncoupling." In: *Science* 275 (1997), pp. 841–844. ISSN: 0036-8075. DOI: 10.1126/science.275.5301.841.

[92] D. Du et al. "Action potential morphology of human induced pluripotent stem cell-derived cardiomyocytes does not predict cardiac chamber specificity and is dependent on cell density." In: *Biophys. J.* 108 (2015), pp. 1–4. ISSN: 0006-3495. DOI: 10.1016/j.bpj.2014.11.008.

[93] C. Denning et al. "Cardiomyocytes from human pluripotent stem cells: from laboratory curiosity to industrial biomedical platform." In: *Biochim. Biophys. Acta* 1863 (2016), pp. 1728–1748. ISSN: 0006-3002. DOI: 10.1016/j.bbamcr.2015.10.014.

[94] X. Yang, L. Pabon, and C. Murry. "Engineering adolescence: maturation of human pluripotent stem cell-derived cardiomyocytes." In: *Circ. Res.* 114 (2014), pp. 511–523. ISSN: 0009-7330. DOI: 10.1161/CIRCRESAHA.114.300558.

[95] S. Protze et al. "Sinoatrial node cardiomyocytes derived from human pluripotent cells function as a biological pacemaker." In: *Nat. Biotechnol.* 35 (2017), pp. 56–68. ISSN: 1087-0156. DOI: 10.1038/nbt.3745.

[96] M. Hoekstra et al. "Induced pluripotent stem cell derived cardiomyocytes as models for cardiac arrhythmias." In: *Front. Physiol.* 3 (2012), p. 346. ISSN: 1664-042X. DOI: 10.3389/fphys.2012.00346.

[97] T. Colatsky et al. "The Comprehensive in Vitro Proarrhythmia Assay (CiPA) initiative - Update on progress." In: *J. Pharmacol. Toxicol. Methods* 81 (2016), pp. 15–20. ISSN: 1056-8719. DOI: 10.1016/j.vascn.2016.06.002.

[98] A. Sharma, J. Wu, and S. Wu. "Induced pluripotent stem cell-derived cardiomyocytes for cardiovascular disease modeling and drug screening." In: *Stem Cell Res. Ther.* 4 (2013), p. 150. ISSN: 1757-6512. DOI: 10.1186/scrt380.

[99] M. Birket et al. "Expansion and patterning of cardiovascular progenitors derived from human pluripotent stem cells." In: *Nat. Biotechnol.* 33 (2015), pp. 970–979. ISSN: 1087-0156. DOI: 10.1038/nbt.3271.

[100] H. McNamara et al. "Optically Controlled Oscillators in an Engineered Bioelectric Tissue." In: *Phys. Rev. X* 6 (2016), p. 031001. ISSN: 2160-3308. DOI: 10.1103/PhysRevX.6.031001.

[101] A. Varghese et al. "Endogenous channels in HEK cells and potential roles in HCN ionic current measurements." In: *Prog. Biophys. Mol. Biol.* 90 (2006), pp. 26–37. ISSN: 0079-6107. DOI: 10.1016/j.pbiomolbio.2005.05.002.

[102] M. Sultan et al. "A global view of gene activity and alternative splicing by deep sequencing of the human transcriptome." In: *Science* 321 (2008), pp. 956–960. ISSN: 0036-8075. DOI: 10.1126/science.1160342.

[103] D. Hochbaum et al. "All-optical electrophysiology in mammalian neurons using engineered microbial rhodopsins." In: *Nat. Methods* 11 (2014), pp. 825–833. ISSN: 1548-7091. DOI: 10.1038/nmeth.3000.

[104] Y. Huang, A. Walker, and E. Miller. "A photostable silicon rhodamine platform for optical voltage sensing." In: *J. Am. Chem. Soc.* 137 (2015), pp. 10767–10776. ISSN: 0002-7863. DOI: 10.1021/jacs.5b06644.

[105] H. Zhang, E. Reichert, and A. Cohen. "Optical electrophysiology for probing function and pharmacology of voltage-gated ion channels." In: *eLife* 5 (2016), e15202. ISSN: 2050-084X. DOI: 10.7554/eLife.15202.

[106] D. Qin, Y. Xia, and G. Whitesides. "Soft lithography for micro- and nanoscale patterning." In: *Nat. Protoc.* 5 (2010), pp. 491–502. ISSN: 1754-2189. DOI: 10.1038/nprot.2009.234.

[107] K. ten Tusscher et al. "A model for human ventricular tissue." In: *Am. J. Physiol. Heart Circ. Physiol.* 286 (2004), H1573–H1589. ISSN: 0363-6135. DOI: 10.1152/ajpheart.00794.2003.

[108] K. ten Tusscher and A. Panfilov. "Alternans and spiral breakup in a human ventricular tissue model." In: *Am. J. Physiol. Heart Circ. Physiol.* 291 (2006), H1088–H1100. ISSN: 0363-6135. DOI: 10.1152/ajpheart.00109.2006.

[109] A. Shrier et al. "Prediction of complex atrioventricular conduction rhythms in humans with use of the atrioventricular nodal recovery curve." In: *Circulation* 76 (1987), pp. 1196–1205. ISSN: 0009-7322. DOI: 10.1161/01.CIR.76.6.1196.

[110] M. Kruse et al. "Impaired endocytosis of the ion channel TRPM4 is associated with human progressive familial heart block type I." In: *J. Clin. Invest.* 119 (2009), pp. 2737–2744. ISSN: 0021-9738. DOI: 10.1172/JCI38292.

[111] I. Temple et al. "Connexins and the atrioventricular node." In: *Heart Rhythm* 10 (2013), pp. 297–304. ISSN: 1547-5271. DOI: 10.1016/j.hrthm.2012.10.020.

[112] V. Fast and A. Kléber. "Cardiac tissue geometry as a determinant of unidirectional conduction block: assessment of microscopic excitation spread by optical mapping in patterned cell cultures and in a computer model." In: *Cardiovasc. Res.* 29 (1995), pp. 697–707. ISSN: 0008-6363. DOI: 10.1016/S0008-6363(96)88643-3.

[113] M. Draper and M. Mya-Tu. "A comparison of the conduction velocity in cardiac tissues of various mammals." In: *Q. J. Exp. Physiol. Cogn. Med. Sci.* 44 (1959), pp. 91–109. ISSN: 0033-5541. DOI: 10.1113/expphysiol.1959.sp001379.

[114] B. Hoffman et al. "Electrical activity of single fibers of the atrioventricular node." In: *Circ. Res.* 7 (1959), pp. 11–18. ISSN: 0009-7330. DOI: 10.1161/01.RES.7.1.11.

[115] C. Werley et al. "Geometry-dependent functional changes in iPSC-derived cardiomyocytes probed by functional imaging and RNA sequencing." In: *PLoS One* 12 (2017), e0172671. ISSN: 1932-6203. DOI: 10.1371/journal.pone.0172671.

[116] H. Zhu et al. "Two dimensional electrophysiological characterization of human pluripotent stem cell-derived cardiomyocyte system." In: *Sci. Rep.* 7 (2017), p. 43210. ISSN: 2045-2322. DOI: 10.1038/srep43210.

[117] W. Yamamoto et al. "Electrophysiological Characteristics of Human iPSC-Derived Cardiomyocytes for the Assessment of Drug-Induced Proarrhythmic Potential." In: *PLoS One* 11 (2016), e0167348. ISSN: 1932-6203. DOI: 10.1371/journal.pone.0167348.

[118] I. Karakikes et al. "Human induced pluripotent stem cell-derived cardiomyocytes: insights into molecular, cellular, and functional phenotypes." In: *Circ. Res.* 117 (2015), pp. 80–88. ISSN: 0009-7330. DOI: 10.1161/CIRCRESAHA.117.305365.

[119] P. Burridge et al. "Production of de novo cardiomyocytes: human pluripotent stem cell differentiation and direct reprogramming." In: *Cell Stem Cell* 10 (2012), pp. 16–28. ISSN: 1934-5909. DOI: 10.1016/j.stem.2011.12.013.

[120] N. Mordwinkin, P. Burridge, and J. Wu. "A review of human pluripotent stem cell-derived cardiomyocytes for high-throughput drug discovery, cardiotoxicity screening, and publication standards." In: *J. Cardiovasc. Transl. Res.* 6 (2013), pp. 22–30. ISSN: 1937-5387. DOI: 10.1007/s12265-012-9423-2.

[121] D. Noble. "A modification of the Hodgkin—huxley equations applicable to Purkinje fibre action and pace-maker potentials." In: *J. Physiol.* 160 (1962), pp. 317–352. ISSN: 0022-3751. DOI: 10.1113/jphysiol.1962.sp006849.

[122] A. Pietak and M. Levin. "Bioelectric gene and reaction networks: computational modelling of genetic, biochemical and bioelectrical dynamics in pattern regulation." In: *J. R. Soc. Interface* 14 (2017), p. 20170425. ISSN: 1742-5689. DOI: 10.1098/rsif.2017.0425.

[123] S. Marino et al. "A methodology for performing global uncertainty and sensitivity analysis in systems biology." In: *J. Theor. Biol.* 254 (2008), pp. 178–196. ISSN: 0022-5193. DOI: 10.1016/j.jtbi.2008.04.011.

[124] R. Clayton and A. Panfilov. "A guide to modelling cardiac electrical activity in anatomically detailed ventricles." In: *Prog. Biophys. Mol. Biol.* 96 (2008), pp. 19–43. ISSN: 0079-6107. DOI: 10.1016/j.pbiomolbio.2007.07.004.

[125] C. A. Werley et al. *An ultra-widefield microscope for high-speed, all-optical electrophysiology*. 2017.

[126] S. Luther et al. "Low-energy control of electrical turbulence in the heart: Supplement ". In: *Nature* 475.7355 (2011), pp. 235–239.